

UC Berkeley

UC Berkeley Electronic Theses and Dissertations

Title

Reconstructing past Earth and planetary surface temperatures with cosmogenic noble gases

Permalink

<https://escholarship.org/uc/item/2wd0g82x>

Author

Tremblay, Marissa M.

Publication Date

2017

Peer reviewed|Thesis/dissertation

**Reconstructing past Earth and planetary surface temperatures with
cosmogenic noble gases**

by

Marissa M. Tremblay

A dissertation submitted in partial satisfaction of the
requirements for the degree of
Doctor of Philosophy

in

Earth and Planetary Science

in the

Graduate Division

of the

University of California, Berkeley

Committee in charge:

Professor David L. Shuster, Chair
Professor Donald J. DePaolo
Professor Kurt M. Cuffey

Summer 2017

**Reconstructing past Earth and planetary surface temperatures with
cosmogenic noble gases**

Copyright 2017
by
Marissa M. Tremblay

Abstract

Reconstructing past Earth and planetary surface temperatures with cosmogenic noble gases

by

Marissa M. Tremblay

Doctor of Philosophy in Earth and Planetary Science

University of California, Berkeley

Professor David L. Shuster, Chair

Cosmogenic nuclides, which are produced in the uppermost few meters of the Earth's crust by cosmic-ray particle interactions with atomic nuclei, are commonly used to quantify the rates and timing of surface processes. Some of the first terrestrial cosmogenic nuclide measurements revealed that the cosmogenic noble gases ^3He and ^{21}Ne are diffusively lost at Earth surface temperatures in common silicate minerals like quartz and feldspars. Viewed as a fatal limitation for geologic applications since then, the open-system behavior of cosmogenic noble gases can, in fact, be exploited to quantitatively reconstruct temperatures at the surfaces of Earth and other planetary bodies.

In Chapter 1, I develop a theoretical framework for using cosmogenic noble gases as a paleothermometer based on the principles and mathematics underlying radiogenic noble gas thermochronometry. With this framework and published information on the diffusion kinetics of helium and neon in quartz and feldspars, I demonstrate that cosmogenic ^3He -in-quartz measurements could be used to constrain past surface temperatures at high latitudes and elevations on Earth, while ^{21}Ne -in-feldspar measurements could be used to constrain past surface temperatures at lower latitudes and elevations, and on other planetary bodies.

I then explore the applicability of these published diffusion kinetics through a series of stepwise degassing experiments on quartz (Chapter 2) and feldspars (Chapter 3) containing initially uniform distributions of proton-induced ^3He and ^{21}Ne . These experiments reveal that ^3He and ^{21}Ne diffusion kinetics vary significantly across samples of different geologic origin, and that in many cases quartz and feldspars exhibit complex diffusion behavior manifest as nonlinearity in Arrhenius plots. The origin of this complex behavior is indeterminate, but I demonstrate that it is not caused by temperature-dependent structural transformations or anisotropy and that it is not an artifact of proton irradiation. Instead, complex diffusion behavior appears to be controlled by some intrinsic, sample-specific material property. I also demonstrate that we can mathematically model complex diffusion behavior, and use geologic examples with simple exposure and temperature histories to validate this mathematical model.

Having laid out the theoretical and experimental backbone of cosmogenic noble gas paleothermometry, in Chapter 4 I present two applications of the technique to problems in paleoclimate and planetary science. In the first application, I use cosmogenic ^3He and ^{10}Be observations in quartz from a series of nested moraines in the Maritime Italian Alps to reconstruct temperatures since the Last Glacial Maximum (LGM). I demonstrate that temperatures reconstructed from the cosmogenic ^3He observations are consistent with temperatures expected for this region since the LGM from a global circulation model (GCM) and other proxy data, but that additional constraints are necessary to fully interpret this dataset. In the second application, I use observations of cosmogenic neon isotopes in plagioclase feldspars from lunar sample 76535 to demonstrate that this sample only experienced solar heating during its 142 million year residency at the lunar surface. This constraint on the thermal history of 76535 agrees with existing argon measurements and confirms the fidelity of paleomagnetic measurements in the same sample, which have been used to demonstrate that the Moon had an early core dynamo.

Optimism is never a bad attitude.

Contents

Contents	ii
List of Figures	v
List of Tables	vii
1 Cosmogenic noble gas paleothermometry	1
1.1 Abstract	1
1.2 Introduction	2
1.3 Theoretical background	4
1.3.1 Simultaneous production and diffusion	4
1.3.2 Cosmogenic nuclide production	5
1.3.3 Effects of surface temperature variability on cosmogenic noble gas diffusion	6
1.4 Methods	10
1.4.1 Assessing the sensitivity of cosmogenic noble gas paleothermometry	10
1.4.2 Cosmogenic ^3He retention in Antarctic erratics	11
1.5 Results and Discussion	12
1.5.1 Effects of temperature, exposure duration, and grain size on cosmogenic noble gas retention	12
1.5.2 Geologic scenarios involving temperature change	14
1.5.3 An initial test of cosmogenic noble gas paleothermometry with geologic samples	17
1.6 Conclusions	20
1.7 Acknowledgements	21
2 Diffusion kinetics of ^3He and ^{21}Ne in quartz and implications for cosmogenic noble gas paleothermometry	22
2.1 Abstract	22
2.2 Introduction	23
2.3 Methods	25
2.3.1 Proton irradiation	25

2.3.2	Stepwise heating and degassing experiments	26
2.3.3	Cosmogenic ^3He and ^{21}Ne measurements	27
2.3.4	Sample characterization	29
2.4	Results	30
2.4.1	Step-degassing experiments on proton-irradiated quartz	30
2.4.2	Natural cosmogenic ^3He and ^{21}Ne measurements	36
2.4.3	Fluid and mineral inclusions	39
2.4.4	Trace element concentrations	39
2.5	Discussion	40
2.5.1	Complex Arrhenius behavior	40
2.5.2	Comparison with results from Shuster and Farley (2005)	44
2.5.3	Two-domain model for ^3He diffusion in quartz	45
2.5.4	Implications for He and Ne retentivity in quartz	46
2.5.5	Geologic applicability of laboratory-determined diffusion kinetics	49
2.6	Conclusions	51
2.7	Acknowledgements	51
3	Neon diffusion kinetics and implications for cosmogenic neon paleothermometry in feldspars	52
3.1	Abstract	52
3.2	Introduction	53
3.3	Methods	55
3.4	Results	58
3.5	Discussion	64
3.5.1	Comparison of neon and argon diffusion	65
3.5.1.1	Neon and argon diffusion in alkali feldspars	65
3.5.1.2	Neon and argon diffusion in plagioclase feldspars	68
3.5.2	Multiple diffusion domain (MDD) model for neon diffusion in feldspars	70
3.5.3	Implications for neon retentivity in feldspars	71
3.6	Conclusions	74
3.7	Acknowledgements	75
4	Applications of cosmogenic noble gas paleothermometry to questions in Earth and planetary science	76
4.1	Abstract	76
4.2	Introduction	77
4.2.1	Reconstructing Late Quaternary temperatures in the Maritime Alps, Italy	78
4.2.1.1	Existing proxy constraints on the Late Quaternary climate of the Maritime Alps	80
4.2.2	Surface temperatures of the Moon recorded in lunar sample 76535	81
4.3	Methods	82

4.3.1	Helium measurements in quartz from Gesso Valley moraine boulders .	83
4.3.2	Neon measurements in 76535 anorthite	86
4.4	Results and Discussion	87
4.4.1	Cosmogenic ^3He retention in quartz and temperature reconstruction from Gesso Valley moraine boulders	88
4.4.2	Cosmogenic neon retention in 76535 anorthite and recorded lunar sur- face paleotemperatures	103
4.5	Conclusions	107
4.6	Acknowledgements	109
	Bibliography	110

List of Figures

1.1	Relationship between effective diffusion temperature (EDT) and mean temperature.	7
1.2	EDT as a function of diurnal and annual temperature amplitudes.	8
1.3	Depth dependence of temperature perturbations originating at the surface and cosmogenic nuclide production rates.	9
1.4	Cosmogenic noble gas retention as a function of exposure duration, temperature, and diffusion lengthscale.	13
1.5	Example geologic scenario of cosmogenic noble gas retention across the transition from the last glacial period to the Holocene epoch.	15
1.6	Example geologic scenario of cosmogenic noble gas retention across the Pliocene-Pleistocene transition.	16
1.7	Geologic test of cosmogenic noble gas paleothermometry using cosmogenic ^3He in glacial erratics from the Pensacola Mountains, Antarctica.	19
2.1	Arrhenius and residual plots for He and Ne diffusion in quartz sample HU-08-03.	30
2.2	Arrhenius and residual plots for He and Ne diffusion in quartz sample QA-767-Q(1).	31
2.3	Arrhenius and residual plots for He and Ne diffusion in quartz sample UB09-4. .	32
2.4	Summary Arrhenius plot of the nine quartz diffusion experiments conducted. . .	37
2.5	Arrhenius plots for proton-induced and cosmogenic ^3He and ^{21}Ne diffusion for Antarctic vein quartz sample 04-RDY-139-STR.	38
2.6	Arrhenius plots of two-domain models for ^3He diffusion in quartz samples. . . .	46
2.7	Helium and neon retentivity in quartz.	47
2.8	Retention of cosmogenic ^3He in sample HU-08-03 and comparison with retention predicted from laboratory diffusion kinetics.	50
3.1	Arrhenius and residual plots for Ne and Ar diffusion in Fish Canyon sanidine. .	59
3.2	Arrhenius and residual plots for Ne and Ar diffusion in Gulf of Salerno sanidine.	61
3.3	Arrhenius and residual plots for Ne and Ar diffusion in Benson Mines orthoclase.	62
3.4	Arrhenius and residual plots for Ne and Ar diffusion in Surtsey, Iceland labradorite.	63
3.5	Arrhenius and residual plots for Ne and Ar diffusion in Plush, Oregon labradorite.	64
3.6	Arrhenius and residual plots for Ne and Ar diffusion in Grass Valley anorthite. .	65
3.7	Arrhenius and residual plots for Ne and Ar diffusion in lunar 76535 anorthite. .	66

3.8	Comparison of calculated diffusivities from multiple diffusion domain (MDD) models to calculated diffusivities from neon stepwise degassing experiments. . .	72
3.9	Variability of neon retentivity in feldspars.	74
4.1	Sample locations in the Gesso Valley, Maritime Alps, Italy.	79
4.2	Quartz grain size analysis for Gesso Valley samples.	85
4.3	Cosmogenic ^3He retention as a function of ^{10}Be exposure age in quartz, Gesso Valley moraine samples.	90
4.4	Arrhenius plots for helium diffusion in quartz from Gesso Valley moraine samples.	91
4.5	Minimized misfit between observed and MDD-modeled ^3He diffusivities as a function of number of diffusion domains, Gesso Valley quartz samples.	93
4.6	EDTs integrated over the exposure duration of Gesso Valley moraine samples. .	95
4.7	Gesso Valley EDTs calculated from modern meteorological data.	96
4.8	Cosmogenic ^3He retention in PDP10 calculated from scaled TraCE-21ka seasonal temperatures and spliced, scaled chironomid July temperatures.	97
4.9	Cosmogenic ^3He retention in PM1 and PM4 calculated from scaled TraCE-21ka seasonal temperatures.	98
4.10	Cosmogenic ^3He retention in TDB1 and TDB3 calculated from scaled TraCE-21ka seasonal temperatures.	98
4.11	Minimized misfit between observed and MDD-modeled ^3He diffusivities as a function of activation energy for Gesso Valley quartz samples, assuming a three domain diffusion model.	101
4.12	Observations of naturally-occurring neon isotopes in 76535 anorthite.	105
4.13	Arrhenius plot for neon diffusion experiment on 76535 anorthite.	106
4.14	Misfit between observed and calculated cosmogenic neon retention in 76535 anorthite as a function of effective diffusion temperature.	107
4.15	Relationship between EDT and mean temperature through the lunar daily insolation cycle at the Apollo 17 site.	108

List of Tables

1.1	Cosmogenic ^{10}Be and ^3He observations for glacially transported cobbles from the Pensacola Mountains, Antarctica.	18
2.1	Description of quartz samples studied in diffusion experiments.	26
2.2	Summary of ^3He quartz diffusion parameters.	33
2.3	Summary of ^{21}Ne quartz diffusion parameters.	34
3.1	Description of feldspar samples studied in diffusion experiments.	55
3.2	Summary of neon diffusion parameters for feldspars.	60
3.3	Best fit multiple diffusion domain model parameters for neon in feldspars.	71
4.1	Sample information for previously dated Gesso Valley moraine boulders.	83
4.2	Observations of cosmogenic ^3He in Gesso Valley quartz samples.	89
4.3	Apparent ^3He exposure ages and retention in Gesso Valley quartz samples.	90
4.4	Three domain MDD model parameters for ^3He diffusion in Gesso Valley quartz samples.	93
4.5	Observations of naturally-occurring neon isotopes in 76535 anorthite.	104

Acknowledgments

I thank, first and foremost, my Ph.D. advisor Professor David Shuster. The intellectual insight, scientific opportunities, and friendship David afforded me over the last five years have been truly invaluable to me. It brings me great joy to know that we will remain lifelong colleagues and friends. I am also deeply grateful to Dr. Greg Balco, who was instrumental as a collaborator to the work presented in this dissertation and whom I admire greatly as a scientist. I also thank Professors Bill Dietrich and Kurt Cuffey for inspiring and molding my ever-increasing interest in Earth surface processes, Professor Nick Swanson-Hysell for allowing me to explore geochemistry in deep time through my second qualifying exam project, and Professor Don DePaolo and Ron Amundson for their insight and support as members of my committees.

One of the best aspects of working with David was interacting with the other Ph.D. students and postdoctoral scholars in his group. Dr. Matthew Fox is a delightfully challenging colleague to work with, and I am grateful for the time and effort he put into our collaborative efforts. Drs. Alka Tripathy Lang, Sonia Tikoo, and Becky Reverman became important scientific and life mentors to me during my time in Berkeley, showing me that there is more than one successful path to follow upon finishing the Ph.D.. And Chelsea Willett, fellow Shustar, has been a superb sounding board, lab mate, and friend over the past three years.

The research presented here would have been substantially more challenging, if not impossible, without the resources and expertise of the staff at the Berkeley Geochronology Center. In particular, I thank Tim Becker, who is really the lifeblood of the BGC noble gas laboratory and from whom I have gained a wealth of knowledge about mass spectrometry. I also especially thank Nick Fylstra, who began his technician job at the same time I started my Ph.D. and who has been a patient and ever-friendly colleague as we learned alongside one another. Likewise, I thank Shaun Brown, Tim Teague, and Tom Owens in EPS for their willingness to help me and teach me about some technical aspects of my research. I would also be remiss not to thank the UC Berkeley Larsen Grant and National Science Foundation (GRFP, EAR 1111853, and EAR 1322086) for financially supporting this research.

I also owe immense thanks to my friends at the BGC and in EPS who had nothing to do with my research but who kept me sane, happy, and grounded through the last five years. Dr. Courtney Sprain and I were “adversaries” for the first five seconds of our Ph.D.s, but fortunately we became best friends just as quickly. Her persistent positivity and friendship have meant more to me than she knows, and I so look forward to watching her career blossom. Kristen Fauria is the friend who always seems to be on my level; I will miss the ease of understanding in our regular interactions, but know that we will remain close no matter where academic life takes us. Dr. Ryan Ickert was an unexpected and now dear friend who, though he will kill me for writing this, has changed my life for the better. I acknowledge my friendships with Chris Johnson, ever the straight shooter, and Dr. Mong-Han Huang, ever the cheerleader, as well.

Many people made my journey to earning my Ph.D. at UC Berkeley possible, too many to thank here. I give a special shout out to Professors Nick Christie-Blick and Sidney Hemming

at Columbia University, who took me under their wing when I was a naive eighteen-year-old to teach me the importance and reward of doing scientific research. I also thank Emily (Hernandez-Goldstein) Cooperdock, a friend and colleague who has seen the worst of me and nonetheless sees the best in me; I look forward to our careers continuing to parallel one another. Last, but obviously not least, I thank my parents Patricia and Richard Tremblay. They have encouraged me to follow my passion without reserve and been an emotional backstop for me even when I haven't always been there for them over the last five years. I dedicate this work to them.

Chapter 1

Cosmogenic noble gas paleothermometry

This chapter was previously published in Tremblay, M.M., Shuster, D.L., and Balco, G., *Earth and Planetary Science Letters* **400**, 195–205 (2014). doi:10.1016/j.epsl.2014.05.040

1.1 Abstract

We present a theoretical basis for reconstructing paleotemperatures from the open-system behavior of cosmogenic noble gases produced in minerals at Earth's surface. Experimentally-determined diffusion kinetics predicts diffusive loss of cosmogenic ^3He and ^{21}Ne from common minerals like quartz and feldspars at ambient temperatures; incomplete retention has also been observed empirically in field studies. We show that the theory of simultaneous production and diffusion that applies to radiogenic noble gases in minerals—the basis of thermochronology—can also be applied to cosmogenic noble gases to reconstruct past surface temperatures on Earth. We use published diffusion kinetics and production rates for ^3He in quartz and ^{21}Ne in orthoclase to demonstrate the resolving power of cosmogenic noble gas paleothermometry with respect to exposure duration, temperature, and diffusion domain size. Calculations indicate that, when paired with a quantitatively retained cosmogenic nuclide such as ^{21}Ne or ^{10}Be , observations of cosmogenic ^3He in quartz can constrain temperatures during surface exposure in polar and high altitude environments. Likewise, ^{21}Ne retention in feldspars is sensitive to temperatures at lower latitudes and elevations, thus expanding the potential geographic applicability of this technique to most latitudes. As an example, we present paired measurements of ^3He and ^{10}Be in quartz from a suite of Antarctic sandstone erratics to test whether the abundances of cosmogenic ^3He agree with what is predicted from first principles and laboratory-determined diffusion kinetics. We find that the amounts of cosmogenic ^3He present in these samples are consistent with the known mean annual temperature (MAT) for this region of Antarctica between -25 and -30 °C. These results demonstrate the method's ability to record paleotemperatures through geologic

time.

1.2 Introduction

Reconstructing past surface temperatures from continental settings is important for understanding how climatic processes, such as glacial cycles, and tectonic processes, such as orogenic-driven elevation change, have shaped terrestrial environments and landforms. The most widely applied methods for reconstructing past surface temperatures on continents involve measuring stable isotopes of oxygen in carbonates or ice. However, in the case of carbonates, traditional stable isotope methods require that the oxygen isotopic composition of water from which carbonate formed is known, which is rarely the case [e.g. 1–3]. In the past decade, measurements of multiply substituted isotopologues (clumped isotopes) in carbonates have circumvented this limitation [4, 5]. Nevertheless, temperatures calculated from carbonate clumped isotope measurements can be anomalously high [6] and vary as a function of seasonal parameters like precipitation [7] precluding simple interpretation in some cases. Leaf physiognomy [e.g. 8, 9] and pollen distribution [e.g. 10] have also been used to estimate terrestrial paleotemperatures. However, these bioclimatic proxies depend on numerous additional climate parameters, including precipitation, plant-available moisture, seasonality, and length of the growing season. All existing terrestrial paleotemperature proxies are limited by the abundance of specific minerals/fossils in the rock record and can suffer from poor preservation and diagenetic alteration [1]. Thus quantitative reconstruction of past terrestrial temperatures remains a major challenge despite the development of several paleotemperature proxies over the past few decades.

In this paper we describe a new paleotemperature proxy based on the open-system behavior of cosmogenic noble gases in common minerals. ^3He and ^{21}Ne were the first in situ-produced cosmogenic nuclides to be unambiguously observed in terrestrial materials [11–13]. Since then, measurements of cosmogenic nuclides in minerals have transformed how Earth surface processes are studied and quantified [14]. ^3He and ^{21}Ne are particularly attractive for studying surface processes. Since ^3He and ^{21}Ne are both stable, they can be used to quantify exposure histories that are long relative to the half-lives of cosmogenic radionuclides like ^{10}Be and ^{26}Al . Cosmogenic ^3He and ^{21}Ne also have high production rates in terrestrial materials, minimizing the amount of material needed for analysis, and noble gas measurements are faster and cheaper than measurements of cosmogenic radionuclides by accelerator mass spectrometry. Cosmogenic ^{21}Ne in quartz, olivine, pyroxene, and amphibole and cosmogenic ^3He in the latter three phases have been extensively used to study geomorphic and geologic processes [e.g. review by 15]. Empirical observations [16–19], and in some cases measured diffusion kinetics [20–23], indicate that these cosmogenic noble gas–mineral pairs exhibit quantitative retention at Earth surface temperatures.

In contrast, cosmogenic ^3He and ^{21}Ne experience significant diffusive loss over geologic time at Earth’s surface in quartz and feldspars, respectively. As a result, these cosmogenic noble gas–mineral pairs have been almost entirely avoided in surface process studies. Incom-

plete retention of cosmogenic ^3He was first inferred from comparisons of ^3He -based exposure ages with ^{10}Be or ^{26}Al ages from the same quartz samples. In diverse settings, the ^3He ages were systematically younger [17, 24–26]. Experimentally-determined diffusion kinetics of ^3He in quartz broadly agrees with these observations and indicates that significant proportions of ^3He can be lost from quartz over time, even at subzero temperatures [22]. Although one study showed that ^3He could be quantitatively retained in very large quartz grains with < 100 ka of exposure in Antarctica [27], the only published cosmogenic ^3He –quartz measurements since the mid-1990s were used to screen for relatively old versus young erratics and sub-select samples for ^{10}Be analyses [28]. Observations of cosmogenic ^{21}Ne in feldspars [16, 29] and experimentally-determined diffusion kinetics of Ne [21] suggest that feldspars can also experience diffusive loss of cosmogenic ^{21}Ne at Earth’s surface, depending on mineralogical composition. Sanidine, which apparently exhibits quantitative retention of ^{21}Ne [21, 29], is the only feldspar that has been used to study surface processes [18, 30].

Although avoided in cosmogenic nuclide studies, the open-system behavior of radiogenic noble gases has been extensively studied and utilized as a method for reconstructing thermal histories of minerals and rocks in the upper lithosphere [31]. Widely applied methods of noble gas thermochronology, such as the $^{40}\text{Ar}/^{39}\text{Ar}$ system in feldspars and the (U-Th)/He system in apatite and zircon, record both time, through the production of noble gas atoms via radioactive decay, and temperature, through their thermally-activated diffusive loss. In principle, cosmogenic noble gas–mineral pairs exhibiting open-system behavior also record the thermal histories of rocks that can be quantified using the same theoretical framework as radiogenic noble gases. Since cosmogenic nuclide production occurs almost entirely within the uppermost few meters of the Earth’s surface, cosmogenic noble gas–mineral pairs ought to record thermal histories of local surface environments.

Here we present calculations to test whether the open-system behavior of cosmogenic ^3He in quartz and ^{21}Ne in feldspars can be used to quantify past temperatures at Earth’s surface. We utilize published production rates and diffusion kinetics of these cosmogenic noble gas–mineral pairs, although future paleothermometry applications will warrant tighter constraints on both of these variables. We show that with relatively simple models based on first principles we can predict the observed abundances of cosmogenic ^3He in an example set of quartz samples from Antarctica with simple Holocene exposure histories. This work focuses on ^3He and ^{21}Ne in quartz and feldspars, respectively, but the theoretical framework presented here can be extended to any cosmogenic noble gas–mineral system and to other planetary bodies and higher temperature regimes [e.g. 32–34]. Further, this cosmogenic nuclide-based paleothermometer, which is characterized by fundamentally different principles and assumptions from preexisting paleotemperature proxies, may be particularly useful for studying surface processes where pre-existing proxies cannot be applied, or provide important tests for internal consistency in cases where they can.

1.3 Theoretical background

1.3.1 Simultaneous production and diffusion

The theory and mathematics describing the open-system behavior of noble gases in minerals have been extensively developed in the field of noble gas thermochronology; we present a brief review of fundamental concepts here. The concentration of a noble gas M simultaneously being produced and diffusing from a mineral changes as a function of time t according to:

$$\frac{\partial M}{\partial t} = \frac{D(T)}{a^2} \nabla^2 M + P_M \quad (1.1)$$

where D is diffusivity, ∇^2 is the second-order spatial derivative or Laplacian, a is the dimension of the diffusion domain, and P_M is the mineral-specific production rate of M . Eq. (1.1) requires that diffusion of noble gases in the mineral is Fickian (i.e., atoms move from regions of high to low concentration with a flux proportional to the concentration gradient) and isotropic. Published diffusion experiments suggest that these conditions are met for noble gas diffusion in quartz [22] and orthoclase [21]. Solutions to Eq (1.1) must also satisfy the boundary condition that the concentration of M at a , the outer boundary of the diffusion domain, is zero. This condition is effectively valid for minerals when the diffusion domain is equivalent to the grain size, as diffusivities along grain boundaries are typically several orders of magnitude greater than within the mineral grains themselves [e.g. 35], and the surrounding environment is nearly an infinite reservoir for rare nuclides. Abundances of cosmogenic ^3He in different grains sizes sharing a common exposure history indicate that the diffusion domain and grain size are equivalent for quartz [25]. For thermally-activated diffusion of noble gases in minerals, a large body of research [e.g. review by 36] shows that the diffusivity D depends exponentially on temperature according to the Arrhenius relationship:

$$\frac{D(T)}{a^2} = \frac{D_0}{a^2} \exp\left(\frac{-E_a}{RT(t)}\right) \quad (1.2)$$

where D_0 is the diffusivity at infinite temperature, E_a is the activation energy, R is the gas constant, and T is temperature. The diffusion parameters D_0 and E_a are specific to a particular noble gas–mineral pair and can be determined empirically via laboratory experiments. If both temperature (and therefore diffusivity) and the production rate remain constant through time, and if we assume the diffusion domain has a spherical geometry, Eq. (1.1) has the analytical solution described by Wolf et al. [37]:

$$M(t) = P_M \frac{a^2}{D} \left[\frac{1}{15} - \sum_{n=1}^{\infty} \frac{6}{\pi^4 n^4} \exp\left(-\pi^2 n^2 \frac{D}{a^2} t\right) \right] \quad (1.3)$$

The spherical geometry assumption is reasonable for most mineral grains with modest aspect ratios, as long as the surface area to volume ratio of the actual diffusion domain and the spherical approximation are equivalent [38, 39]. When temperature and/or production

vary as a function of time, the analytic approach is no longer valid and a numerical solution is required. For calculations in this paper involving time-varying production rates, we implement the Crank-Nicholson finite-difference scheme described by Ketcham [40] to discretize and solve Eq. (1.1).

1.3.2 Cosmogenic nuclide production

A fundamental difference between solutions to Eq. (1.1) for radiogenic and cosmogenic noble gases is the production term [for an extensive review of cosmogenic nuclide production, see 15, 41]. Cosmogenic nuclides are produced when high-energy cosmic-ray particles ultimately induce nuclear transmutations, typically spallation reactions, of target atoms in a mineral. Production rates depend on i) the flux and energy spectrum of incident particles, ii) the elemental composition of the target mineral, and iii) the cross-sections of relevant reactions. At typical Earth surface elevations, the flux of energetic particles is primarily controlled by an exponential dependence of production rate on the thickness of shielding mass (e.g., the overlying atmosphere and any additional shielding by rock or soil) above the sample [42]. Given a mineral with uniform composition (e.g. quartz), however, the production ratio of two cosmogenic nuclides can only vary if both the relevant reaction cross-sections depend differently on particle energy and the energy spectrum of the cosmic-ray flux changes. Since cross-sections of most geologically relevant reactions have similar energy dependence, and since the energy spectrum of the cosmic-ray flux is nearly invariant at typical surface elevations, the production rate ratio of two nuclides in a particular target mineral is essentially constant over time regardless of the variation in absolute production rate due to surface erosion or deposition. In practice, nearly all surfaces on Earth are subject to either erosion or deposition, so incorporating the time-dependence of production in solutions to Eq. (1.1) will be important for reconstructing thermal histories from cosmogenic noble gases.

Apparent exposure ages can be determined from the concentration M and local production rate P_M of a cosmogenic noble gas exhibiting open-system behavior in a particular mineral (Eq. 1.1). However, like open-system behavior of radiogenic noble gases, this apparent age has little significance by itself, providing only a lower bound on exposure age. Additional information is required to reconstruct a thermal history. In the simplest case of a single period of surface exposure with negligible erosion, this information can be obtained by pairing the partially-retained nuclide with one that is not subject to diffusive loss. Given knowledge of relevant production rates, the concentration of the quantitatively retained nuclide establishes the exposure duration, and the concentration of the partially retained nuclide becomes a function only of the integrated temperature over a sample's exposure. In the case of more complex exposure histories involving erosion and/or burial, changes in depth and production rate with time can be determined from the concentration–depth profile of one or paired measurements of two quantitatively retained cosmogenic nuclides [30, 43, 44]. Thus we can use measurements of one or more quantitatively retained nuclides to independently determine both the time interval over which to solve Eq. (1.1) and how the production term evolves. Once the exposure history of the sample is known, the concentra-

tion of the partially-retained nuclide is directly related to the temperature experienced by the sample during that history.

1.3.3 Effects of surface temperature variability on cosmogenic noble gas diffusion

Rocks at Earth's surface experience temperature oscillations on daily, seasonal, and longer timescales. Because diffusion is a continuous process and a nonlinear function of temperature, these periodic surface temperature oscillations will influence the time-integrated thermal history that a cosmogenic noble gas–mineral pair records. We are ultimately interested in changes in mean ambient temperatures over geologic time. Therefore we need to account for the effects of periodic temperature variations on diffusivity in order to infer mean ambient temperatures from measurements of cosmogenic noble gases. This can be achieved by defining the effective diffusion temperature, or EDT, as the temperature corresponding to the mean diffusivity over a variable temperature function. Mathematically, the EDT can be written by transforming Eq. (1.2):

$$EDT = \frac{-E_a}{R} \left(\ln \left[\frac{1}{t} \int_0^t \exp \left(\frac{-E_a}{RT(t')} \right) dt' \right] \right)^{-1} \quad (1.4)$$

where t is the period of the temperature variation. This concept of an effective temperature has been previously defined and applied in the thermoluminescence literature [45, 46]. We use the term effective diffusion temperature here to emphasize that, given the same temperature function, the effective temperature of solid-state noble gas diffusion may not be the same as the effective temperature for another temperature-dependent process. Since diffusivity is a nonlinear function of temperature, the EDT will always be greater than or equal to the mean temperature of a given temperature function. To conceptualize this, Fig. 1.1 shows the relationship between temperature (A) and diffusivity (B) for a sinusoidal temperature function.

The difference between EDT and mean temperature (ΔT , Fig. 1.1A) is a function of the mean temperature, amplitude of the temperature oscillation, and diffusion parameters used to calculate EDT with Eq. (1.4), but is independent of frequency for a one component temperature oscillation, as in Fig. 1.1. For a given mean temperature, ΔT increases with increasing amplitude. This means that rock samples at the surface experiencing the same mean temperature and exposure duration can have different EDTs and therefore observable differences in cosmogenic noble gas retention, such that the sample experiencing a larger amplitude temperature variation will have lower net retentivity over time. Similarly, because EDT is a function of activation energy, the EDT of cosmogenic ^3He in quartz will be different from that of cosmogenic ^{21}Ne in orthoclase within the same sample. The effects of temperature oscillations are magnified at lower temperatures; in other words, for the same amplitude temperature oscillation, ΔT increases with decreasing mean temperature.

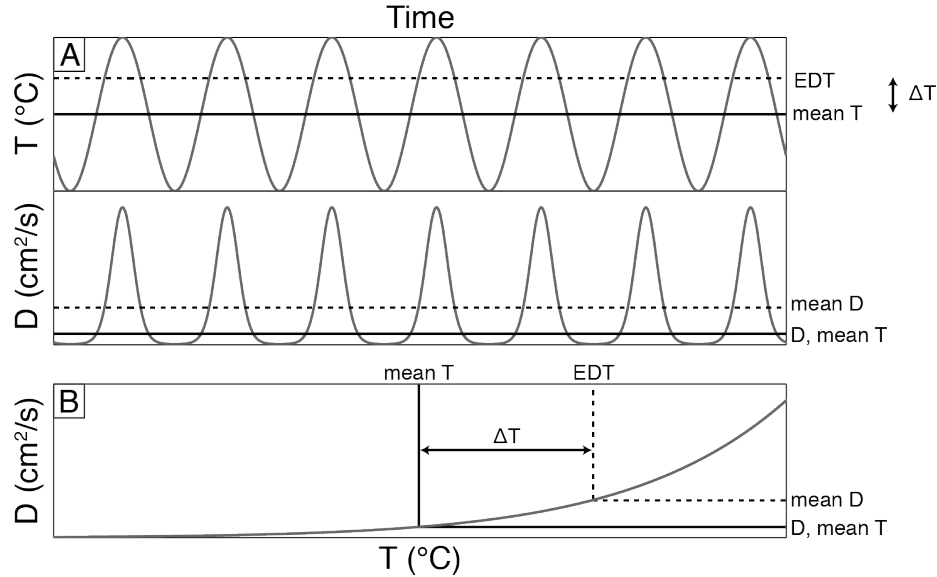


Figure 1.1: Schematic illustration of ΔT , the difference between effective diffusion temperature (EDT) and mean temperature. The EDT is calculated from the mean diffusivity D experienced over the temperature function in (A), which will always be greater than or equal to the mean temperature since diffusivity is a nonlinear function of temperature (B).

ΔT does depend on frequency when multiple temperature oscillations occur simultaneously. To demonstrate this, Fig. 1.2 shows ΔT for periodic temperature functions with a mean of 0 °C and different daily and annual amplitudes for both the ³He–quartz (A) and ²¹Ne–feldspar (B) systems, calculated according to Eq. (1.4). Surfaces for mean temperatures other than 0 °C would plot sub-parallel to those shown in Fig. 1.2, with lower mean temperatures corresponding to greater ΔT values and divergence of the surfaces with increasing amplitudes.

In addition to heat conduction between rocks at the surface and surrounding air, rocks are also directly heated by incident solar radiation. The effects of radiative heating on rock temperature are complex and depend on factors such as the shortwave and longwave radiative fluxes, thermal properties of the rock like albedo, and short-term variables like moisture content, snow cover, and wind conditions [e.g. 47–49]. Barring stochastic, transient variables like wind, radiative heating has the same period as daily temperature oscillations and thus increases the magnitude of daily rock temperature amplitudes relative to that of air. Except in extreme desert environments, where the daily rock temperature amplitude can be as large as 40 °C [50, 51], 5–10 °C amplifications are typical, depending on albedo [48, 49]. Daily temperature amplitudes this large have significant effects on the ΔT , as shown in Fig. 1.2. Convolution of diurnal radiative heating of rock surfaces with daily and annual temperature oscillations can therefore result in large differences between EDT and mean temperature at the surface that need to be accounted for.

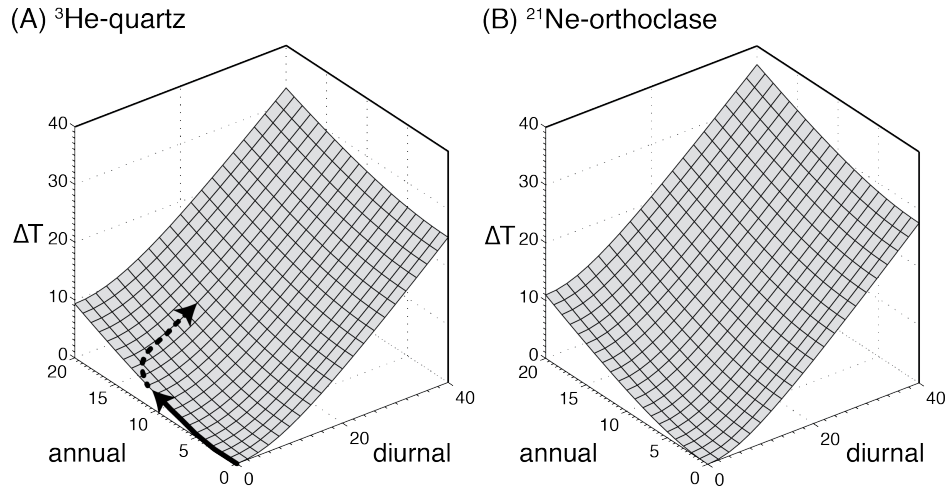


Figure 1.2: ΔT , the difference between effective diffusion temperature (EDT) and mean temperature, as a function of the amplitudes of diurnal and annual temperature oscillations for a mean temperature of 0 °C, calculated according to Eq. (1.4). We show ΔT surface for both the ^3He –quartz (A) and ^{21}Ne –orthoclase (B) systems using the diffusion kinetics of Shuster and Farley [22] and Gourbet et al. [21], respectively. For higher mean temperatures, ΔT surfaces plot sub-parallel to and below the surface for 0 °C shown; the converse is true for lower mean temperatures. In (A), we show an example of how ΔT might evolve for a constant mean temperature as a sample approaches the surface due to erosion. Below ~ 14 cm, the ΔT experienced by a sample is primarily a function of the annual temperature oscillation and evolves along the solid arrow. Above ~ 14 cm, the amplitude of the annual temperature oscillation approaches its magnitude at the surface, and the daily amplitude begins to increase. At these depths, ΔT evolves approximately according to the dashed arrow.

Since cosmogenic nuclide production occurs within a few meters of the Earth’s surface and a typical sample moves with respect to the surface due to either erosion or aggradation, the attenuation of surface temperature variations with depth must also be considered. The amplitude of any surface temperature oscillation decreases with depth beneath the surface according to:

$$T(z) = A \exp\left(-z \sqrt{\frac{\omega \rho c_p}{2k}}\right) \exp\left(i \left[\omega t - z \sqrt{\frac{\omega \rho c_p}{2k}}\right]\right) \quad (1.5)$$

where T is temperature, z is depth, A is the surface temperature amplitude, ω is the surface temperature frequency, ρ is rock density, c_p is specific heat capacity, and k is thermal conductivity [e.g. 52]. Fig. 1.3A shows solutions to Eq. 1.5 for the typical thermal properties and density of granite and for different frequency and amplitude surface temperature oscillations. Fig. 1.3A demonstrates that longer period temperature oscillations will propagate to greater depths. The skin depth—the depth at which the temperature ampli-

tude decreases by $1/e$ —is 0.14 m for daily and 2.8 m for annual oscillations; glacial cycle temperature oscillations affect temperatures tens to hundreds of meters beneath the surface. For comparison, the skin depth associated with the attenuation of cosmogenic nuclide production by spallation reactions in the same density material is 0.59 m (Fig. 1.3B). This indicates that cosmogenic nuclide production rates remain relatively high at depths where daily air and rock temperature oscillations are significantly diminished. The amplitude of the annual temperature oscillation, however, is significant at all depths where cosmogenic nuclide production occurs.

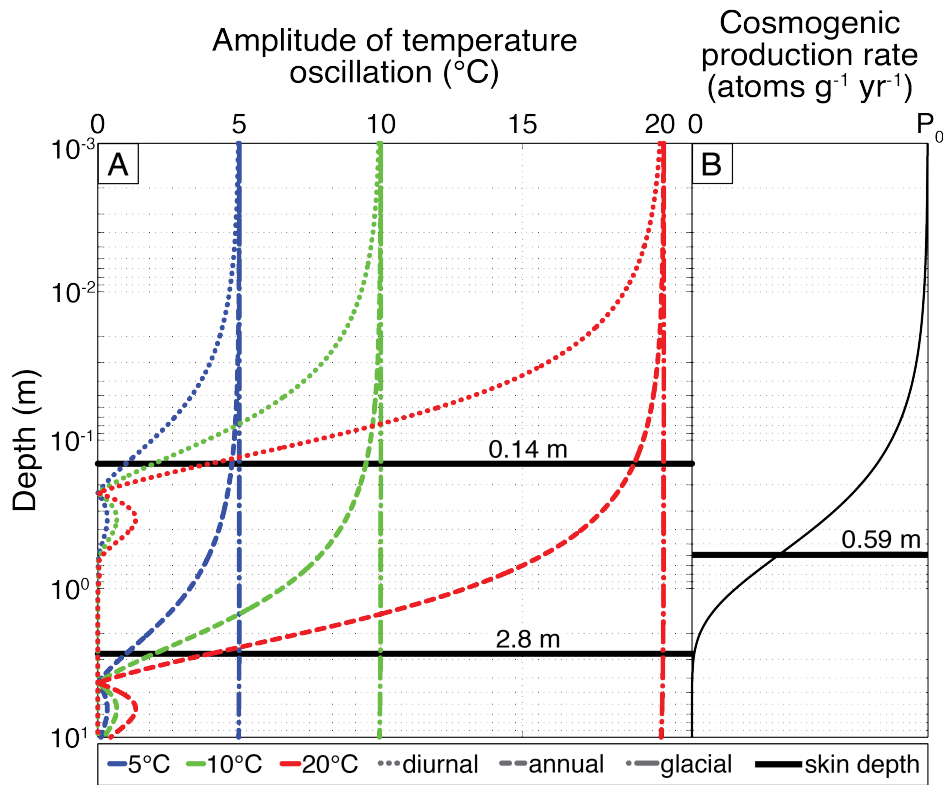


Figure 1.3: Depth dependence of temperature perturbations originating at the surface (A) and cosmogenic nuclide production rates (B). In (A), we use the thermal properties of granite from McGreevy [49] and a density of 2.7 g/cm^3 to calculate with Eq. (1.5) how thermal waves with diurnal, annual, and glacial-cycle periods with 5, 10, and 20 $^{\circ}\text{C}$ amplitudes at the Earth’s surface propagate with depth. The skin depth, the depth at which the amplitude of the temperature perturbation is $1/e$ of the surface amplitude, is noted for the different period oscillations. (B) Attenuation of a spallogenic cosmogenic nuclide production rate with depth, with a surface production rate of P_0 . We assumed the same density as in (A) and an attenuation coefficient of 160 g/cm^2 . The skin depth, the depth at which production equals P_0/e , is also shown.

The arrows in Fig. 1.2A schematically demonstrate how daily and annual temperature oscillations influence the EDT and ΔT of a rock as it is brought to the surface by erosion for a constant mean surface temperature. At depths $> \sim 0.14$ m, the amplitudes of daily temperature oscillations (Fig. 1.3, dotted curves) are small and only the annual temperature oscillation (Fig. 1.3, dashed curves) will significantly affect ΔT . At these depths, ΔT (and EDT) evolves according to the solid arrow in Fig. 1.2A as the sample moves toward the surface and the amplitude of the annual temperature oscillation increases. At depths $< \sim 0.14$ m, the amplitude of the daily temperature oscillation becomes significant, while the amplitude of the annual temperature oscillation approaches its surface magnitude; the ΔT will then evolve according to the dashed arrow in Fig. 1.2A. The reverse thermal history is expected for samples that are progressively buried due to sedimentation.

To summarize, rocks at Earth’s surface are heated by surrounding air, which experiences temperature oscillations of predictable frequencies and amplitudes, and by solar radiation, which increases the amplitude of daily rock temperatures above that of the surrounding air. Calculating a mean temperature from an observed diffusion temperature (i.e., EDT) of a cosmogenic noble gas–mineral system therefore requires considering the depth integrated effects of both diurnal radiative heating and short-term air temperature oscillations on rock temperatures. These short-term temperature oscillations should be predictable on long ($> 10^3$ yr) timescales, as they are primarily a function of solar insolation and therefore latitude.

1.4 Methods

1.4.1 Assessing the sensitivity of cosmogenic noble gas paleothermometry

We present a series of calculations using the theory and mathematics outlined above to establish under what conditions cosmogenic noble gas–mineral pairs will record surface temperature histories. All calculations utilize the diffusion parameters for He in quartz reported by Shuster and Farley [22] [$E_a = 84.5$ kJ/mol; $\ln(D_0/a^2) = 11.1 \ln(s^{-1})$]. We do not use the diffusion kinetics of ^3He in quartz reported by Trull et al. [23], as their results were likely compromised by a nonuniform, unknown initial distribution of cosmogenic ^3He in their experiment. Gourbet et al. [21] conducted diffusion experiments on multiple types of feldspars, demonstrating that feldspars generally experience diffusive loss of ^{21}Ne at Earth surface temperatures but that diffusion parameters are compositionally dependent. Since the diffusion experiment on MadOr orthoclase ($An_{0.2}Ab_{5.5}Or_{94.3}$) yielded the most robust, simple Arrhenius relationship for Ne diffusion [21], we use these parameters in our calculations [$E_a = 112.1$ kJ/mol; $\ln(D_0/a^2) = 7.4 \ln(s - 1)$]. For quartz, we use a sea level high-latitude (SLHL) cosmogenic production rate of 108 atoms/g/yr for ^3He [53]. Production rates of cosmogenic ^{21}Ne in feldspars vary depending on mineral composition. We use a SLHL production rate of 22.4 atoms/g/yr for the composition of MadOr orthoclase, calculated from the stoichiometric production rates of Gourbet et al. [21] and the model production rates of

Kober et al. [29].

In the first set of calculations, we investigate the feasibility of estimating the integrated temperature over a single exposure period. We assume that production and the EDT are constant through time and use Eq. (1.3) to model the effects of grain size, temperature, and exposure duration on cosmogenic noble gas retention. Retention R , or the fraction of the cosmogenic noble gas produced that has not diffused from the mineral grain, can be defined as:

$$R = \left(\frac{M_A}{M_B}\right) \left(\frac{P_A}{P_B}\right)^{-1} \quad (1.6)$$

where A is a diffusive cosmogenic noble gas and B is a quantitatively-retained cosmogenic nuclide. Any cosmogenic nuclide that does not diffuse from the mineral or decay over the timescale of interest can be used as the quantitatively retained nuclide B ; in the example dataset discussed later we use ^{10}Be . If both cosmogenic nuclides are quantitatively retained at the EDT, $R = 1$. If A is diffusively lost, R approaches zero over time as the concentration of A reaches steady-state and ingrowth of B continues. As defined in Eq. (1.6), R is readily calculated from laboratory measurements of A and B and knowledge of their production rate ratio.

In the second set of calculations, we evaluate the feasibility of estimating the magnitude of past temperature changes. We use the finite-difference scheme described by Ketcham [40] to model how retention evolves for two geologic scenarios involving a temperature change. Production rates are scaled and passed to the forward model using the code underlying the CRONUS-Earth online calculator [54]. In one scenario, we model cosmogenic noble gas retention for samples exposed since the last glacial period that experience rapid warming at the beginning of the Holocene. In another scenario, we model cosmogenic noble gas retention for samples exposed over the past 4 Ma that experience cooling across the Plio-Pleistocene climate transition. We allow the pre-transition EDTs to vary in each scenario and hold the post-transition EDT constant to evaluate whether the magnitude of a temperature shift can be resolved as differences in retention. We use both the modeled geologic scenarios and constant production and EDT calculations to discuss potential applications and limitations of cosmogenic noble gas paleothermometry for constraining past Earth surface temperatures.

1.4.2 Cosmogenic ^3He retention in Antarctic erratics

To evaluate whether the existing knowledge of diffusion kinetics for the ^3He -quartz system and the underlying theory are consistent with geologic observations, we measured cosmogenic ^3He abundances in quartz from glacially transported erratic cobbles in the Pensacola Mountains, Antarctica. While not originally collected for this purpose, these samples are useful for the present study because their cosmogenic ^{10}Be exposure ages define a monotonic exposure age-elevation relationship recording progressive deglaciation of this site between 10.6 and 4.8 ka. This relationship, which is commonly observed in similar data sets throughout Antarctica, indicates that each sample was emplaced during deglaciation and has experienced only

a single period of surface exposure, and that the ^{10}Be exposure ages accurately record the duration of this period [e.g. 55, 56]. Thus, given an exposure history determined from the ^{10}Be measurements and an estimate from present climatology of mean ambient temperatures in the Pensacola Mountains (ca. -25 to -30 °C; see discussion below), we compare measured ^3He concentrations with those predicted by Eq. (1.4) to evaluate whether using the open-system behavior of cosmogenic ^3He to reconstruct past temperatures is viable with natural samples.

1.5 Results and Discussion

1.5.1 Effects of temperature, exposure duration, and grain size on cosmogenic noble gas retention

Figs. 1.4A–B show predicted retention, calculated with Eq. (1.3), of cosmogenic ^3He in quartz and ^{21}Ne in orthoclase as a function of time for constant-EDT exposure histories in 1 mm–diameter grains. These figures summarize the respective conclusions of the diffusion studies by Shuster and Farley [22] and Gourbet et al. [21]: cosmogenic ^3He diffusion in quartz is significant at subzero EDTs and relatively short (10^3 yr) timescales, while cosmogenic ^{21}Ne diffusion in orthoclase is significant at EDTs in the 20–40 °C range on 10^5 – 10^6 yr timescales. Importantly, the calculations presented in Figs. 1.4A–B highlight the time and temperature ranges over which paleotemperature information could be constrained by cosmogenic noble gas observations. For example, EDTs ranging from -40 to 20 °C could readily be distinguished with measurements of cosmogenic ^3He retention in 1 mm quartz grains with 10 ka exposure durations. However, for the same grain size and exposure duration, cosmogenic ^{21}Ne is quantitatively retained in orthoclase ($R = 1$) at all EDTs below 40 °C; this nuclide-mineral pair would only display partial retention at typical Earth surface temperatures for exposure durations $> 10^6$ yr. The results of Gourbet et al. [21] imply that cosmogenic ^{21}Ne retention in other alkali feldspars (anorthoclase and sanidine) should be sensitive to a lower temperature range over shorter exposure durations than ^{21}Ne in orthoclase. Available data predict complete retention of cosmogenic ^{21}Ne in quartz at all EDTs and timescales shown in Fig. 1.4, indicating that this nuclide-mineral pair is expected to always accurately record exposure duration.

Broadly, these model results indicate that the ratio of cosmogenic ^3He to a quantitatively retained cosmogenic nuclide in quartz can constrain past surface temperatures in polar and high altitude environments, where EDTs are consistently at or below 0 °C. The concentration of the fully-retained nuclide (e.g., ^{21}Ne , ^{10}Be , or ^{26}Al) constrains the exposure duration, while the concentration of cosmogenic ^3He can be used to determine the EDT. ^{21}Ne measurements in orthoclase can constrain paleotemperature histories at lower latitudes and elevations than the ^3He –quartz system, where EDTs are in the 20–40 °C range.

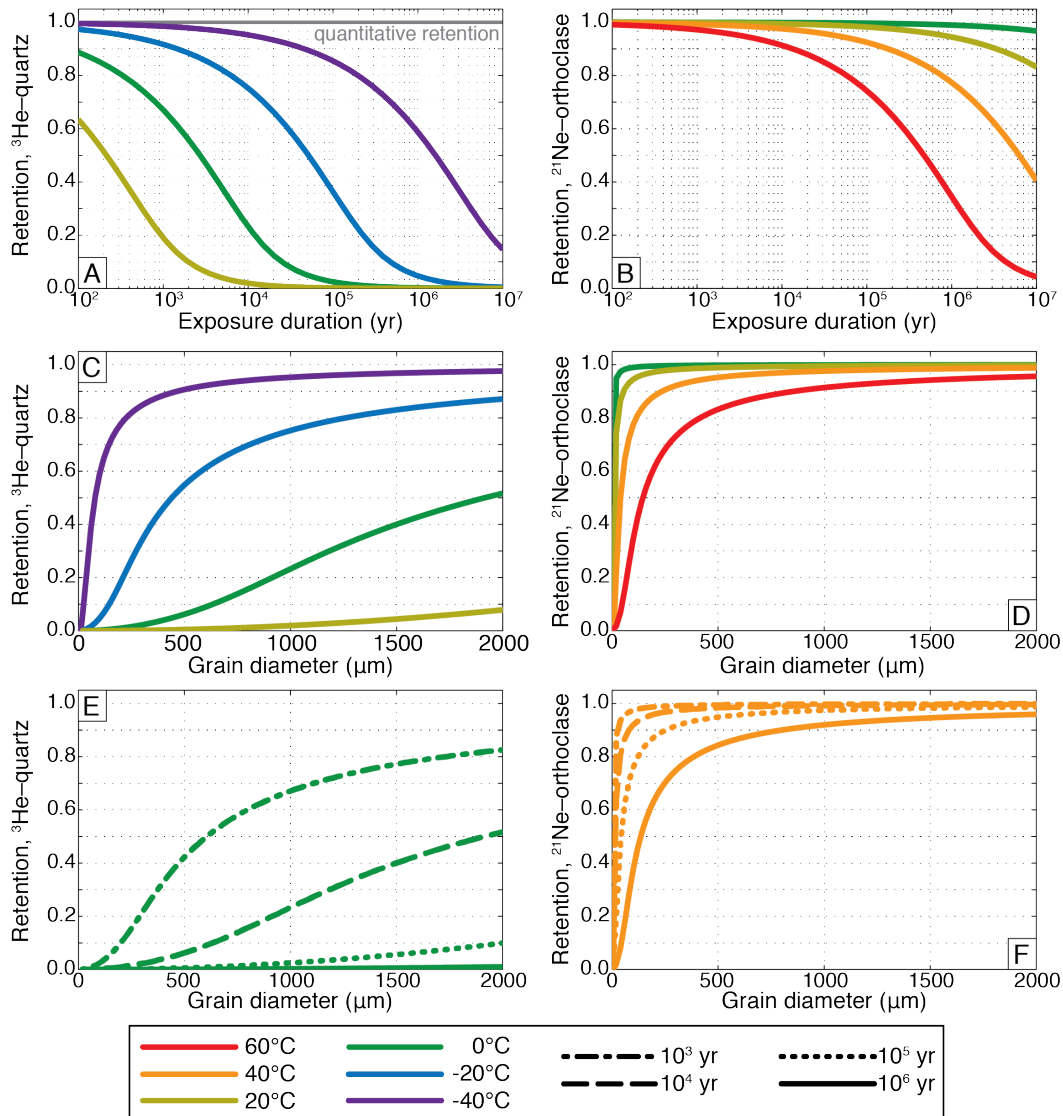


Figure 1.4: Retention of cosmogenic ^3He in quartz (A,C,E) and ^{21}Ne in orthoclase feldspar (B,D,F) using the diffusion kinetics of Shuster and Farley [22] and Gourbet et al. [21], respectively. Retention refers to the fraction of the cosmogenic noble gas produced during exposure that has not diffused from the mineral grain. Curves were calculated using the analytical solution of the production-diffusion equation (Eq. 1.3) assuming a constant effective diffusion temperature (EDT). In (A) and (B), retention is plotted as a function of EDT and exposure duration for 1mm-diameter grains, assuming that the grain size defines the size of the diffusion domain. The line for quantitative retention (i.e. no diffusion during exposure) is also shown in (A). (C) and (D) show retention as a function of EDT and grain size for an exposure duration of 10^4 yr. In (E) and (F), retention is shown as a function of grain size and exposure duration. In (E), retention curves are plotted for an EDT of 0°C ; in (F), the EDT = 40°C .

Retention, and hence the useful temperature range of a particular nuclide-mineral pair, depends on grain size; Figs. 1.4C–F show this effect. Larger grains, corresponding to larger diffusion domains, display higher retentivity at a given EDT and duration for both systems. This is potentially advantageous for paleothermometry because of the possibility of selecting grain sizes to yield maximum sensitivity for particular geologic problems and temperature ranges. For example, while cosmogenic ^{21}Ne is expected to be fully retained in orthoclase at EDTs ≤ 40 °C in 1 mm-diameter grains for 10^4 yr of exposure (Fig. 1.4B), significant temperature–retention differences are predicted for the same scenario in 0.1 mm-diameter grains (Fig. 1.4D). Additionally, observations of retention in different grain sizes can provide an important test for internal consistency: observed retentivities in different grain sizes with a common exposure history should imply a common EDT, as in Fig. 1.4C.

1.5.2 Geologic scenarios involving temperature change

While constant EDT–exposure scenarios are useful for demonstrating the temperature sensitivity of various nuclide–mineral pairs, geologic applications of open-system behavior of cosmogenic noble gases will most likely be aimed at reconstructing past temperature changes. To explore this, we consider two hypothetical geologic scenarios in which the timing of a temperature change is well established but its magnitude in a particular location is not.

A variety of paleoenvironmental and geochemical proxies from marine or lacustrine sediments and ice cores have been used to estimate the magnitude of local and globally-averaged warming at the end of the last glacial period [e.g. 57, 58]. In continental settings, these proxies often only provide qualitative estimates of temperature change [10, 59]. Quantitative estimates of continental temperatures for the last glacial maximum have been made from plant macrofossils and pollen records; however, in many cases these estimates cannot be reconciled with sea surface temperature proxies and climate models to better than 4–8 °C [60] despite nominally having an uncertainty of only 1–2 °C [59, and references therein].

In Fig. 1.5, we show model calculations that evaluate whether cosmogenic noble gas paleothermometry could be used to determine the magnitude of continental temperature increases at the onset of the Holocene. We assume that a sample has been continuously exposed for 16 ka at an erosion rate of 0.5 m/Ma. A single warming event occurs over a 1.2 ka period centered at 12 ka. We consider two cases that are suited to the ^3He –quartz and ^{21}Ne –orthoclase pairs, respectively: Holocene EDTs of 0 °C are typical of high elevations in low to mid-latitude mountainous regions, while EDTs of 60 °C occur in arid deserts where radiative solar heating is significant.

Fig. 1.5 demonstrates that retention of ^3He in quartz and ^{21}Ne in orthoclase is sensitive to the magnitude of Holocene warming in both scenarios. However, for scenarios such as this one in which temperatures increase through time, the sensitivity is relatively small, as the increase in diffusivity caused by climate warming acts to speed up the loss of information about the prior colder period. Retention varies by $< 20\%$ between scenarios in which EDTs during the last glacial period equaled the Holocene EDT and were 15 °C cooler. Assuming that measurements of retention can be resolved with $\pm 2.5\%$ precision, one could determine

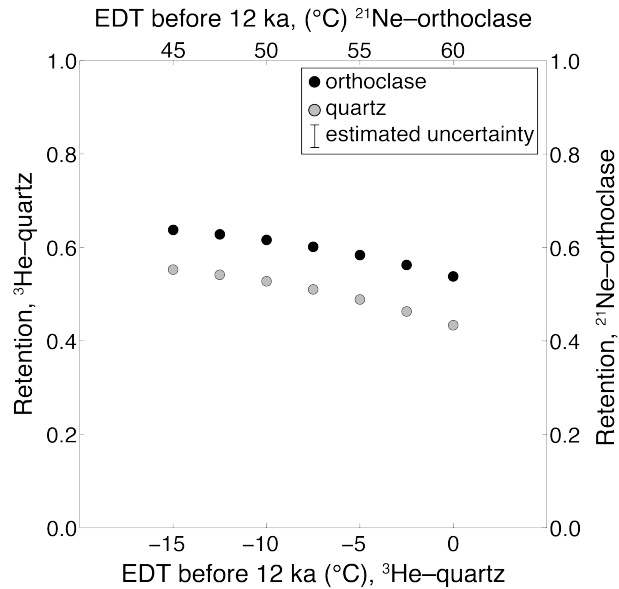


Figure 1.5: Example geologic scenario where cosmogenic noble gas retention is modeled for different magnitude temperature changes at the transition between the last glacial period and the Holocene Epoch. All calculations assume exposure began at 16 ka and warming occurred over a 1.2 ka period centered at 12 ka. Retention of cosmogenic ^3He in quartz (left, gray circles) is plotted against effective diffusion temperature (EDT) before the increase centered at 12 ka (bottom). The predicted ^3He retention corresponds to 2 mm-diameter quartz grains that have experienced an EDT of 0 °C over the Holocene. Retention of cosmogenic ^{21}Ne in orthoclase feldspar (right, black circles) is plotted against EDT before the increase centered at 12 ka (top). The predicted ^{21}Ne retention corresponds to 0.2 mm-diameter orthoclase grains that have experienced an EDT of 60 °C over the Holocene. We assume an average erosion rate of 500 cm/Ma for both systems, although the results are relatively insensitive to erosion rate on this relatively short timescale.

pre-Holocene EDTs (and infer mean Holocene temperatures) to within ± 2.5 °C. In some cases, this would improve upon existing estimates, or provide quantitative constraints where only qualitative estimates presently exist. Measurements of retention across multiple grain sizes could in principle provide greater temperature resolution in this scenario.

Our second scenario involves the Pliocene-Pleistocene climate transition, which is marked by cooling and the onset of northern hemisphere continental glaciation at ~ 2.5 Ma [61–63]. Paleotemperature estimates for the Pliocene are scarce and frequently qualitative, particularly on continental settings and at low latitudes. Cosmogenic noble gas concentrations in rocks in very slowly eroding landscapes that have resided at or near the surface since before ~ 2.5 Ma should record the magnitude of cooling across this transition. Rock surfaces with apparent exposure ages exceeding 2.5 Ma are common in the polar deserts of the

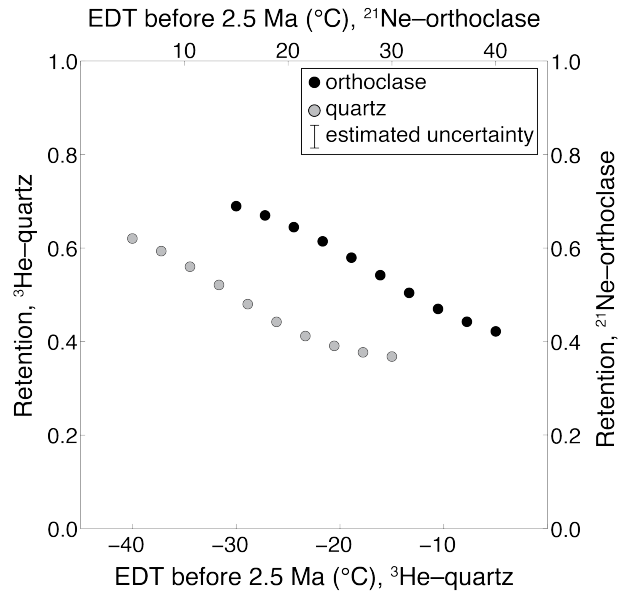


Figure 1.6: Example geologic scenario where cosmogenic noble gas retention is modeled for different magnitude temperature changes at the Pliocene-Pleistocene transition. All calculations assume exposure began at 4 Ma and cooling occurred over a 0.25 Ma period centered at 2.5 Ma. Retention of cosmogenic ^3He in quartz (left, gray circles) is plotted against effective diffusion temperature (EDT) before the decrease centered at 2.5 Ma (bottom). The predicted ^3He retention corresponds to 2 mm-diameter quartz grains that have experienced an EDT of -40°C over the Quaternary Period. Retention of cosmogenic ^{21}Ne in orthoclase feldspar (right, black circles) is plotted against EDT before the decrease centered at 2.5 Ma (top). The predicted ^{21}Ne retention corresponds to 0.2 mm-diameter orthoclase grains that have experienced an EDT of 15°C over the Quaternary. An average erosion rate of 10 cm/Myr is assumed for both systems.

Transantarctic Mountains [19] and the low-latitude deserts of Australia [64], Chile [65, 66], and Namibia [67], and likely exist in other arid and tectonically quiescent regions.

Fig. 1.6 shows predicted retention of cosmogenic ^3He in quartz and ^{21}Ne in orthoclase for an exposure scenario in which samples are continuously exposed for 4 Ma at a constant erosion rate of 0.1 m/Ma. A single cooling event occurs over a 0.25 Ma period centered at 2.5 Ma. We assume the same grain sizes as in the previous example, but EDTs of -40°C for quartz (typical of the Transantarctic Mountains) and 15°C for orthoclase (typical of moderate elevations at temperate latitudes) during the Quaternary. In contrast to the previous example, a scenario in which temperature and therefore diffusivity decreases over time tends to increase the preservation of past temperature information. The same conceptual model could be applied to samples exposed at the surface during the Pliocene and subsequently buried in a sedimentary deposit at depths where cosmogenic production is negligible.

1.5.3 An initial test of cosmogenic noble gas paleothermometry with geologic samples

While diffusion experiments enable predictions of retentivity for a particular cosmogenic noble gas–mineral pair, these predictions have yet to be tested directly with geologic samples. To do this, we measured cosmogenic ^3He and ^{10}Be in nine quartz samples from an elevation transect of glacially transported cobbles in the Pensacola Mountains, Antarctica (Table 1.1; see Tables S1-S3 in Tremblay et al. [68] for additional sample, site, and analytical information). As previously mentioned, all samples have ^{10}Be exposure ages younger than 11 ka that define a monotonic age-elevation relationship, suggesting a single period of surface exposure for each sample as deglaciation progressed during the Holocene [e.g. 56].

Our goal in presenting these data is not to reconstruct a detailed Holocene temperature history for Antarctica. Rather, we use these data to examine whether the temperatures inferred from cosmogenic noble gases agree with the relatively simple climatological and surface exposure histories that we expect for these samples. Thus we make several simplifying assumptions in our analysis and interpretation of this dataset. First, we assume that the ^3He diffusion kinetics determined by Shuster and Farley [22] apply to the quartz samples we analyzed and do not take into account uncertainty in the diffusion kinetics. Second, we do not incorporate production rate uncertainties of either ^3He or ^{10}Be into our analysis. And lastly, although we analyzed quartz grains between 0.25–0.85 mm in diameter (representative of the range of quartz grain sizes in the samples, which are medium to coarse grained sandstones), we assume a representative grain size of 0.5 mm in our calculations. We then use apparent ^3He and ^{10}Be exposure ages and these assumptions to calculate an average EDT for all samples and compare this EDT to that expected from the climatology of the sample location. For future quantitative paleotemperature reconstructions, sample-specific diffusion kinetics and more rigorous quantification of grain size and the $^3\text{He}/^{10}\text{Be}$ production rate ratio will be necessary, since each of our assumptions affects the calculation of an EDT and potentially introduces non-trivial uncertainty into our analysis.

Apparent ^3He exposure ages are systematically younger than ^{10}Be exposure ages of these samples (Fig. 1.7A), consistent with diffusive loss of ^3He at surface exposure temperatures and resulting in ^3He retention of ~ 28 – 63% (Fig. 1.7B). In calculating apparent ^3He exposure ages, we assume that the ^3He observed in our samples is cosmogenic ^3He produced solely during the most recent period of exposure, which is consistent with the simple exposure history inferred from the ^{10}Be exposure ages. Given the diffusion kinetics of ^3He in quartz [22], any non-cosmogenic ^3He present at the time of mineral formation (e.g. from magmatic gases or hydrothermal fluids) is expected to be rapidly lost by diffusion. We applied the finite difference scheme used in section 2.4 to iteratively calculate the EDT that best predicts the observed ^3He retention for each sample; the average EDT for all samples, accounting for measurement uncertainty only, is -13 ± 4 °C (Fig. 1.7C).

The curves in Fig. 1.7A–B show the expected relationship between apparent ^3He exposure age and ^3He retention with exposure duration for several constant EDTs. Although there is an apparent structure in the ^3He retention–exposure age relationship that varies from the

Table 1.1: Cosmogenic ^{10}Be and ^3He concentrations in quartz, apparent surface exposure ages, and implied ^3He retention for glacially transported cobbles from the Pensacola Mountains, Antarctica. Analytical details appear in Supplementary Tables S1-S3 in Tremblay et al. [68]. To calculate exposure ages, we used version 2.2 of the CRONUS-Earth online calculator [54] with the scaling scheme of Stone [69], the production rate calibration dataset of Balco et al. [70] for ^{10}Be , and the production rate estimate of Vermeesch et al. [53] for ^3He . We also assume a rock density of 2.5 g/cm^3 , and an attenuation coefficient of 160 g/cm^2 .

Sample name	Latitude(DD)	Longitude (DD)	Elevation (m)	^{10}Be (10^3 atoms/g) ^b	^3He (10^3 atoms/g)	Apparent exposure ages (yr) ^a		
						^{10}Be	^3He	
10-MPS-077-CRK	-83.6368	-59.0117	488	39.2 ± 1.2	569 ± 106	4837 ± 144	2622 ± 664	0.54 ± 0.14
10-MPS-095-CRK	-83.642	-58.9552	576	50.5 ± 2.5	502 ± 116	5757 ± 281	2139 ± 1997	0.37 ± 0.21
10-MPS-099-CRK	-83.6394	-58.9785	565	56.1 ± 1.5	541 ± 282	6512 ± 176	2349 ± 763	0.36 ± 0.12
10-MPS-120-IBR	-83.8094	-58.8613	632	37.3 ± 1.2	627 ± 115	4114 ± 132	2584 ± 544	0.63 ± 0.13
10-MPS-123-HBS	-83.7455	-58.8309	996	132.4 ± 2.8	1551 ± 132	10612 ± 226	4614 ± 672	0.435 ± 0.064
10-MPS-124-LNK	-83.7596	-59.0759	812	87.3 ± 2.2	886 ± 134	8287 ± 210	3134 ± 743	0.378 ± 0.09
10-MPS-126-LNK	-83.7608	-59.0739	806	87.1 ± 2.2	892 ± 106	8592 ± 213	3278 ± 783	0.382 ± 0.092
10-MPS-128-LNK	-83.7589	-59.0778	755	69.2 ± 2.0	520 ± 130	6853 ± 198	1920 ± 731	0.28 ± 0.11
10-MPS-129-LNK	-83.7589	-59.0778	755	67.7 ± 1.7	575 ± 94	6859 ± 169	2169 ± 638	0.316 ± 0.093

^aUncertainties are ‘internal’ uncertainties including measurement uncertainty only.

^bConcentrations normalized to ‘07KNSTD’ standardization [71]. See supplementary data in Tremblay et al. [68].

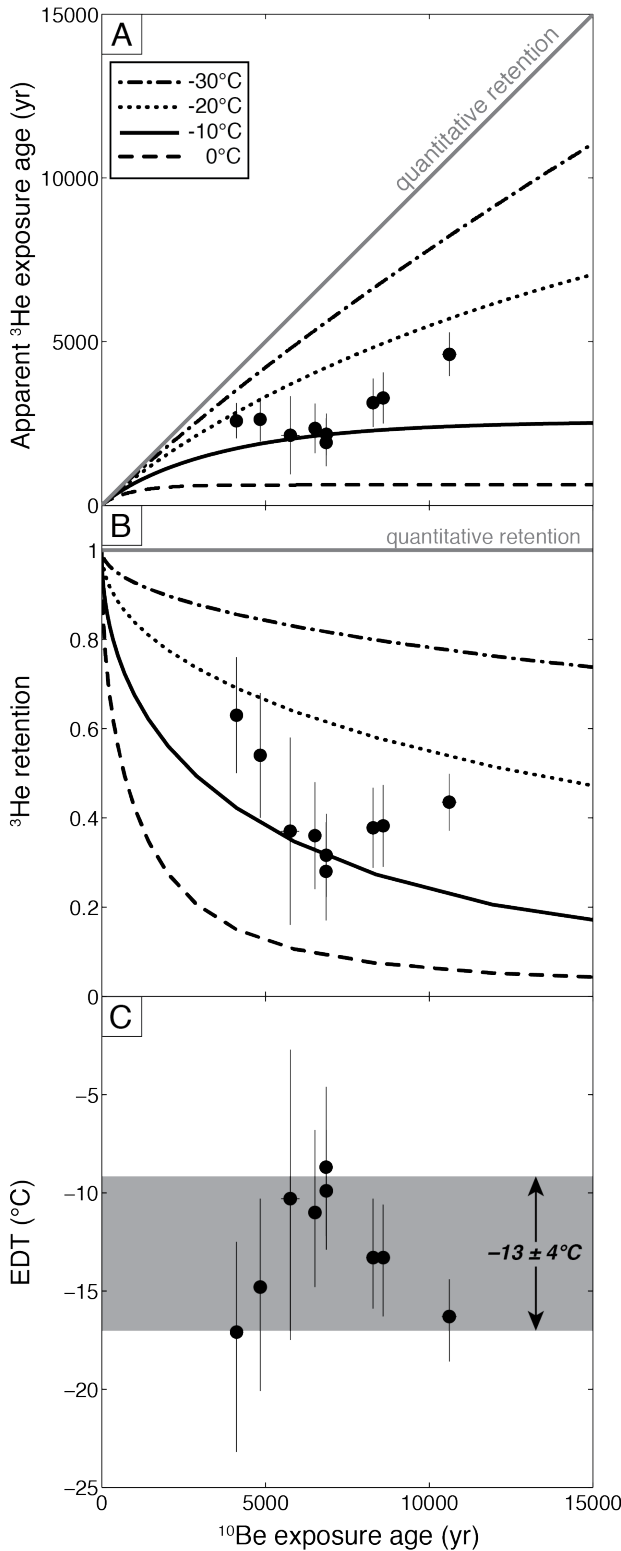


Figure 1.7: Retention of cosmogenic ^3He in glacial erratics with simple Holocene exposure histories from the Pensacola Mountains, Antarctica. ^{10}Be concentrations in quartz constrain the exposure duration of each sample, and we estimated apparent exposure ages from measurements of ^3He in quartz from the same samples and assuming all ^3He was cosmogenic. (A) shows the relationship between the apparent ^3He exposure age and the ^{10}Be exposure age; if no ^3He diffusion occurred, all data points would plot on the line labeled ‘quantitative retention’. (B) shows the relationship between retention of cosmogenic ^3He (apparent ^3He exposure age/ ^{10}Be exposure age) and ^{10}Be exposure age. Uncertainties shown in (A) and (B) include measurement uncertainties only. Uncertainties in ^{10}Be exposure ages are in most cases smaller than the symbol plotted. Curves in (A) and (B) show how apparent ^3He exposure age and retention evolve with time for different effective diffusion temperatures (EDTs), respectively. In (C), we calculated the EDT from the ^3He retention and exposure duration (from the ^{10}Be measurements) of each sample. If we assume that the EDT for all samples is equal and has been invariant over their respective exposure histories, we find an average EDT in the Pensacola Mountains during the Holocene between of $-13 \pm 4^\circ\text{C}$. This corresponds to a mean annual temperature between -25 and -30°C (see text).

expected relationship for a constant EDT of $-13\text{ }^{\circ}\text{C}$, the reduced chi-squared misfit between the observed ^3He retention and that predicted for an EDT of $-13\text{ }^{\circ}\text{C}$ is 1.04, suggesting that most of this variability can be explained by uncertainty in the ^3He measurements. Additional variability may also result from differences in sample-specific diffusion kinetics [72], the grain size distribution of ^3He analysis aliquots, site-specific differences in radiative heating, or some combination therein. Because retention in each sample integrates over its thermal history, it is very unlikely that the apparent structure in the ^3He dataset results from several degree temperature changes over short time intervals (i.e. several hundred years) during the Holocene. This variability is also unlikely caused by a local lapse rate, as katabatic winds prevent typical lapse rates in places like the Pensacola Mountains [73].

Numerous ice core paleotemperature reconstructions for Antarctica show that Holocene temperature changes in inland regions were small [e.g. 74, 75]. Given that mean temperatures in the Pensacola Mountains remained relatively constant over the Holocene, we can compare this average EDT of $\sim -13\text{ }^{\circ}\text{C}$ to mean temperature using the reasoning outlined in section 2.3. The automated weather stations (AWS) from the University of Wisconsin-Madison AWS Program nearest the Pensacola Mountains in latitude and elevation are Elizabeth ($82.6\text{ }^{\circ}\text{S}$, $137.1\text{ }^{\circ}\text{W}$; 549 m), Erin, ($84.9\text{ }^{\circ}\text{S}$, $128.8\text{ }^{\circ}\text{W}$; 990 m), and Harry ($83.0\text{ }^{\circ}\text{S}$, $121.4\text{ }^{\circ}\text{W}$; 954 m). In addition to daily and annual oscillations, temperatures at these sites vary sub-annually, and the amplitude of daily oscillations decreases dramatically from the austral summer to winter. These short-term oscillations and the average mean annual temperature (MAT) at these AWS sites of $-23 \pm 2\text{ }^{\circ}\text{C}$ are likely very similar to those occurring in the Pensacola Mountains. The average EDT for the three AWS sites, calculated from three-hour temperature data collected from 2009 to 2012, is $-16 \pm 1\text{ }^{\circ}\text{C}$. This EDT is consistent with the Holocene EDT estimated from our ^3He retention measurements. Because we have not accounted for the effects of radiative heating on rock temperatures during the austral summer, the difference between MAT and EDT in the Pensacola Mountains may be even greater, suggesting colder MATs in the Pensacola Mountains. This is consistent with MAT estimates from 10 m firn temperatures on the Ronne Ice Shelf (adjacent to the Pensacola Mountains) of $-30\text{ }^{\circ}\text{C}$ [76]. Overall, an estimated modern MAT in the Pensacola Mountains between -25 and $-30\text{ }^{\circ}\text{C}$ is consistent with the Holocene EDT calculated from cosmogenic ^3He measurements in quartz. This result demonstrates that, when combined with the theory and principles applied to radiogenic noble gases, our current knowledge about the production and diffusion of cosmogenic ^3He in quartz are consistent with observations of cosmogenic ^3He in geologic samples exposed at surface temperatures.

1.6 Conclusions

The open-system behavior of cosmogenic noble gases in common minerals like quartz and feldspars can be interpreted using the theory and mathematics applied to radiogenic noble gas thermochronometers and used to reconstruct past Earth surface temperatures. Calculations based on published diffusion kinetics predict that the cosmogenic ^3He –quartz system

is sensitive to subzero temperatures characteristic of high elevation and/or high altitude environments, while the ^{21}Ne -orthoclase system is sensitive to moderate to high temperatures on geologic timescales. Both systems can potentially resolve temperature changes associated with climatic events during the past few million years. Applications of cosmogenic noble gas thermochronometry will require careful consideration of the fundamentally noisy thermal histories rocks experience near Earth's surface, but we demonstrate that short-term temperature fluctuations can be accounted for with effective diffusion temperatures. This new technique should be valuable for corroborating existing paleotemperature proxy records where they exist and expanding their spatial and temporal resolution where they do not.

1.7 Acknowledgements

We thank C. Todd for collecting some of the samples from the Pensacola Mountains as well as M. Vermeulen and M. Hegland for assistance with sample collection and preparation. We appreciate AWS three-hour temperature datasets made available by the University of Wisconsin-Madison AWS Program, supported by the NSF Antarctic Sciences Program (ANT-0944018 and ANT-1245663; <http://amrc.ssec.wisc.edu>). B. Guralnik and an anonymous referee provided detailed reviews that helped clarify this manuscript. We acknowledge support from the NSF Petrology and Geochemistry Program (EAR-1322086), the UC Berkeley Larsen Grant, and the Ann and Gordon Getty Foundation.

Chapter 2

Diffusion kinetics of ^3He and ^{21}Ne in quartz and implications for cosmogenic noble gas paleothermometry

This chapter was previously published in Tremblay, M.M., Shuster, D.L., and Balco, G., *Geochimica et Cosmochimica Acta* **142**, 186–204 (2014). doi:10.1016/j.gca.2014.08.010

2.1 Abstract

The simultaneous production and diffusion of cosmogenic noble gases offers the potential to constrain past temperatures on Earth and other planetary surfaces. Knowledge of both the production rate and diffusion kinetics of cosmogenic nuclide pairs is required to utilize this open-system behavior for paleothermometry. Here, we investigate the diffusion kinetics of spallogenic ^3He and ^{21}Ne in quartz through a series of step-degassing experiments on individual, proton-irradiated quartz grains. Quartz often, but not always, exhibits two stages of linear Arrhenius behavior, with He and Ne exhibiting similar release patterns. This two-stage behavior does not appear to correlate with heating-induced structural changes or anisotropy, nor is it an artifact of proton irradiation; the behavior may instead be associated with radiation damage, mineral inclusions, fluid inclusions, or structural defects. We tentatively interpret these two Arrhenius arrays to represent multiple diffusion domain (MDD)-type behavior in quartz, as two-domain models closely reproduce the experimental data. However, we are currently unable to link this behavior with a clear physical mechanism; a different, more mechanistic model may be more appropriate in future studies.

For both He and Ne, modeled Arrhenius diffusion parameters (activation energy, E_a , and pre-exponential factor, D_0) display a range of values in the quartz samples analyzed. For ^3He , E_a ranges from 73.0 to 99.8 kJ/mol and D_0 from 5.9×10^0 to $1.0 \times 10^4 \text{ cm}^2\text{s}^{-1}$ for the

initial, low-temperature linear Arrhenius arrays; when observed, a second array at higher temperatures corresponds to E_a ranging from 85.2 to 106.4 kJ/mol and D_0 from 1.7×10^{-1} to $3.5 \times 10^0 \text{ cm}^2\text{s}^{-1}$. For ^{21}Ne , E_a ranges from 95.7 to 153.8 kJ/mol and D_0 from 6.6×10^{-1} to $3.2 \times 10^3 \text{ cm}^2\text{s}^{-1}$ for the initial, low-temperature array; linearity at high temperatures is not well constrained, likely because the α - to β - quartz transition occurs during the relevant temperature range. When extrapolated to Earth surface temperatures and geologically relevant timescales, these results suggest that 1 mm-radius quartz grains lose significant amounts of cosmogenic ^3He by diffusion at sub-zero temperatures from the low-retentivity domain over $> 10^3$ yr timescales and from the high-retentivity domain over $> 10^4$ yr, whereas quantitative retention of cosmogenic ^{21}Ne occurs over $> 10^6$ yr at temperatures ≥ 40 °C in most cases. While these results are generally consistent with previously reported studies, they also reveal that sample-specific diffusion parameters are required for quantitative application of cosmogenic noble gas paleothermometry. The cosmogenic ^3He abundance in one quartz sample with a simple Holocene exposure history and the stepwise degassing pattern of cosmogenic ^3He and ^{21}Ne from another quartz sample with a ~ 1.2 Ma exposure history agree well with diffusion experiments on proton-irradiated aliquots of the same samples. For the sample with a simple Holocene exposure history, a production and diffusion model incorporating sample-specific diffusion parameters and the measured ^3He abundance predicts an effective exposure temperature consistent with the mean modern temperature at the sample location. This internal consistency demonstrates that the empirically determined, sample-specific diffusion kinetics apply to cosmogenic ^3He and ^{21}Ne in quartz in natural settings over geologic timescales.

2.2 Introduction

Cosmogenic nuclides, originating from nuclear interactions between secondary cosmic-ray particles and mineral targets in the outermost few meters of the solid Earth, are commonly used to estimate rates and times of geologic processes that modify the Earth's surface [14]. The stable cosmogenic noble gases ^3He and ^{21}Ne have relatively high production rates in common minerals and are cheaper and easier to measure than cosmogenic radionuclides. However, early research into surface exposure dating showed that both ^3He and ^{21}Ne experience diffusive loss at Earth surface temperatures in quartz and feldspars, respectively [17, 22–25]. These authors concluded that open-system behavior renders these cosmogenic noble gas/mineral pairs unfit for surface exposure dating, and they have not been used for this application. However, accurate knowledge of diffusion kinetics would overcome this limitation. In addition, these pairs may be useful as thermochronometers, recording integrated thermal histories of rocks during exposure within a few meters of the surface [68].

Utilizing this open-system behavior requires knowledge of both the production rate and diffusion kinetics of a particular cosmogenic nuclide-mineral pair. For quartz, the sea level high latitude (SLHL) production rate of cosmogenic ^{21}Ne in quartz has been quantified by geologic calibrations and artificial target experiments [e.g. 77–79]. The production rate of

cosmogenic ^3He in quartz is more difficult to empirically quantify from geological samples, given that existing estimates of He diffusion kinetics in quartz as well as comparison between measured concentrations of cosmogenic ^3He and other nuclides indicate diffusive loss at surface temperatures. However, the ^3He production rate in quartz can be estimated from production rates measured in other minerals combined with element-specific reaction cross-sections [28, 80, 81], and has also been directly measured in artificial target experiments [53]. Thus, production rates for these nuclides in quartz are reasonably well established. In contrast, relatively little work has studied mechanisms or kinetics of He and Ne diffusion in quartz.

A common method for quantifying noble gas diffusion kinetics involves step-degassing experiments on crystal fragments. In these experiments, samples are sequentially heated at controlled temperatures and durations, allowing a fraction of the gas present to diffuse from the solid in each heating step. The duration of, and gas fraction released in, each heating step can be used to calculate lengthscale-normalized diffusion coefficients, D/a^2 , at each temperature [82]. This method requires that: (1) diffusion is Fickian and isotropic [83], (2) the diffusant has a known initial distribution, and (3) the diffusion domain has fixed geometry. If the temperature dependence of diffusion follows an Arrhenius law, then the natural logarithm of the calculated diffusivities $\ln(D/a^2)$ will correlate linearly with inverse absolute temperature. The diffusion parameters of activation energy, E_a , and pre-exponential factor, D_0 , can be quantified from the slope and y-intercept, respectively, of a linear regression through an Arrhenius array, and given the further assumption of Arrhenius behaviour at all temperatures then used to calculate diffusivity at any temperature. Noble gas diffusion kinetics have also been quantified by inward diffusion experiments [e.g. 20, 84] and implantation experiments [20, 85]. These experiments are fundamentally different from step-degassing experiments because they occur over extremely small distances (hundreds of nm) and can thus avoid sample heterogeneities like defects and inclusions. Geologic applications of cosmogenic noble gas measurements, however, requires quantifying noble gas diffusion across the grain scale of natural samples, which often include such heterogeneities. Degassing experiments provide an empirical quantification that includes such complexity and are thus employed here.

To our knowledge, only two published sets of step-degassing experiments fully quantify the diffusion kinetics of ^3He and ^{21}Ne in quartz. Trull et al. [23] measured diffusivities of cosmogenic ^3He in quartz that indicate quantitative retention of ^3He in large (> 2 mm) quartz grains on 10^6 yr timescales. Using aliquots of gem-quality quartz containing a uniform distribution of proton-induced ^3He and ^{21}Ne , Shuster and Farley [22] measured diffusion kinetics that predict quartz grains with diameters > 1 mm will retain Ne at most Earth surface temperatures but will experience significant diffusive loss of He at subzero temperatures on $> 10^2 - 10^3$ yr timescales. Their results also suggest that the Trull et al. [23] experiments may have been compromised by partial diffusive loss of cosmogenic ^3He . However, it is unclear whether noble gas diffusion kinetics in gem-quality quartz is applicable to commonly occurring quartz with variable physical characteristics. For example, Niedermann et al. [86] estimated an activation energy for ^{21}Ne diffusion in quartz that is significantly lower

than that determined by Shuster and Farley [22]. Similarly, Trull et al. [26] observed that late-Pleistocene and Holocene-aged quartz samples from Death Valley, California, despite some of the highest surface temperatures on Earth, retain significantly more cosmogenic ^3He than expected from the diffusion parameters of Shuster and Farley [22]. These observations indicate that the diffusion kinetics of ^3He and ^{21}Ne may vary significantly amongst natural quartz samples.

Here we investigate the diffusion kinetics of ^3He and ^{21}Ne in quartz through degassing experiments on a suite of proton-irradiated fragments of natural quartz samples. Using the range of observed diffusion parameters, we model how concentrations of cosmogenic ^3He and ^{21}Ne evolve as a function of exposure duration and temperature at the Earth's surface and explore how retention of both cosmogenic nuclides can vary amongst different quartz samples. We also pair the proton-induced ^3He and ^{21}Ne experiments with measurements of cosmogenic ^3He and ^{21}Ne abundances to evaluate whether the diffusion kinetics observed in the laboratory accurately quantify temperature records integrated over a sample's cosmogenic exposure history.

2.3 Methods

2.3.1 Proton irradiation

To quantify the variability of He and Ne diffusion kinetics in quartz, we conducted step-degassing experiments on a suite of quartz samples, originally collected for cosmogenic exposure dating, that span a range of petrologic origins and geologic histories. Sample descriptions are provided in Table 2.1; photographs of the quartz fragments used in diffusion experiments are shown in Fig. S1 of Tremblay et al. [87]. Step-degassing experiments require a measurable abundance and known distribution of the diffusant at the start of the experiment. To achieve this, we irradiate our samples with energetic protons, which generates uniform distributions of ^3He and ^{21}Ne in quartz through similar nuclear transmutations as those induced by cosmic rays but with at least ten orders of magnitude higher production rates [22, 88]. Aliquots of quartz samples were irradiated with a ~ 220 MeV proton beam for ~ 5 hours at the Francis H. Burr Proton Therapy Center at the Massachusetts General Hospital [88]. Samples CarBZ and UB09-4 were irradiated in April 2013 with a total fluence of $\sim 8.5 \times 10^{15}$ p/cm^2 ; all other samples were irradiated in April 2011 with a total fluence of $\sim 1.0 \times 10^{16}$ p/cm^2 . As we show later, the abundance of cosmogenic ^{21}Ne and ^3He in some natural samples that have experienced exceptionally long (e.g., millions of years) exposure durations can be high enough to support step-degassing experiments on multi-grain quartz aliquots. However, the much higher abundance attainable by proton irradiation (at least three orders of magnitude greater than non-proton induced components) permits more detailed and more precise measurements on single quartz grains, which reduces complications caused by variation in grain size, shape, and properties. Additionally, and more importantly for ^3He , our existing knowledge of diffusion kinetics predicts that cosmogenic ^3He in natu-

rally irradiated quartz will in most cases be nonuniformly distributed due to diffusive loss at Earth surface temperatures and therefore unsuitable for step-degassing experiments.

Table 2.1: Description of quartz samples studied in diffusion experiments.

Sample name	Description	Apparent exposure age
03-RDY-011-QZH	ice-transported granitic boulder, Transantarctic Mountains	$> 4.9 \pm 1.1$ Ma (^{10}Be) [89] 10.6 ± 0.2 Ma (^{21}Ne) [21]
04-MG-080-BR	quartzofeldspathic gneiss bedrock, Antarctic Dry Valleys	248 ± 27 ka (^{10}Be) 220 ± 25 ka (^{26}Al)
04-RDY-139-STR	vein quartz boulder, Transantarctic Mountains	0.60 ± 0.04 Ma (^{10}Be) 1.188 ± 0.072 Ma (^{21}Ne)
98-PCM-105-MNZ	quartzofeldspathic erratic boulder, Mt. Menzies massif, East Antarctica	$> 5.11 \pm 1.24$ Ma (^{10}Be) 8.76 ± 0.35 Ma (^{21}Ne)
CarBZ	gem-quality quartz, Luis Serra do Ouro Mine, Serra Pelada, Carajas, Brazil	—
HU-08-03	moraine boulder of Miocene welded rhyolite tuff, Huancan Valley, Peru	$12.35 + 0.2/-0.02$ ka (^{14}C , ^{10}Be) [90, 91]
QA-767-Q	phenocryst-rich trachyte, upper part of the Ammonia Tanks Tuff, Yucca Mountain, Nevada USA	605 ± 18 ka (^{21}Ne) [21]
UB09-4	phreatic eruption ejecta cobble of felsic granitoid, Ubehebe volcanic field, Death Valley, California USA	3.3 ± 0.1 ka (^{10}Be) [92]

2.3.2 Stepwise heating and degassing experiments

We screened irradiated quartz aliquots under an optical microscope for large fractures, mineral inclusions, and fluid inclusions. We chose quartz fragments apparently lacking these features and photographed and measured each fragment from multiple sides using a calibrated petrographic microscope (Fig. S1 of Tremblay et al. [87]). Selected fragments were loaded into Pt-Ir alloy envelopes attached to K-type thermocouples and put under vacuum.

Either a 30 W or 70 W diode laser was used to heat each sample, with the laser beam defocused over the Pt-Ir envelope to ensure uniform heating. The thermocouple and laser are connected in a feedback loop with a PID temperature controller, which allows the Pt-Ir envelope temperature to be regulated and measured to within ~ 2 °C.

Each sample was heated over at least fifty consecutive heating steps, including at least two retrograde heating cycles, to temperatures between 70 and 1200–1250 °C, with each step lasting 0.25 to 3 hours. The released gas was purified with a SAES getter, brought to 11 K on temperature-controlled cryogenic trap, and then heated to 33 K and 70 K to release helium and neon, respectively. Each element was measured separately on an MAP 215-50 sector field mass spectrometer in the BGC Noble Gas Thermochronometry Lab. Following the diffusion experiment, each sample was removed from its Pt-Ir packet to examine whether the grain broke during the experiment, re-photographed, and then heated to 1250 °C in a laser chamber to ensure complete degassing. Between six and ten room temperature procedural blanks were periodically measured during each experiment; the magnitude of blank corrections was generally $\leq 10\%$. Aliquots of a manometrically-calibrated air standard were also analyzed after approximately every fifth heating step and used to determine helium and neon sensitivities of the mass spectrometer. Measured air standard helium and neon isotopic compositions were indistinguishable from atmospheric. Blank-corrected ^3He , ^{21}Ne , and $^4\text{He}/^3\text{He}$ measurements from each experimental heating step are reported in Table S1 of Tremblay et al. [87]; no isobaric interference corrections were necessary. We used the measured release fraction and duration of each heating step to calculate diffusion coefficients using the equations of Fechtig and Kalbitzer [82] as discussed above, assuming that the quartz diffusion domain is represented by the whole crystal fragment and is spherical. The assumption of a spherical geometry is appropriate for fragments with modest aspect ratios if the surface area to volume ratio of the actual diffusion domain and the spherical approximation are equivalent [38, 39], which we determined from our petrographic microscope measurements.

2.3.3 Cosmogenic ^3He and ^{21}Ne measurements

In addition to experiments on proton-irradiated quartz, we performed a similar step-degassing experiment on a non-irradiated aliquot of the Antarctic vein quartz sample 04-RDY-139-STR. This sample is from a high-elevation site in the Transantarctic Mountains (86.50171 °S, 124.48661 °E, 2356 masl) with a very low erosion rate and therefore has unusually high natural concentrations of cosmogenic ^{21}Ne and ^3He . The precise exposure history of this sample is unknown and, based on cosmogenic ^{26}Al and ^{10}Be concentrations, most likely includes multiple periods of exposure and burial. We measured bulk concentrations of ^{20}Ne , ^{21}Ne , and ^{22}Ne in this sample using the method described in Balco and Shuster [78] and found a total ^{21}Ne concentration of 288.2 ± 3.5 Matoms/g. Ne isotope ratios in three heating steps were indistinguishable from the atmospheric-cosmogenic mixing line [86, 93], and the assumption of two-component mixing implies that the sample contains 199.1 ± 3.7 Matoms/g cosmogenic ^{21}Ne and 89.0 ± 3.8 Matoms/g ^{21}Ne attributable to trapped Ne with

atmospheric composition (Table S2, Fig. S2 in Tremblay et al. [87]). This concentration of cosmogenic ^{21}Ne implies an apparent exposure age of ~ 1.25 Ma. From a crushed but otherwise unprocessed fraction of this sample that had been stored at room temperature since collection in 2004, we picked 0.0753 g of quartz fragments (~ 100 grains) similar in size to the proton-irradiated grain analyzed in the single-grain step-degassing experiment. We sequentially heated and degassed this multi-grain aliquot following the same procedure as described above, but loaded the sample into a large tantalum packet rather than the small Pt-Ir packets used for single grain experiments on proton-irradiated quartz. We then compared calculated D/a^2 values from the proton-irradiated and cosmogenic experiments to test whether the diffusion kinetics of proton-induced ^3He and ^{21}Ne are consistent with the observed degassing profiles of cosmogenic ^3He and ^{21}Ne . Blank-corrected ^3He and ^{21}Ne measurements from each heating step in this experiment are reported in Table S3 of Tremblay et al. [87]. ^{20}Ne and ^{22}Ne signals in individual heating steps were too low to permit accurate Ne isotope ratio measurements due to isobaric interferences [86] and are therefore not reported.

We also tested whether the diffusion kinetics determined from our experimental results are representative of natural geologic conditions by measuring bulk cosmogenic ^3He abundances in six aliquots of quartz from sample HU-08-03. HU-08-03 was collected from a boulder of rhyolitic ignimbrite on the Huancane IIa moraine of the Quelccaya Ice Cap in Peru (13.9461 $^{\circ}\text{S}$, 70.8927 $^{\circ}\text{W}$, 4862 masl; [90, 91]) for cosmogenic-nuclide production rate calibration during the CRONUS-Earth project. This moraine is radiocarbon-dated at 12,350 cal yr BP [90]. Geological evidence and concentrations of other cosmic-ray-produced radionuclides indicates that the sample was emplaced at this time and subsequently experienced a single period of exposure at its present location [91]. As with sample 04-RDY-139-STR discussed above, we separated quartz from a fraction of this sample that had been crushed but not otherwise processed, and had been stored at room temperature since collection. Quartz aliquots of 100–200 mg were packaged in tantalum packets, placed under vacuum in a sample chamber, and heated with a 70 W diode laser to either 700 or 1200 $^{\circ}\text{C}$ for 1 hr. Repeat extractions at either temperature yielded He signals indistinguishable from blank measurements. We analyzed the helium released during heating according to the techniques described above. However, these analyses released large quantities of ^4He in addition to ^3He , which resulted in the total He pressure in the mass spectrometer being outside the calibration range attainable with available standard gas pipettes. To account for this, we introduced a ^3He spike into the mass spectrometer after several peak-hopping measurement cycles and used the difference in ^3He signals at the time of spike inlet between samples and standards to correct for nonlinearity. Having corrected for nonlinearity in this way, we then applied a blank correction as described above. We propagated (sometimes large) uncertainties associated with both nonlinearity and blank corrections, and averaged results from six aliquots to estimate the total ^3He concentration. In order to evaluate this ^3He concentration in the context of this sample’s known exposure age [91], we assume that all ^3He is cosmogenic.

2.3.4 Sample characterization

Numerous factors can lead to variable diffusion kinetics and complex Arrhenius diffusive behavior for a given mineral-diffusant pair, including anisotropy [e.g. 94], temperature-induced structural transformations [e.g. 95], accumulation of radiation damage [e.g. 96–98], the presence of mineral and/or fluid inclusions [e.g. 84], and crystallographic defects [e.g. 36, 99]. The effects of the former three factors can be determined or at least approximated based on the results from diffusion experiments. We carried out several ancillary analyses in order to evaluate whether the latter two factors influenced the diffusion kinetics observed in our samples.

Although very large fluid and mineral inclusions readily visible under the binocular microscope were avoided, smaller ($\leq 20 \mu\text{m}$) inclusions were difficult to recognize by visual inspection in the relatively large quartz fragments with pronounced conchoidal fracturing chosen for experiments. We made grain mounts of 20–50 quartz fragments from each sample and examined the mounts both on an optical petrographic microscope and a Zeiss EVO scanning electron microscope (SEM) in the backscattering mode in order to characterize the relative abundances and types of inclusions characteristic of each sample.

To evaluate whether the observed diffusion kinetics relate to crystallographic defects and/or mineral and fluid inclusions, we also measured the concentrations of several trace elements in our samples. Crystallographic point defects and dislocations in quartz are often associated with the presence of trace elements, which can both substitute for silicon in the structural configuration or interstitially occupy c-axis channels [e.g. 100, 101]. For example, Al^{3+} commonly substitutes for structural Si^{4+} , and an alkali metal like Li^+ , Na^+ , or K^+ occupies the adjacent interstice for charge compensation, creating an $[\text{AlO}_4^- | M^+]^0$ point defect [e.g. 100, 102]. Although less common, Fe^{3+} and Ti^{4+} also substitute for Si^{4+} in quartz. Mineral and fluid inclusions in quartz can also contain significant concentrations of Na and K as well as Ca, Mg, and Mn [101]. To measure trace element concentrations, we dissolved several-hundred-milligram aliquots of quartz from each sample in hydrofluoric acid. We added a small amount of 1% sulfuric acid to each sample solution and then heated the solutions to remove Si by evaporating SiF_4 while keeping the elements of interest in solution. We then diluted each sample to achieve a 1% HNO_3 , 1% H_2SO_4 solution for analysis. Bracketing standard solutions containing Al, Ca, Fe, K, Li, Mg, Mn, Na, and Ti were made with the same matrix (1% HNO_3 , 1% H_2SO_4), and sample concentrations were measured by comparison with these standard solutions on a Perkin Elmer 5300 DV inductively coupled plasma optical emission spectrometer (ICP-OES) in the College of Natural Resources at UC Berkeley.

2.4 Results

2.4.1 Step-degassing experiments on proton-irradiated quartz

Arrhenius plots are shown for step-degassing experiments on proton-irradiated fragments of HU-08-03 (Fig. 2.1), QA-767-Q(1) (Fig. 2.2), and UB09-4 (Fig. 2.3). These three experiments span the range of observed Arrhenius behavior and diffusion parameters; Arrhenius plots for all experiments, including a replicate experiment on sample QA-767-Q, are shown in the supplementary materials (Figs. S3-S8) of Tremblay et al. [87].

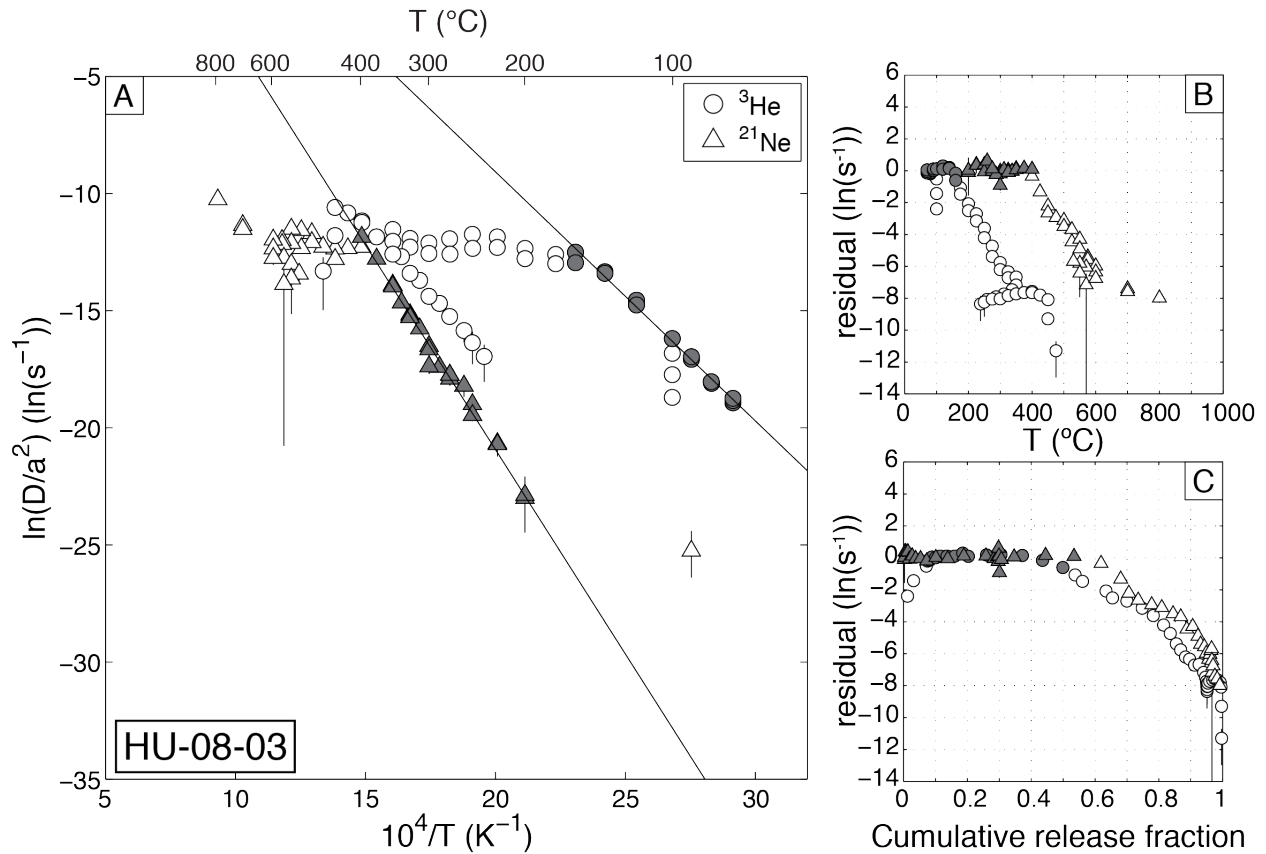


Figure 2.1: Arrhenius plot (A) and residual plots (B-C) for diffusion of proton-induced ^3He (circles) and ^{21}Ne (triangles) in quartz from sample HU-08-03, a rhyolitic moraine boulder from Peru. Calculated $\ln(D/a^2)$ for each temperature step are shown, although in most cases the uncertainty is smaller than the symbol. Uncertainties in $\ln(D/a^2)$ were estimated using a Monte Carlo approach (see text). Linear regressions were fit through the filled symbols in (A) and used to calculate E_a and $\ln(D_0/a^2)$, with uncertainties propagated from the Monte Carlo scheme. The difference between the $\ln(D/a^2)$ calculated for each heating step and that predicted by the linear regression is plotted as a residual against temperature (B) and cumulative release fraction (C). Filled symbols correspond to those in (A).

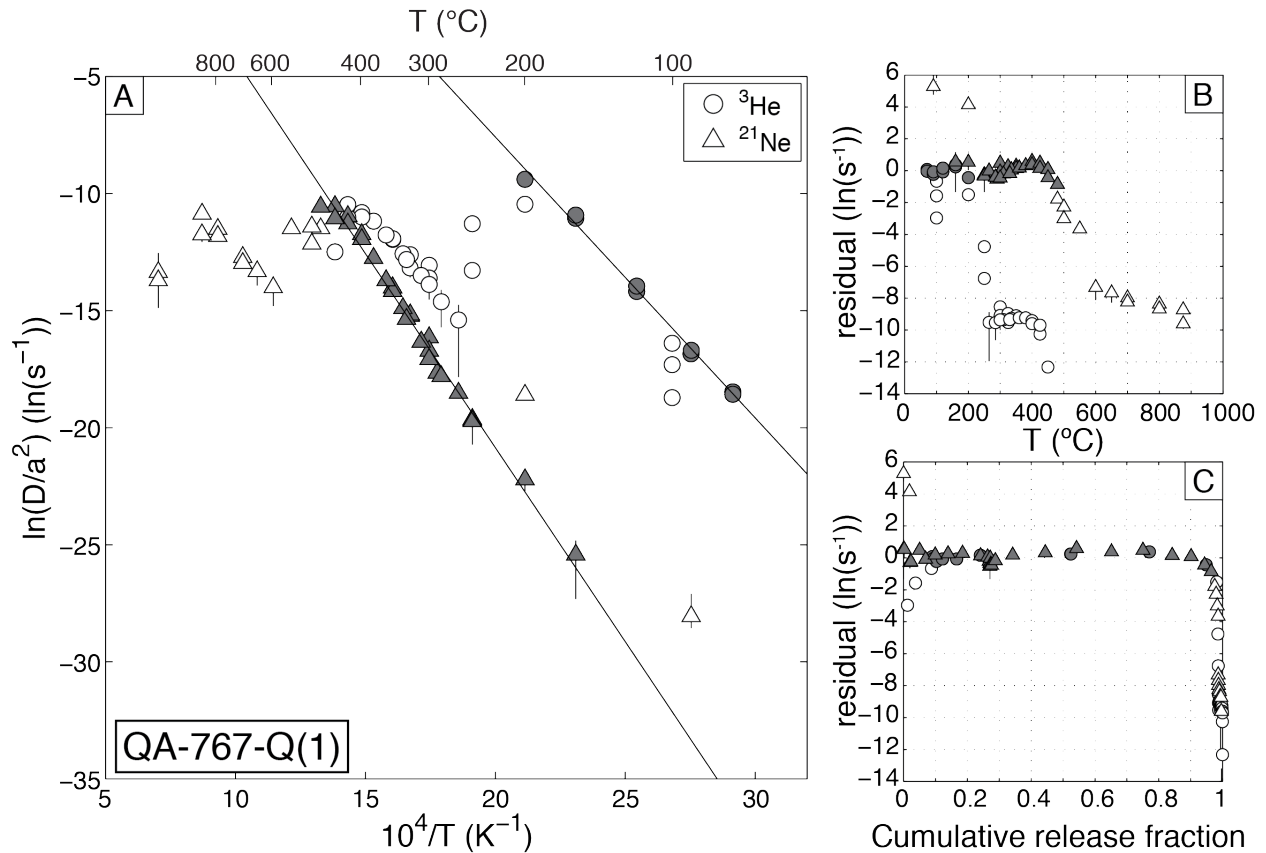


Figure 2.2: Arrhenius plot (A) and residual plots (B-C) for diffusion of proton-induced ^3He (circles) and ^{21}Ne (triangles) in quartz from sample QA-767-Q(1) of the Ammonia Tanks Tuff, Yucca Mountain USA.

Because the equations of Fechtig and Kalbitzer [82] use the cumulative gas release fraction to calculate diffusivities, linear propagation of uncertainties in cumulative gas release fraction from our step heating experiments would result in unrealistically large uncertainties in diffusivities. To address this, uncertainties in the calculated diffusivities of ^3He and ^{21}Ne for each heating step were propagated using a Monte Carlo approach, whereby we generated 30,000 normally distributed, random datasets using the analytical uncertainties in measured ^3He and ^{21}Ne to calculate a range of permissible D/a^2 values. We fit least squares regressions through a subset of the data points in each Arrhenius plot (see below) and used the Monte Carlo-derived uncertainties in D/a^2 to estimate uncertainties in E_a and $\ln(D_0/a^2)$ for both ^3He and ^{21}Ne . We also plot the residuals, or differences between the calculated diffusivity of ^3He and ^{21}Ne at each heating step and the expected diffusivity at the same temperature from the Arrhenius linear regressions, as a function of temperature (Fig. 2.1B–2.3B) and cumulative release fraction (Fig. 2.1C–2.3C).

Simple, linear Arrhenius behavior was not observed in most experiments. Instead, two

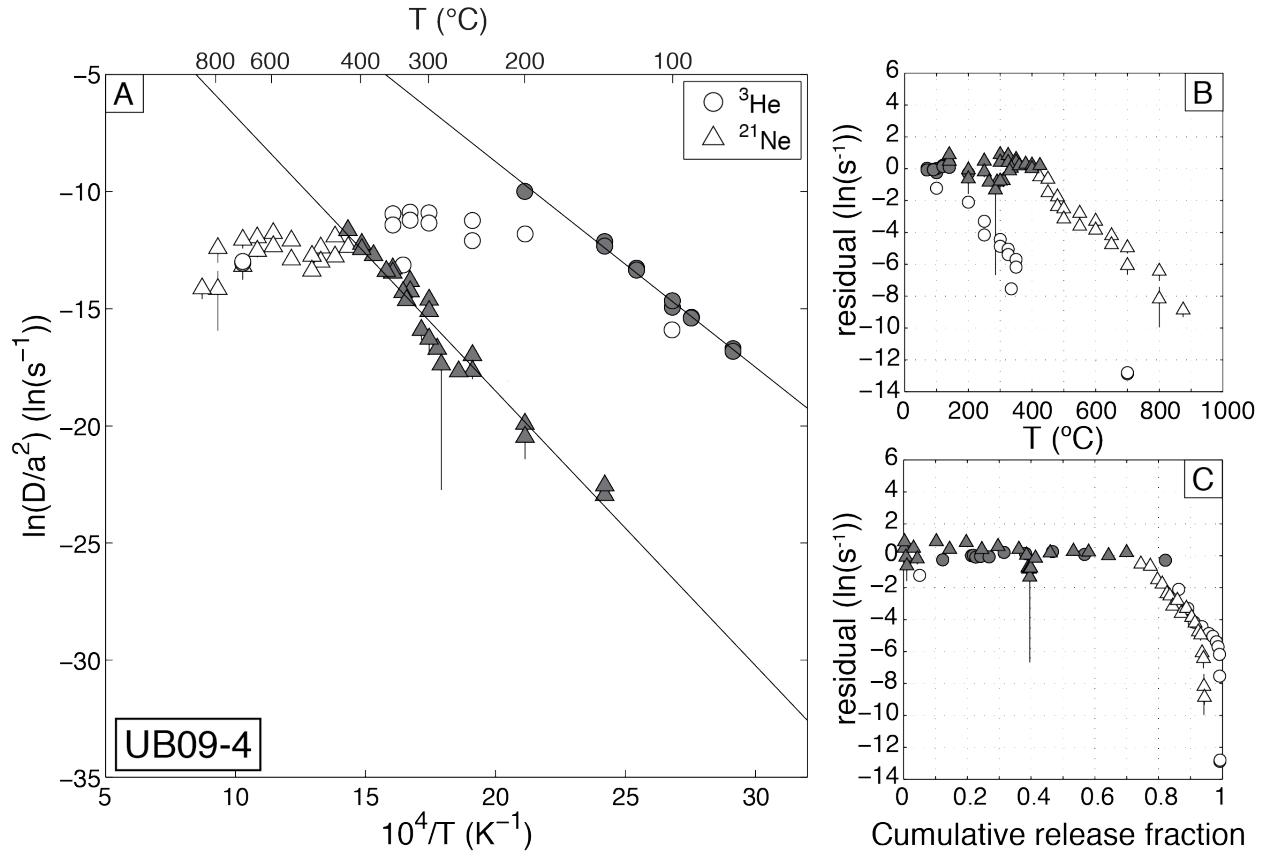


Figure 2.3: Arrhenius plot (A) and residual plots (B-C) for diffusion of proton-induced 3He (circles) and ^{21}Ne (triangles) in quartz from sample UB09-4, a felsic granitoid ejecta cobble from a phreatic eruption in the Ubehebe volcanic field, Death Valley, California USA.

linear Arrhenius arrays were observed for both 3He and ^{21}Ne in six of the nine step-degassing experiments: one at lower temperatures and one at higher temperatures, separated by a transition zone where diffusivity changes relatively little with increasing temperature (Fig. 2.1A-2.2A). When fitting least squares regressions, we followed an approach similar to those of Gourbet et al. [21] and Cassata and Renne [95]. We attempted to include data from as many temperature steps as possible that make up a linear Arrhenius array while minimizing the residuals (e.g. Fig. 2.1B-C) between the regression and the data. Typically, prograde steps with residuals $\geq 1 \ln(s^{-1})$ from the least squares regression through the preceding sequential steps and retrograde steps with residuals $\geq 2 \ln(s^{-1})$ from the least squares regression through the preceding and following prograde steps were excluded from fits. For 3He , the first few temperature steps at 100 $^{\circ}C$, which represent $\leq 9\%$ of the total 3He yield, exhibit increasing apparent diffusivities. This is likely due to minor diffusive loss of 3He either during or after the proton irradiation [22]; to minimize potential bias from this effect, we also exclude these steps from the regressions.

Table 2.2: Summary of ^3He quartz diffusion parameters. 1σ uncertainties are reported.

Sample	SR ^c (μm)	^3He , low-temperature array ^a			^3He , high-temperature array ^b		
		E_a (kJ/mol)	\pm	$\ln(D_0/a^2)$ ($\ln(s^{-1})$)	E_a (kJ/mol)	\pm	$\ln(D_0/a^2)$ ($\ln(s^{-1})$)
03-RDY-011-QZH	252	96.3	2.3	15.4	0.6	—*	—*
04-MG-080-BR	328	95.4	1.0	12.8	0.3	92	17
04-RDY-139-STR	426	96.6	0.7	13.8	0.2	93.0	1.9
98-PCM-105-MNZ	349	97.5	0.6	15.1	0.2	90.9	7.4
CarBZ	388	75.3	0.6	9.6	0.2	—*	—*
HU-08-03	256	88.5	1.1	12.2	0.3	98.8	6.6
QA-767-Q (1)	280	99.8	2.1	16.4	0.6	106.4	13.4
QA-767-Q (2)	306	99.6	0.4	15.2	0.1	85.2	16.6
UB09-4	299	73.0	0.8	8.8	0.2	—*	—*

^aIn cases where two linear Arrhenius arrays were observed during an experiment, these values correspond to the linear Arrhenius array observed at lower temperatures.

^bIf observed, these values correspond to the linear Arrhenius array observed at higher temperatures.

^cRadius of a sphere with a surface to volume ratio approximately equal to that of the quartz analyzed based on measured cross-dimensions of each quartz fragment. Images of proton-irradiated quartz fragments are shown in Fig. S1. of Tremblay et al. [87]

Table 2.3: Summary of ^{21}Ne quartz diffusion parameters. 1σ uncertainties are reported.

Sample	SR ^c (μm)	^{21}Ne , low-temperature array ^a			^{21}Ne , high-temperature array ^b		
		E_a (kJ/mol)	\pm	$\ln(D_0/a^2)$ ($\ln(\text{s}^{-1})$)	E_a (kJ/mol)	\pm	$\ln(D_0/a^2)$ ($\ln(\text{s}^{-1})$)
03-RDY-011-QZH	252	101.4	7.6	6.5	1.5	—*	—*
04-MG-080-BR	328	136.6	12.5	14.9	3.0	—*	—*
04-RDY-139-STR	426	107.7	4.0	5.9	0.8	126.8	6.0
98-PCM-105-MNZ	349	121.8	6.6	9.8	1.4	—*	—*
		116.5	4.5	8.4	0.9	—*	—*
		121.3	5.6	9.9	1.2	—*	—*
CarBZ	388	143.9	3.3	14.1	0.7	—*	—*
HU-08-03	256	145.2	8.3	14.0	1.7	90.6	9.7
QA-767-Q (1)	280	139.9	4.9	12.8	0.9	89.4	17.6
QA-767-Q (2)	306	153.8	6.5	16.6	1.3	—*	—*
UB09-4	299	95.7	1.9	4.5	0.4	—*	—*

^aIn cases where two linear Arrhenius arrays were observed during an experiment, these values correspond to the linear Arrhenius array observed at lower temperatures. For 04-RDY-139-STR and 98-PCM-105-MNZ, we report two sets of ^{21}Ne diffusion kinetics. The first set of diffusion kinetics corresponds to the largest subset of ^{21}Ne data that forms a low-temperature linear array. The second set of diffusion kinetics corresponds to a smaller subset of the ^{21}Ne data that forms a low-temperature linear array with a better linear fit. Filled data points in Figs. S5 and S6 of Tremblay et al. [87] were used to calculate the first set of diffusion kinetics.

^bIf observed, these values correspond to the linear Arrhenius array observed at higher temperatures. For ^{21}Ne , diffusion parameters are only shown for the high-temperature linear array if the ^{21}Ne release fraction is equivalent to the release fraction of ^3He making up a high temperature linear array in the same experiment.

^cRadius of a sphere with a surface to volume ratio approximately equal to that of the quartz analyzed based on measured cross-dimensions of each quartz fragment. Images of proton-irradiated quartz fragments are shown in Fig. S1. of Tremblay et al. [87]

The linear Arrhenius arrays and transition zones occur over different temperature ranges for ^3He and ^{21}Ne (Fig. 2.1B–2.2B). However, with the exception of sample 04-MG-080-BR the cumulative gas release fractions comprising the low-temperature linear arrays in each experiment are nearly equivalent for ^3He and ^{21}Ne (Fig. 2.1C–2.2C); in other words, divergence from the low-temperature linear arrays occur at the same gas release fraction, but not the same temperature, for He and Ne. Between different quartz samples, the proportion of ^3He and ^{21}Ne within the the low-temperature linear arrays varies greatly, ranging from 50% for HU-08-03 (Fig. 2.1C) to $> 95\%$ for QA-767-Q(1) (Fig. 2.2C). Likewise, plots of the residuals versus temperature for HU-08-03 (Fig. 2.1B) and QA-767-Q(1) (Fig. 2.2B) reveal that the temperatures ranges over which we observed linear Arrhenius behavior of ^3He and ^{21}Ne vary between samples. Higher-temperature linear Arrhenius arrays are well defined for ^3He and represent as much as 20% of the cumulative gas release fraction. We report calculated diffusion parameters and sample dimensions for all experiments in Tables 2.2 and 2.3, and include E_a and $\ln(D_0/a^2)$ estimates for these second linear arrays when observed. We report a second set of ^{21}Ne diffusion kinetic parameters for three of these experiments in which the proportions of ^3He and ^{21}Ne in the higher temperature linear Arrhenius arrays are equivalent (Table 2.3).

A single linear Arrhenius array was apparent in the experiment on sample UB09-4 (Fig. 2.3). More than 80% of the ^3He and ^{21}Ne released in the UB09-4 experiment makes up a linear Arrhenius array, with the remaining $< 20\%$ deviating from the linear trend and without ever forming a second linear array at higher temperatures (Fig. 2.3A, 2.3C). Single linear Arrhenius arrays were also observed in experiments on quartz from 03-RDY-011-QZH (Fig. S3 in Tremblay et al. [87]) and CarBZ (Fig. S7 in Tremblay et al. [87]), although there is an apparent second ^{21}Ne linear array for CarBZ at high temperatures. The activation energies of ^3He and ^{21}Ne diffusion calculated for these samples are in several cases significantly lower than those calculated for the first linear Arrhenius array in experiments where two arrays were observed. To summarize, we observed two well-defined Arrhenius arrays in the He data from six of our nine experiments; in the other three experiments, we observed only a single Arrhenius array. For the Ne data, we observed two distinct arrays in three experiments, and only a single array in the other six. When we observed two arrays in the Ne data we also observed two arrays in the He data, but the reverse is not the case.

Fig. 2.4 shows the range of Arrhenius relationships we observed for ^3He and ^{21}Ne , both for the low-temperature linear arrays and for the high-temperature linear arrays when present. For the low-temperature arrays, ^3He activation energies range from 73.0 to 99.8 kJ/mol and the pre-exponential factor, D_0 , ranges from 5.9×10^0 to $1.0 \times 10^4 \text{ cm}^2\text{s}^{-1}$. When observed, the second linear array at higher temperatures corresponds to ^3He activation energies ranging from 85.2 to 106.4 kJ/mol and D_0 values ranging from 1.7×10^{-1} to $3.5 \times 10^0 \text{ cm}^2\text{s}^{-1}$; in most experiments, the activation energies calculated for these second arrays are indistinguishable within uncertainty from the activation energy calculated from the low-temperature arrays. ^{21}Ne activation energies range from 95.7 to 153.8 kJ/mol and D_0 values range from 6.6×10^{-1} to $3.2 \times 10^3 \text{ cm}^2\text{s}^{-1}$ for the low-temperature array. For the three experiments comprising equivalent release fractions for ^3He and ^{21}Ne in the high-temperature linear arrays, ^{21}Ne

activation energies range from 89.4 to 126.8 kJ/mol and D_0 values range from 5.9×10^{-4} to $7.3 \times 10^{-1} \text{ cm}^2\text{s}^{-1}$. For two of these three cases, the activation energies calculated from the high-temperature ^{21}Ne array are inconsistent with those calculated from the low-temperature array. The Arrhenius relationships for ^3He and ^{21}Ne reported by Shuster and Farley [22] and for ^3He reported by Trull et al. [23] are also plotted in Fig. 2.4 for comparison. The simple Arrhenius relationships for ^3He and ^{21}Ne calculated by Shuster and Farley [22] from step-degassing experiments on gem-quality quartz fall within the range of Arrhenius relationships characterized by the low-temperature linear arrays in our experiments. The single linear Arrhenius array observed by Trull et al. [23] is very close to the range linear ^3He arrays we observed at higher temperatures.

2.4.2 Natural cosmogenic ^3He and ^{21}Ne measurements

We observed two linear Arrhenius arrays in the step-degassing experiment carried out on a proton-irradiated fragment of vein quartz sample 04-RDY-139-STR (Fig. S5 of Tremblay et al. [87]). Fig. 2.5 shows the results the step-degassing experiment on an unirradiated, multi-grain quartz aliquot from sample 04-RDY-139-STR, with the results of the proton-irradiated step-degassing experiment plotted for comparison. The calculated diffusivities of cosmogenic ^3He at low-temperature heating steps (85% of the total cosmogenic ^3He) are significantly lower than those of proton-induced ^3He diffusivities at the same temperatures. In contrast, we observed close agreement between cosmogenic and proton-induced ^3He diffusivities at the end of the transition zone and throughout the second, higher temperature linear Arrhenius array observed for proton-induced ^3He (Fig. 2.5A).

Cosmogenic and proton-induced ^{21}Ne diffusivities in sample 04-RDY-139-STR also overlap at higher temperatures (Fig. 2.5B). A small fraction (7%) of the total ^{21}Ne in the cosmogenic experiment degassed at temperatures less than 250 °C; the diffusivities calculated for these steps plot above the proton-induced ^{21}Ne diffusivities at the same temperatures. In principle, if ^{21}Ne produced by proton irradiation is diffusively equivalent to cosmic-ray-produced Ne, we should observe exactly the same diffusion kinetics in natural and proton-irradiated samples. Although this is the case in broad terms, the results of the two experiments differ in detail. As discussed above, bulk Ne isotope ratios in this sample indicate that only 70% of the total ^{21}Ne is cosmic-ray-produced. Differences in the release pattern of cosmogenic and a trapped atmospheric ^{21}Ne component in this sample could therefore potentially explain differences between the two experiments. However, as noted above, amounts of Ne released in individual heating steps in the experiment on naturally irradiated quartz were too small to accurately separate ^{21}Ne released in each step into cosmogenic and trapped components.

We also observed two linear Arrhenius arrays in the step-degassing experiment on a proton-irradiated quartz fragment from sample HU-08-03, a rhyolite moraine boulder from Peru (Fig. 2.1). Bulk cosmogenic ^3He measurements for six aliquots of unirradiated quartz from this sample yield an average cosmogenic ^3He concentration of 3.75 (± 0.3) Matoms/g; results from each analysis are reported in Table S4 of Tremblay et al. [87]. We estimated

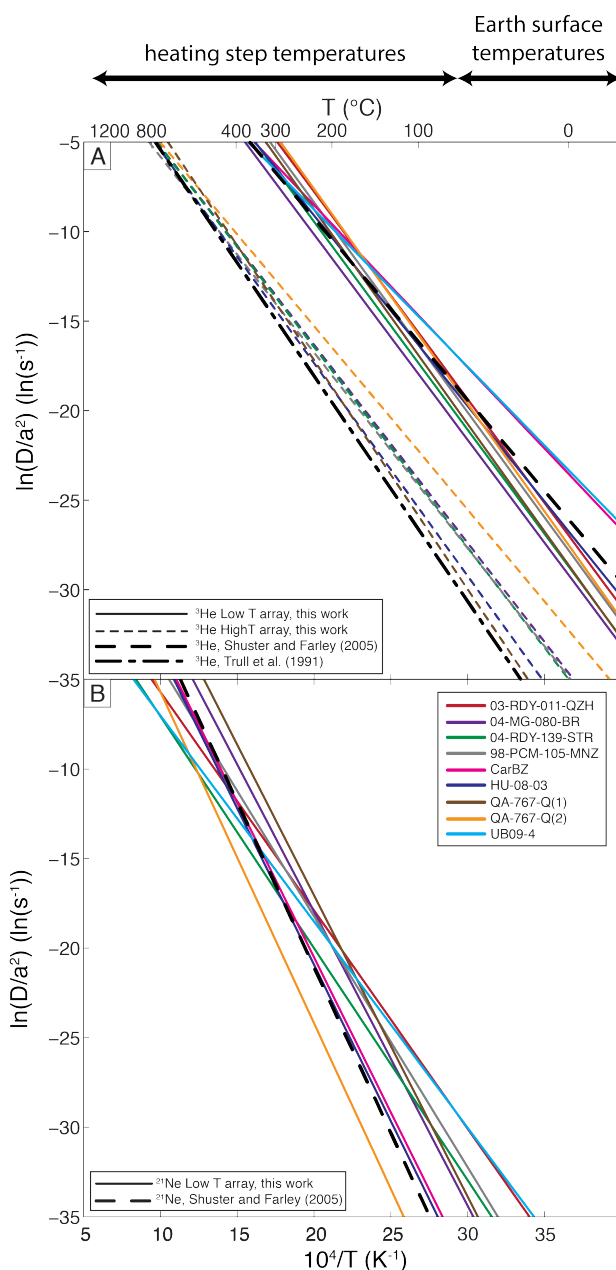


Figure 2.4: Summary Arrhenius plot of the nine quartz diffusion experiments we conducted. In (A), solid color lines correspond to the low-temperature linear arrays and dashed color lines correspond to the high-temperature linear arrays observed for 3He . In (B), the solid color lines correspond to the low-temperature linear arrays observed for ^{21}Ne . Also plotted are the Arrhenius relationships for 3He and ^{21}Ne diffusion in quartz reported by Shuster and Farley [22] (dashed black) and for 3He reported by Trull et al. [23] (dashed-dotted black). Above the Arrhenius plot, the temperature range over which diffusion experiments occur and the temperature range characterizing the Earth's surface is shown.

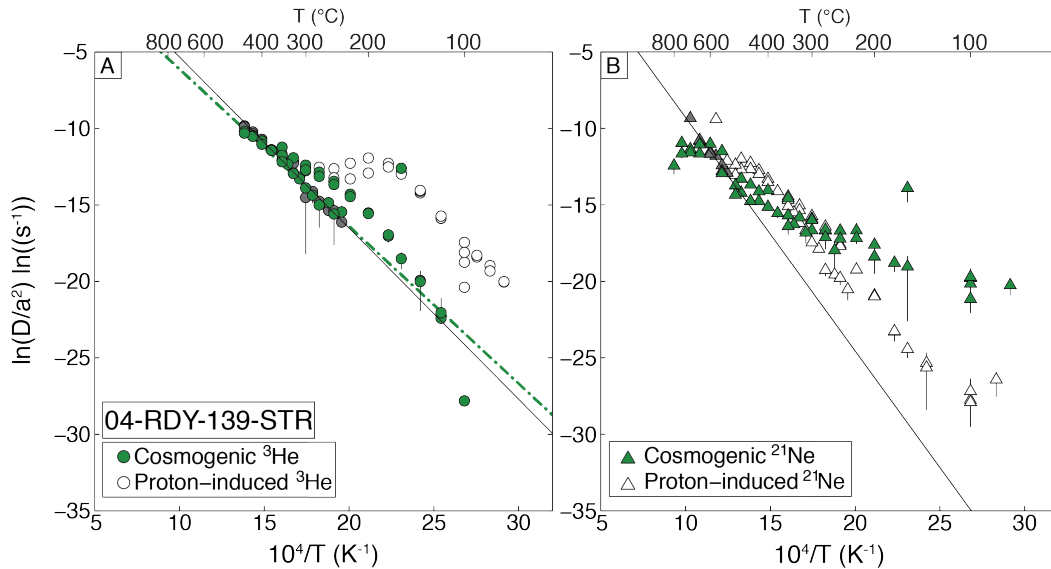


Figure 2.5: Arrhenius plots for proton-induced and cosmogenic ^3He (A) and ^{21}Ne (B) diffusion for Antarctic vein quartz sample 04-RDY-139-STR. Unfilled and grey-filled symbols represent the $\ln(D/a^2)$ values for proton-induced ^3He and ^{21}Ne . Uncertainties are equivalent to those in Fig. S4 in Tremblay et al. [87]. Here, we show with grey-filled symbols the heating steps that we used to calculate E_a and $\ln(D_0/a^2)$ for the higher-temperature linear Arrhenius arrays (Tables 2.2 and 2.3). Linear regressions through these data are also shown. Green-filled symbols show the $\ln(D/a^2)$ values calculated for cosmogenic ^3He and ^{21}Ne . We propagated uncertainty in the cosmogenic $\ln(D/a^2)$ values using the same Monte Carlo approach that we used for the proton-irradiated experiments. The dashed-dotted green line in (A) shows the linear regression through the cosmogenic ^3He measurements corresponding to the same steps as the proton-induced ^3He measurements used to calculate E_a and $\ln(D_0/a^2)$ for the higher-temperature linear Arrhenius array.

the production rate of cosmogenic ^3He at this site by rescaling direct measurements of the ^3He production rate in synthetic quartz targets by Vermeesch et al. [53]. To do this, we used the scaling scheme of Stone [69] as implemented in Balco et al. [54], the elevation-atmospheric pressure relationship of Balco et al. [54], and the solar variability calculations in Vermeesch et al. [53]. This yields an estimate of 1390 atoms/g/yr for the ^3He production rate at the site where HU-08-03 was collected. It is difficult to evaluate the accuracy of this estimate because of uncertainties in production rate scaling between high elevations at low and high latitudes [103], so we assign a 10% uncertainty to this estimate based on the scaling uncertainty in ^3He production rate estimates estimated by Goehring et al. [104]. Given this production rate, the apparent exposure age of HU-08-03 from cosmogenic ^3He is 2700 ± 350 yr. The ratio of this apparent exposure age to the radiocarbon age of the moraine ($12350 \pm 200/20$ yr; [90, 91]) is 0.22 ± 0.03 , which indicates that if the radiocarbon age represents

the true exposure age of sample HU-08-03, 75% of the cosmogenic ^3He produced during this sample's exposure history has been diffusively lost.

2.4.3 Fluid and mineral inclusions

Examination of polished grain mounts provides us with a qualitative sense of the abundances and types of fluid and mineral inclusions characteristic of the quartz samples we studied in diffusion experiments. Example images from optical microscope and SEM analyses are provided in Fig. S9 of Tremblay et al. [87]. Of the three quartz samples with one linear Arrhenius array present in the step-degassing experiments, CarBZ and 03-RDY-011-QZH contain no visible fluid or mineral inclusions. Quartz fragments from sample 03-RDY-011-QZH are highly fractured, with cracks often penetrating deep into the interior of grains. UB09-4 also displays a single linear Arrhenius array, yet SEM examination revealed that quartz from UB09-4 often contains inclusions of accessory minerals like apatite, zircon, and rutile. Some quartz fragments from UB09-4 also contain linear tracks of opaque fluid inclusions visible in plain light, although these are not abundant. Of the samples exhibiting two linear Arrhenius arrays in step-degassing experiments, the abundance and type of inclusions are highly variable. Quartz fragments from samples 04-MG-080-BR and 04-RDY-139-STR are dominated by abundant trails of dark fluid inclusions. Fluid inclusions in these two samples make up a significant (although not quantified) volume of the quartz fragments. On the other hand, fluid inclusions are rare in quartz fragments from samples 98-PCM-105-MNZ, HU-08-03, and QA-767-Q, all of which exhibit two well-defined linear Arrhenius arrays in experiments. We found evidence for a fluid inclusion trail in one quartz fragment from sample HU-08-03 and occasional isolated fluid inclusions in other quartz fragments from these samples. We observed inclusions of the minerals zircon, apatite, and hornblende in quartz fragments from sample 98-PCM-105-MNZ, and numerous zircon inclusions were present in quartz from sample HU-08-03. We only found one inclusion of a feldspar in a quartz fragment of QA-767-Q.

2.4.4 Trace element concentrations

We report concentrations of Al, Ca, Fe, K, Li, Mg, Na, and Ti measured by ICP-OES for each of the quartz samples we conducted step-degassing experiments on in Table S5 of Tremblay et al. [87]. Mn concentrations were below the detection limit in all samples and are therefore not reported. For five of the eight samples with sufficient material, we dissolved two separate aliquots of quartz; these replicates are listed in Table S5 of Tremblay et al. [87]. Concentrations of all elements were below detection limit in two procedural blanks. All quartz samples contain measurable Al, with concentrations ranging from 15 to 650 ppm. Most quartz samples also contain measurable Li, Na, and Ti.

2.5 Discussion

Numerous mechanisms could be responsible for the complex Arrhenius behavior observed in six of our nine experiments. As we discuss below, our results suggest that anisotropy and temperature-dependent structural transformations are unlikely causes. Instead, a sample-specific property, such as radiation damage, structural defects, mineral inclusions and fluid inclusions may be responsible for the complex Arrhenius behavior. While at present we cannot definitively explain this behavior, we present a simple two-domain model that, although lacking an underlying physical mechanism, closely reproduces the observed complex Arrhenius behavior. We then use this two-domain model framework and our measurements of cosmogenic ^3He in sample HU-08-03 to test the applicability of our laboratory-determined diffusion kinetics at Earth surface temperatures and over geologic time.

2.5.1 Complex Arrhenius behavior

The low-temperature linear Arrhenius arrays observed in our experiments broadly agree with the single linear Arrhenius arrays observed for ^3He and ^{21}Ne diffusion in experiments reported by Shuster and Farley [22] (Fig. 2.4). This indicates that these low-temperature arrays represent volume diffusion of ^3He and ^{21}Ne in our quartz samples. Below we explore potential mechanisms for producing complex Arrhenius behavior (i.e. the occurrence of, and transition between, low- and high-temperature linear arrays) for ^3He and ^{21}Ne observed in some of our experiments.

Anisotropy is not the likely cause of the complex Arrhenius behavior for two reasons. First, we analyzed roughly equant quartz fragments in each diffusion experiment (i.e. the aspect ratios of the respective crystallographic axes were not extreme), but complex Arrhenius behavior was only observed in some of the experiments. We would expect each quartz fragment to exhibit two linear Arrhenius arrays if the arrays corresponded to diffusion along different crystallographic directions within the quartz lattice. Second, anisotropic diffusion occurs when the energy barriers associated with different diffusion pathways differ significantly enough such that one pathway is preferred at low temperatures and that multiple diffusion pathways are permitted at high enough temperatures [e.g. 94]. Thus there is a temperature dependence to which diffusion pathway is taken, and this temperature dependence should be expressed in both prograde and retrograde heating cycles. Yet in all cases where the complex ^3He behavior is observed, the diffusivities defining the second linear array correspond to both prograde and retrograde heating steps to below the transition (e.g. Fig 2.1A, 2.2A) and do not agree with the diffusivities in the preceding transition zone. Collectively, these lines of evidence are inconsistent with the hypothesis that multiple Arrhenius arrays are the result of anisotropic diffusion.

The observed temperatures of the apparent transition in D/a^2 also make structural transformations in quartz an unlikely cause of complex Arrhenius behavior. The only structural transformation expected to occur in quartz during the main phase of our experiments (i.e. not the final highest temperature steps) is the α -quartz to β -quartz transformation. The α

to β -quartz transformation occurs instantaneously at ~ 573 °C at 1 atm [105, and references therein] and likely occurs at a similar temperature in our experiments under vacuum. At temperatures preceding the α to β -quartz transformation, α -quartz experiences systematic volume expansion; after the transition, β -quartz experiences no volume expansion at temperatures below 1000 °C [106]. We thus expect a change in diffusive behavior of ^3He and ^{21}Ne across the α to β -quartz transformation. Yet the transition between the initial low-temperature linear array and the subsequent high-temperature array occurs at temperatures ≤ 450 °C for ^3He in all experiments where we observed the transition. The α -quartz to β -quartz transformation likely does affect the diffusive behavior of ^{21}Ne in our experiments, since deviation from the first linear Arrhenius array generally occurs between 400 and 600 °C. Further, the Pt-Ir packets are allowed to cool during analyses in between heating steps, which means that quartz fragments undergo the instantaneous α to β -quartz transformation multiple times towards the end of the diffusion experiments. Repeated transformation between α -quartz to β -quartz may explain why second high-temperature ^{21}Ne arrays consistent with ^3He high-temperature arrays are not always observed. This may also explain why activation energies for high-temperature ^{21}Ne arrays are inconsistent with activation energies of the low-temperature ^{21}Ne arrays, in cases where high-temperature ^{21}Ne and ^3He agreement is observed. Ultimately, these inconsistencies in ^{21}Ne behavior at or above the α to β -quartz transformation temperature indicate that only the low-temperature linear array for ^{21}Ne observed in our experiments should be extrapolated to Earth surface temperatures. In future experiments, degassing most of the ^{21}Ne through longer heating steps at temperatures lower than the α to β -quartz transformation temperature may result in a better resolved second linear Arrhenius array for ^{21}Ne .

The fact that in most experiments we observed departures from the low-temperature Arrhenius arrays at nearly equivalent cumulative release fractions of ^3He and ^{21}Ne (Fig. 2.1C, 2.2C) but different temperatures for each nuclide (Fig. 2.1B, 2.2B) is significant for several reasons. In addition to the arguments above about anisotropy and the α to β -quartz transformation, this observation indicates that the ^3He diffusivity transition is not due to a material property change. Otherwise, diffusivities of both nuclides would be expected to deviate from linear Arrhenius behavior at a common temperature. Further, the relationship between low-temperature Arrhenius arrays and cumulative release fractions suggests that the patterns of ^3He and ^{21}Ne diffusive behavior are controlled by a common mechanism at temperatures < 573 °C. Since this behavior is not observed in all experiments, and the cumulative gas fraction comprising the first linear arrays varies between experiments, this behavior must be controlled by a sample-specific property such as radiation damage, mineral inclusions, fluid inclusions, or structural defects. We discuss each of these sample-specific properties and its potential link with diffusive behavior below.

The diffusion kinetics of noble gases in quartz may be influenced by natural radiation damage, due to U and Th present either in the quartz itself or in surrounding or included accessory minerals, or by damage associated with proton irradiation. With regards to the latter, Shuster and Farley [22] calculated slightly different ^3He and ^{21}Ne diffusion parameters in experiments on two fragments of the same quartz sample irradiated with different proton en-

ergies and fluences; the fragment experiencing the higher proton dose exhibits slightly greater ^3He and ^{21}Ne retentivity. We did not irradiate individual samples with different proton doses and therefore cannot evaluate whether the proton irradiation influenced the diffusion kinetics inferred from linear Arrhenius arrays. However, the results of our stepwise degassing experiment on non-irradiated quartz fragments from sample 04-RDY-139-STR clearly demonstrate that complex Arrhenius behavior is not an artifact of the proton irradiation. For cosmogenic ^3He , we observed significantly lower apparent diffusivities at temperatures corresponding to the low temperature linear Arrhenius array in the proton-irradiated experiment, consistent with diffusive loss over this sample's exposure history at subzero temperatures in Antarctica. In contrast, we find excellent agreement between apparent diffusivities of cosmogenic and proton-induced ^3He corresponding to the high temperature linear Arrhenius array (Fig. 2.5A). This has two important implications. First, that the high-temperature array in proton-irradiated quartz is also present in the diffusive behavior of non-irradiated quartz and is thus not an artifact of the irradiation. Second, given likely mean annual temperatures at this elevation in the southern Transantarctic Mountains near -40°C , we expect significant diffusive loss of ^3He based on the low-temperature Arrhenius array, but insignificant ($< 5\%$) loss based on the high-temperature Arrhenius array. This observation may indicate that ^3He , and by inference ^{21}Ne , are hosted in two separate reservoirs in quartz characterized by the diffusion parameters calculated for each linear Arrhenius array. We explore this possibility in a two-domain model constructed below.

At relatively low doses, the accumulation of natural radiation damage is known to increase He retentivity in minerals like apatite [96, 97, 107] and zircon [98], and cathodoluminescence and electron paramagnetic resonance (EPR) analyses demonstrate that α -particles produced by U and Th decay induce structural defects in quartz, in particular silicon vacancies and peroxy linkages [108, 109]. If damage induced by natural radiation influences noble gas diffusion in quartz, as it does in apatite and zircon, we expect this damage to have similar effects on cosmogenic and proton-induced noble gas diffusion in quartz. This is because natural radiation damage, unlike damage produced during proton irradiation, will accumulate in quartz on geologic timescales, presumably starting long before quartz samples are exposed to cosmic rays at the Earth's surface. That the quartz fragments we analyzed come from geologic samples with vastly different ages, from Precambrian metamorphic rocks to Miocene volcanics, indicates that these samples likely have very different amounts of natural radiation damage. To assess this more directly, we calculated the amount of ^4He present in each sample prior to proton irradiation (Table S6 in Tremblay et al. [87]) by simply subtracting the proton-induced ^4He from the total observed ^4He by assuming a production $^4\text{He}/^3\text{He}$ ratio of ~ 8.5 and that all observed ^3He is proton-induced [e.g. 22]. Assuming that most of the inherent ^4He is radiogenic and therefore a proxy for the amount of radiation damage accumulated, we find no correlation between complex Arrhenius behavior and radiation damage, nor do we find an obvious relationship between the diffusion parameters for the first linear Arrhenius array and radiation damage. Additionally, the concentrations of ^4He in the two quartz fragments from sample QA-767-Q vary by a factor of seven, but the results of the two diffusion experiments are remarkably consistent. We realize, however, that

the concentration of ^4He in our quartz samples is a non-ideal proxy for radiation damage, since ^4He experiences diffusive loss from quartz at Earth surface temperatures and because non-radiogenic ^4He may also be present in these samples. In the future, measuring U and Th concentrations in quartz samples analyzed in diffusion experiments should provide a more robust measure of the effects of radiation damage on noble gas diffusion kinetics.

In addition to radiation-induced damage, numerous point defects, dislocations or line defects, and twinning boundaries have been commonly identified in naturally occurring quartz [e.g. 110] that may influence noble gas diffusive behavior. We observed no systematic correlation between the concentrations of any trace element commonly associated with point defects and the observation of one or two linear Arrhenius arrays in step-degassing experiments (Table S5 in Tremblay et al. [87]). Likewise, we observed no systematic correlation between trace element concentration and the fraction of ^3He and ^{21}Ne represented by the low-temperature linear Arrhenius arrays when two arrays were observed. While these observations indicate that point defects commonly associated with trace elements in quartz do not likely contribute to the observed complexity in noble gas diffusion, there are a number of point defects in quartz not associated with trace elements that we have not attempted to identify or evaluate here, including peroxy linkages, oxygen vacancies, silicon vacancies, and non-bridging oxygen holes. Additionally, we have not attempted to quantify the density of line or plane defects in our quartz samples. A series of inward diffusion experiments provide evidence for fast-path diffusion of noble gases in quartz, either by edge/screw dislocations [111, 112] or via isolated nanopores ranging in size from 10 to 15 nm [84]. When considered in the context of our step-degassing experiments, these experimental results point to the possibility that line and plane defects that do not intersect the boundaries of a quartz grain act as noble gas sinks, similar to how radiation damage in apatite creates pockets or traps where He can accumulate [96, 97]. Thus structural defects in quartz remain a strong potential candidate for explaining the complex diffusive behavior of ^3He and ^{21}Ne observed in our experiments.

Fluid and mineral inclusions in the quartz samples we analyzed are highly variable and do not correlate systematically with complex Arrhenius behavior. Many of the quartz samples displaying such complexity contain accessory minerals like zircon and apatite. When present, accessory mineral inclusions are smaller than 20 μm in diameter and do not make up a significant volume of the quartz fragments, which are generally 200 μm in diameter or larger (Fig. S9 in Tremblay et al. [87]). Because spallogenic ^3He and ^{21}Ne are produced in these accessory mineral inclusions during proton irradiation at rates similar to production rates in the quartz matrix [e.g. 88], they constitute an insignificant fraction of the total ^3He and ^{21}Ne abundances and therefore cannot account for the volume of gas associated with the higher-temperature array sometimes observed. Further, apatite, zircon, and rutile inclusions are common in quartz fragments from sample UB09-4, which only exhibited one linear Arrhenius array.

Visible fluid inclusions 5-15 μm in diameter occurred in the quartz analyzed by Trull et al. [23]. The ^3He diffusion parameters those authors calculated agree well with the ^3He diffusion parameters we calculated for the high-temperature linear Arrhenius arrays, indicating that

fluid inclusions may be responsible for complex Arrhenius behavior. We found evidence for fluid inclusions in at least one quartz fragment for all of the samples that exhibited complex Arrhenius behavior. However, the abundance of fluid inclusions varies significantly amongst these quartz samples. While fluid inclusion trails make up a significant volume of the quartz fragments in two of the samples (Fig. S9B,C in Tremblay et al. [87]), fluid inclusions are rare and isolated in other quartz samples exhibiting complex Arrhenius behavior (Fig. S9D,F,G,H in Tremblay et al. [87]). Given that fluid inclusions in our quartz samples are almost always smaller than 10 μm , it seems unlikely that sufficient abundances of ^3He and ^{21}Ne were produced in fluid inclusions to constitute the higher temperature linear Arrhenius arrays observed in the samples with rare fluid inclusions. Additionally, we observed no correlation between complex Arrhenius behavior and concentrations of Ca, K, Mg, or Na, elements that are often concentrated in fluid inclusions [e.g. 101]. An important caveat is that the composition of the fluid inclusions dictates the partition coefficient of ^3He and ^{21}Ne between the fluid inclusions and quartz, and the specific compositions of the fluid inclusions in the quartz samples we analyzed are unknown. Thus fluid inclusions remain a viable potential contributor to the complex Arrhenius behavior observed in some experiments.

2.5.2 Comparison with results from Shuster and Farley (2005)

Shuster and Farley [22] conducted step-degassing experiments on gem-quality quartz from Brazil that exhibited single linear Arrhenius arrays for both ^3He and ^{21}Ne . Shuster and Farley [22] did not measure a large fraction of the ^{21}Ne present in their irradiated quartz aliquots in the step-degassing portion of their experiments ($\sim 40\%$ for the high-dose experiment and 10% for the low-dose experiment). Additionally, there is a slight deviation from the linear Arrhenius array for ^{21}Ne at the end of their low-dose experiment similar to the transition zone described in our experiments. From these two observations one can speculate that Shuster and Farley [22] may have observed complex diffusion behavior of ^{21}Ne if they had continued measuring ^{21}Ne in the step-heating portion of their experiment. However, we do not think that this methodological difference is responsible for the differences between their results and the results presented here, for in both of their experiments Shuster and Farley [22] completely degassed helium during the step-heating portion of their experiments and did not observe any deviation from a linear array.

CarBZ, a different Brazilian gem-quality quartz sample analyzed here, likewise exhibited a single linear Arrhenius array. However, the final $\sim 40\%$ of gas released in the experiment on CarBZ deviates from the linear Arrhenius array, and the Arrhenius parameters calculated from this array suggest much greater ^3He and ^{21}Ne diffusivity for CarBZ than the sample analyzed in Shuster and Farley [22]. The differences in diffusion kinetics and behavior between these two gem-quality samples, both of which lack fluid and mineral inclusions, supports the hypothesis that these differences are caused by inter-sample variability in material properties—specifically radiation damage and/or structural defects—that are not quantitatively measured here. Unfortunately, we do not have sufficient material from the sample analyzed in Shuster and Farley [22] to test this hypothesis.

2.5.3 Two-domain model for ^3He diffusion in quartz

Although we have not identified a mechanistic explanation for the complex diffusive behavior of proton-induced ^3He and ^{21}Ne in quartz, our step-degassing experiment on the naturally irradiated aliquot of quartz sample 04-RDY-139-STR clearly demonstrates that the mechanism driving complex behavior influences cosmogenic noble gas retention over geologic time. Deviations from simple Arrhenius linearity similar to those observed in our experiments are often observed for Ar in feldspars. This led to the development of multiple diffusion domain (MDD) theory, whereby the non-linearity is explained by the systematic exhaustion of sub-grain domains with unique diffusion kinetics [e.g. 113, 114]. Lacking a mechanistic model, we took a similar approach and used the sample-specific diffusion parameters for the low and high temperature linear Arrhenius arrays to construct a simple two-domain diffusion model for noble gas diffusion in each quartz sample exhibiting two linear arrays. Like MDD models, these empirical models assume that the quartz fragments analyzed contain two, non-interacting domains that each make up a fraction of the total quartz fragment volume in which ^3He and ^{21}Ne can reside. Domain 1 refers to the lower retentivity domain characterized by the diffusion parameters of the low-temperature linear Arrhenius array from each diffusion experiment; domain 2 refers to the high retentivity domain characterized by the diffusion parameters of the higher-temperature linear Arrhenius arrays when observed. The fact that we observe divergence from the low-temperature Arrhenius array at the same cumulative gas release fraction for both He and Ne implies that the same two-domain model is appropriate for both noble gases. However, as discussed above, we are less likely to have accurately quantified the diffusion kinetics of the higher-temperature domain for Ne, so we only construct these models using the ^3He diffusion kinetics from our experiments. Because the ^{21}Ne diffusion kinetics for the low-temperature domain imply complete retention at Earth surface temperatures in most quartz samples, these models are less relevant to the interpretation of ^{21}Ne abundances in natural samples (see below).

In the two-domain model, the proportion of ^3He in each domain is allowed to vary, and diffusivities are calculated for the same heating schedule as used in the proton-irradiated experiment using the equations outlined by Fechtig and Kalbitzer [82]. We determined the proportion of ^3He in each domain that best agreed with the experimental data by calculating a misfit statistic M :

$$M = \frac{1}{n} \sum_{j=1}^n \left(\frac{f_{p,j} - f_{m,j}}{\bar{\sigma}} \right)^2 \quad (2.1)$$

where $f_{p,j}$ is the modeled cumulative release fraction of ^3He at heating step j , $f_{m,j}$ is the cumulative release fraction of ^3He during heating step j in the experiment, $\bar{\sigma}$ is the mean uncertainty in the cumulative release fractions of ^3He determined from the Monte Carlo simulation, and n is the number of steps in each heating schedule. Modeled diffusivities for ^3He using the domain proportions that minimized this misfit statistic are shown in Arrhenius space for samples HU-08-03 and QA-767-Q(1) in Fig. 2.6 and in Fig. S10 in Tremblay et al. [87] for the other four experiments exhibiting complex Arrhenius behavior. The two-domain

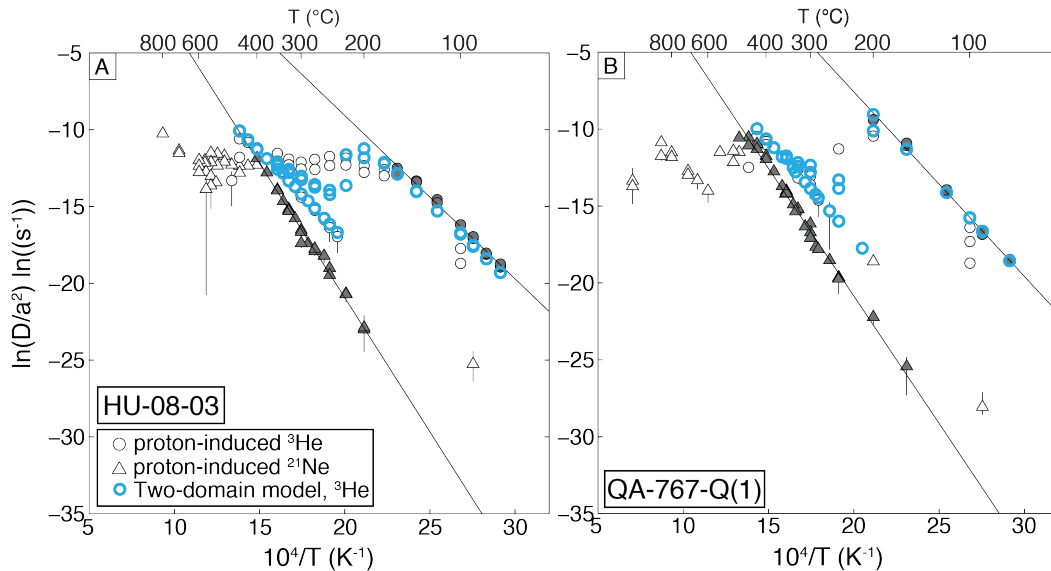


Figure 2.6: Arrhenius plots of the two-domain models for ${}^3\text{He}$ diffusion in quartz samples HU-08-03 (A) and QA-767-Q(1) (B). The results of the diffusion experiment on proton-irradiated quartz fragments corresponding to Figs. 3.1A and 3.2A are shown for comparison with the two-domain model (blue circles). The proportion of gas apportioned to the two domains minimized the misfit statistic M discussed in Eq. (2.1). For HU-08-03 (A), the two-domain model predicts that 81% of the ${}^3\text{He}$ is resides in domain 1, with the remaining 19% populates domain 2. For QA-767-Q(1) (B), only 1% of the ${}^3\text{He}$ is expected to be hosted in domain 2.

models reproduce the two linear Arrhenius arrays observed in experiments as expected, but generally differ from the steps in the experiment corresponding to the transition zone. The amount of gas apportioned to domain 1 ranges from 75% to 99% (Table S7 in Tremblay et al. [87]), which in each of the diffusion experiments corresponds well with the low-temperature linear Arrhenius array and a portion of the transition zone. For the remaining discussion we continue to use the two-domain model framework, recognizing that a model with stronger mechanistic underpinnings is important for future work.

2.5.4 Implications for He and Ne retentivity in quartz

The nine diffusion experiments we conducted on a variety of quartz samples demonstrate that both the diffusion kinetics and diffusive behavior of ${}^3\text{He}$ and ${}^{21}\text{Ne}$ in quartz are quite variable. This implies that retentivity of cosmogenic ${}^3\text{He}$ and ${}^{21}\text{Ne}$ at Earth surface temperatures can vary significantly as well. Fig. 2.7 shows expected variation in cosmogenic ${}^3\text{He}$ and ${}^{21}\text{Ne}$ retentivity during an example continuous exposure history given the ${}^3\text{He}$ and ${}^{21}\text{Ne}$ diffusion parameters calculated from each diffusion experiment. To highlight the effect of

apparent MDD-like behavior of ^3He observed in some experiments on cosmogenic ^3He retention during surface exposure, we show separate retentivity curves for He diffusion parameters inferred from the two separate linear Arrhenius arrays (Fig. 2.7A). He diffusion parameters calculated for the low-temperature linear Arrhenius arrays imply that all quartz samples analyzed will experience significant diffusive loss of cosmogenic ^3He even at subzero surface exposure temperatures, which is consistent with the conclusions of Shuster and Farley [22]. However, the diffusion parameters of the high-temperature linear Arrhenius arrays indicate nearly complete retention of ^3He in the postulated high-retentivity domain at temperatures near or well above 0 °C in large quartz grains. This contrast is important for potential applications of cosmogenic ^3He in quartz to exposure-dating and paleothermometry [68], as a two-domain model predicts partial retention of cosmogenic ^3He over a wider range of temperatures and exposure times than either domain by itself.

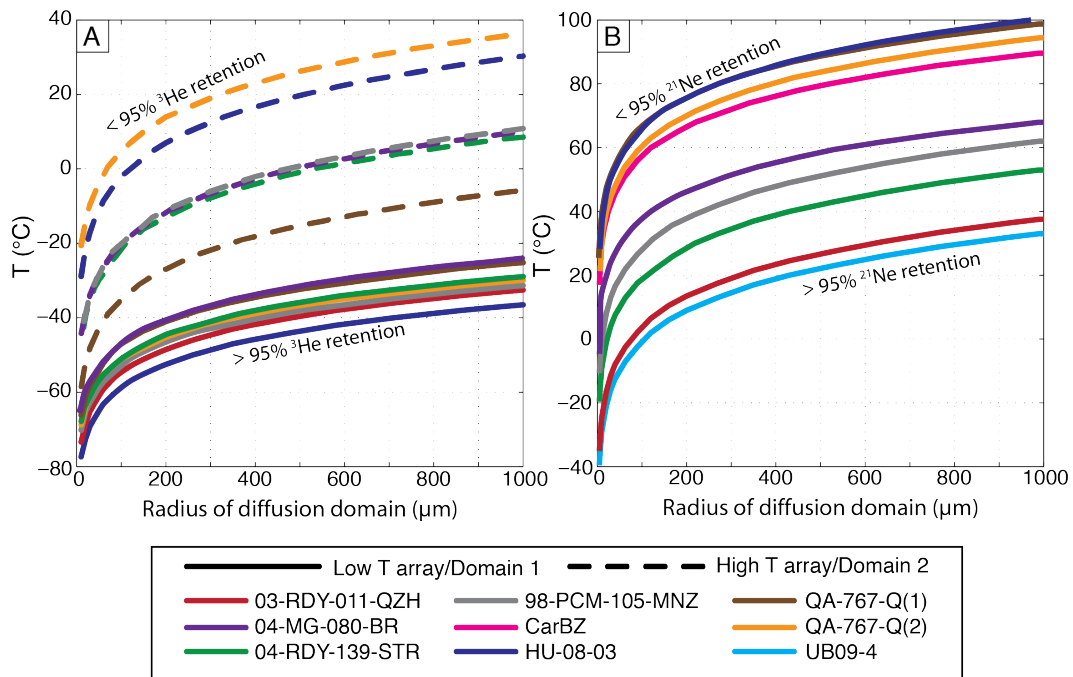


Figure 2.7: Helium (A) and neon (B) retentivity in quartz. The curves show threshold temperatures above which $< 95\%$ retention would occur in quartz as a function of diffusive lengthscale for isothermal simultaneous production and diffusion over 50,000 years, calculated after Wolf et al. [37]. For ^3He (A), the threshold temperature-diffusive lengthscale relationship is shown for the diffusion kinetics calculated for both the low temperature (solid) and high temperature (dashed) linear Arrhenius arrays when observed in diffusion experiments. Retentivity curves for ^3He in quartz samples UB09-4 and CarBZ plot below the temperature range shown. For ^{21}Ne (B), retentivity curves are only shown for the first linear Arrhenius array observed in diffusion experiments.

The variability we observed in ^{21}Ne diffusion kinetics among samples is less important from the perspective of cosmogenic ^{21}Ne retention at Earth surface temperatures, because in nearly all cases the experimental results predict that $> 95\%$ of cosmogenic ^{21}Ne produced in quartz will be retained at temperatures $< 40\text{ }^\circ\text{C}$ for diffusion domain radii $> 500\text{ }\mu\text{m}$ (Fig. 2.7B). ^{21}Ne retentivities are shown using only the diffusion parameters of the low-temperature linear Arrhenius arrays; diffusion parameters for the high-temperature array in three experiments imply even greater retention. Given that temperatures consistently exceeding $40\text{ }^\circ\text{C}$ occur in very few places on Earth, our experiments indicate that cosmogenic ^{21}Ne will generally be quantitatively retained in quartz over geologic time. This is consistent with the results of Shuster and Farley [22] and numerous measurements of cosmogenic ^{21}Ne exposure ages in quartz that agree with exposure ages determined using other cosmogenic radionuclides [e.g. 30, 70, 115]. In the most qualitative sense, this interpretation is also consistent with the Ne diffusion kinetics estimated from the inward diffusion experiments conducted by Cherniak et al. [20]; however, they calculated diffusion parameters that predict Ne diffusivities six orders of magnitude lower than the most retentive quartz sample we analyzed. As mentioned previously, the very small length scales over which inward diffusion experiments like those of Cherniak et al. [20] are conducted avoid the physical heterogeneities in quartz that—as our experiments demonstrate—can significantly influence the net, grain-scale diffusion of noble gases from natural quartz that we are ultimately interested in quantifying.

Importantly and in contrast to the experiments of Cherniak et al. [20], some of the experiments we conducted imply that quantitative retention of cosmogenic ^{21}Ne does not always occur at moderately high surface temperatures. For example, the experiments on quartz samples 03-RDY-011-QZH and UB09-4 predict that, at temperatures of $20\text{--}40\text{ }^\circ\text{C}$, detectable diffusive loss of cosmogenic ^{21}Ne will occur over short exposure times and significant diffusive loss will occur after $10^6\text{--}10^7$ yr of exposure. The activation energy estimated by Niedermann et al. [86] for ^{21}Ne diffusion in quartz of $90 \pm 10\text{ kJ/mol}$ agrees with those calculated from the experiments on 03-RDY-011-QZH and UB09-4 within uncertainty and predicts similar diffusive behavior at relatively high surface temperatures. This variability in ^{21}Ne diffusion kinetics is potentially important in interpreting old apparent exposure ages inferred from cosmogenic ^{21}Ne concentrations in quartz in hot environments [e.g. 65].

The variability in ^3He and ^{21}Ne retentivity inferred from our diffusion experiments and from previous estimates of ^3He and ^{21}Ne diffusivities in quartz from step-degassing measurements [22, 23, 86] indicates that sample-specific diffusion parameters are required to quantitatively apply the open-system behavior of these nuclides to geologic problems. Our results predict that quartz grains in rocks sharing a common exposure duration and temperature but characterized by different diffusion kinetics can contain significantly different abundances of cosmogenic noble gases. Thus if we measure the abundances of cosmogenic noble gases in quartz from a geologic sample, we may come to drastically different inferences about the exposure duration and/or mean exposure temperature of that sample depending on the set of diffusion kinetics we assume. We illustrate this point below with measurements of cosmogenic ^3He in sample HU-08-03.

2.5.5 Geologic applicability of laboratory-determined diffusion kinetics

To test whether our laboratory-determined diffusion kinetics for ^3He accurately quantify cosmogenic ^3He diffusion under natural conditions, we compare the measured concentration of cosmogenic ^3He in quartz sample HU-08-03, a rhyolitic moraine boulder adjacent to the Quelccaya ice cap in Peru, with the concentration predicted from our step-degassing experiments. As previously mentioned, the exposure age of this sample is independently known from radiocarbon dating of the moraine, as well as cosmogenic ^{10}Be analysis of the same boulder and adjacent boulders, to be $12350 \pm 200 / -20$ yr [90, 91]. In Fig. 2.8A, we predict cosmogenic ^3He retention as a function of exposure time and isothermal holding temperatures using the laboratory-determined diffusion parameters for HU-08-03, the average grain size of the quartz analyzed for cosmogenic ^3He ($a = 300 \mu\text{m}$), and two models. In one model, we only use He diffusion kinetics represented by the low-temperature linear Arrhenius array. In the other model, we assume ^3He occupies two domains and use the diffusion kinetics and relative domain proportions from fitting a two-domain model to the experimental data (Fig. 2.6A). For the one-domain model, the measured cosmogenic ^3He retention is consistent with a holding temperature of -5°C , whereas the two-domain model implies a holding temperature in the range $1\text{--}5^\circ\text{C}$.

In order to quantify daily and annual fluctuations in local temperature and calculate an effective exposure temperature for the sample, we obtained hourly and monthly air temperature measurements from a USCRN-compatible weather station at Quelccaya ice cap for the period 2007–2013 from Doug Hardy of the University of Massachusetts Amherst and corrected temperatures for the elevation difference between the weather station and moraine using a local lapse rate determined from NCEP reanalysis data [116]. This calculation accounts for the fact that diffusivity is an exponential function of temperature and that therefore the effective temperature—corresponding to the mean diffusivity experienced by the quartz sample over these short-term temperature oscillations—is higher than the mean temperature. Because of the daily and annual temperature amplitudes at this low-latitude site, the effective exposure temperature we calculated of 1°C is very close to the mean annual temperature (MAT) of $\sim 0.1^\circ\text{C}$. This also means that the effective temperature calculated using the diffusion parameters for the low and high-temperature linear Arrhenius arrays observed in the diffusion experiment on HU-08-03 are indistinguishable. Fig. 2.8A shows that if we assume an effective exposure temperature of 1°C applies for the entire exposure history of this sample, we find that the one domain approach predicts significantly lower ^3He retention than observed. The two-domain model, on the other hand, predicts ^3He retention indistinguishable from the observed retention. We suggest that the effective exposure temperature used in this calculation is a minimum estimate, since we have not accounted for the effect of radiative heating of the sample surface on daily temperature amplitudes, nor have we accounted for evidence that temperatures at Quelccaya ice cap were warmer during the mid-Holocene [117]. Nonetheless, this result provides two important insights about the geologic applicability of our diffusion experiments and two-domain models. First,

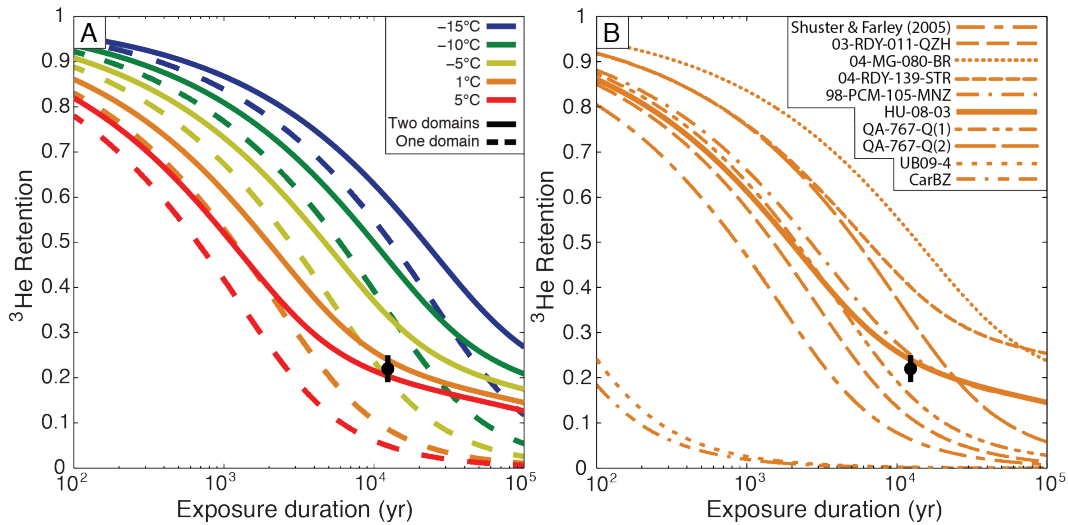


Figure 2.8: Retention of cosmogenic ^3He in sample HU-08-03, calculated from ^3He measurements on seven quartz aliquots. The known radiocarbon age for the moraine on which this sample was collected is $12350 +200/-20$ yr [90, 91]. In (A), the observed cosmogenic ^3He retention is compared to the predicted evolution of ^3He retention using the laboratory-determined diffusion parameters for HU-08-03 for different isothermal holding temperatures, calculated after Wolf et al. [37]. ^3He retention evolution curves are calculated using the diffusion parameters for only the low-temperature linear Arrhenius array (dotted) and the diffusion parameters for both linear Arrhenius arrays using the two-domain model (solid). In (B), the observed cosmogenic ^3He retention is compared to the predicted evolution of ^3He retention using the laboratory-determined diffusion parameters from all experiments for an isothermal holding temperature of 1°C , the effective exposure temperature at the moraine today. For experiments in which complex Arrhenius behavior was observed, the two-domain model is shown. The ^3He retention curve for the diffusion parameters reported by Shuster and Farley [22] is also shown.

it demonstrates that solely considering the diffusion parameters for the low-temperature linear Arrhenius arrays in our experiments does not adequately quantify the diffusive behavior of cosmogenic ^3He at the grain scale. Second, it indicates that although not framed by a physical mechanism, the two-domain model based on laboratory diffusion kinetics accurately simulates the diffusive loss of cosmogenic ^3He in a geologic setting.

In Fig. 2.8B, we use the same approach for modeling retention to highlight the importance of sample-specific diffusion kinetics for quantitative prediction of cosmogenic ^3He retention in geologic settings. We calculate ^3He retention using diffusion parameters from each of our nine diffusion experiments as well as that of Shuster and Farley [22]. As with the comparison in Fig. 2.8A, the effective exposure temperature is not sensitive to the diffusion parameters used in its calculation at this location; therefore we model ^3He retention for an effective exposure

temperature of 1 °C using each set of diffusion parameters. In experiments where we observed complex Arrhenius behavior, we used the two-domain model fit to the experimental results. For the known exposure age of ~ 12.4 ka, we find that most calculated retention curves, including that implied by Shuster and Farley [22], disagree with measured cosmogenic ^3He retention. This result, in combination with the results shown in Fig. 2.8A, demonstrates the importance of obtaining sample-specific diffusion kinetics for geologic applications. Further, this result confirms that simply applying the ^3He diffusion parameters reported by Shuster and Farley [22] to quartz is in this case inappropriate.

2.6 Conclusions

A series of nine diffusion experiments on proton-induced ^3He and ^{21}Ne in quartz reveal that ^3He and ^{21}Ne exhibit variable and complex diffusive behavior in different natural quartz samples. We hypothesize that sample-specific features such as radiation damage, defects, or inclusions control the diffusive behavior we observed, although we were not able to identify a clear correlation between diffusion kinetics and any easily observable physical property of the samples. Measurements of cosmogenic ^3He and ^{21}Ne in some of the same samples demonstrate that complex diffusive behavior observed for proton-induced ^3He and ^{21}Ne is not an artifact of producing these nuclides via proton irradiation and needs to be accounted for in geologic applications. Identifying what controls complex and variable diffusive behavior of noble gases in quartz and developing mechanism-based diffusion models is thus an important direction for future research. To a first order, the ^3He and ^{21}Ne diffusion kinetics we observed in quartz are consistent with previous experiments and empirical observations suggesting that cosmogenic ^3He will experience significant diffusive loss from quartz on timescales $> 10^3$ yr even at subzero temperatures, while cosmogenic ^{21}Ne will be quantitatively retained at nearly all Earth surface temperatures for $> 10^6$ years. Importantly, the results presented here facilitate quantitative applications of these phenomena in determining both paleotemperatures and exposure durations from cosmogenic ^3He and ^{21}Ne concentrations.

2.7 Acknowledgements

We thank B Goehring and J. Schafer for providing information about and material from sample UB09-4, D. Rood for providing material from sample QA-767-Q, J. Stone for providing material and exposure-age data from samples 04-RDY-139-STR and 98-PCM-105-MNZ, and R. Wenk for providing sample CarBZ. We thank P. Brooks, N. Fylstra, and T. Teague for analytical assistance, and D. Hardy for sharing data from the Quelccaya ice cap weather station. We acknowledge support from the NSF Petrology and Geochemistry Program (EAR-1322086), the UC Berkeley Larsen Grant, and the Ann and Gordon Getty Foundation.

Chapter 3

Neon diffusion kinetics and implications for cosmogenic neon paleothermometry in feldspars

This chapter was previously published in Tremblay, M.M., Shuster, D.L., Balco, G., and Cassata, W.S., *Geochimica et Cosmochimica Acta* **205**, 14–30 (2017). doi:10.1016/j.gca.2017.02.013

3.1 Abstract

Observations of cosmogenic neon concentrations in feldspars can potentially be used to constrain the surface exposure duration or surface temperature history of geologic samples. The applicability of cosmogenic neon to either application depends on the temperature-dependent diffusivity of neon isotopes. In this work, we investigate the kinetics of neon diffusion in feldspars of different compositions and geologic origins through stepwise degassing experiments on single, proton-irradiated crystals. To understand the potential causes of complex diffusion behavior that is sometimes manifest as nonlinearity in Arrhenius plots, we compare our results to argon stepwise degassing experiments previously conducted on the same feldspars. Many of the feldspars we studied exhibit linear Arrhenius behavior for neon whereas argon degassing from the same feldspars did not. This suggests that nonlinear behavior in argon experiments is an artifact of structural changes during laboratory heating. However, other feldspars that we examined exhibit nonlinear Arrhenius behavior for neon diffusion at temperatures far below any known structural changes, which suggests that some preexisting material property is responsible for the complex behavior. In general, neon diffusion kinetics vary widely across the different feldspars studied, with estimated activation energies (E_a) ranging from 83.3 to 110.7 kJ/mol and apparent pre-exponential factors (D_0) spanning three orders of magnitude from 2.4×10^{-3} to $8.9 \times 10^{-1} cm^2s^{-1}$. As a consequence of this variability, the ability to reconstruct temperatures or exposure durations

from cosmogenic neon abundances will depend on both the specific feldspar and the surface temperature conditions at the geologic site of interest.

3.2 Introduction

In noble gas thermochronometry, the thermal histories of geologic materials are inferred from the concurrent production and thermally-activated diffusion of noble gases. These thermal histories can be used to understand geologic processes occurring over a vast range of temperatures and timescales, from erosion-driven exhumation of rocks over millions of years [e.g. 118, and references therein] to near instantaneous high-temperature impact events [e.g. 119–121]. Feldspar minerals are frequently utilized for noble gas thermochronometry because they are abundant in silicic rocks and have compositions that permit high noble gas production rates from both radioactive decay (radiogenic noble gases) and in situ nuclear interactions with secondary cosmic-ray particles (cosmogenic noble gases). Since its development nearly half a century ago, feldspar $^{40}\text{Ar}/^{39}\text{Ar}$ thermochronometry, which utilizes the production and diffusion of radiogenic ^{40}Ar , has been extensively used to study crustal and surface processes both on Earth [e.g. 122, 123] and other planetary bodies [e.g. 33, 124]. More recently, cosmogenic argon in feldspars has been used to reconstruct planetary surface temperatures [e.g. 125]. Cosmogenic neon in feldspars can, in theory, also be used for surface temperature thermochronometry [68, 126]. If neon is quantitatively retained in feldspars at planetary surface temperatures, cosmogenic neon measurements can also be used to determine surface exposure durations [e.g. 29].

The production and diffusion systematics of a particular noble gas–mineral pair must be known for thermochronometric or geochronologic applications. Here, we focus on empirical quantification of neon diffusion kinetics in feldspars, with the goal of examining whether cosmogenic neon can be used for surface paleothermometry [68]. The only existing constraints on neon diffusion in feldspars were reported by Gourbet et al. [21], who examined the diffusion kinetics of neutron-induced ^{22}Ne in three alkali feldspars through stepwise degassing experiments. Orthoclase and Ca-rich anorthoclase exhibited relatively simple neon diffusion behavior expressed as a linear relationship between the logarithm of diffusivity and inverse temperature (although the linearity of the orthoclase experiment has been questioned [127]), while Fish Canyon Tuff sanidine did not. The range in Arrhenius diffusion parameters (activation energy, E_a , and pre-exponential factor, D_0) calculated by Gourbet et al. [21] suggest that neon can be quantitatively retained at Earth surface temperatures over millions of years, in the case of the orthoclase studied, or diffusively lost on thousand year timescales, in the case of anorthoclase and sanidine.

Several questions remain from these initial experiments reported by Gourbet et al. [21] that we aim to address. First, what is the kinetics of neon diffusion in plagioclase feldspars? Gourbet et al. [21] studied three alkali feldspars; no experimental work has quantified the kinetics of neon diffusion in plagioclases. To fill this gap, we present results from stepwise degassing experiments on three plagioclase feldspars. We also discuss results from a stepwise

degassing experiment on an endmember plagioclase feldspar from lunar sample 76535 [126].

Second, how do the kinetics and behaviors of neon and argon diffusion compare? In contrast to neon, there is a vast literature exploring the kinetics of argon diffusion in feldspars. Some of the earliest studies examining argon in geologic materials [e.g. 128–131] found evidence for complex diffusion behavior in feldspars, which has been observed numerous times since [e.g. 95, 114, 132, 133, and references therein]. The origin and significance of complex argon diffusion behavior, which is observed as both nonlinear Arrhenius arrays and age spectra with multiple plateaus, has been discussed at length. Multiple diffusion domain (MDD) theory [113, 134, 135] posits that complex diffusion behavior results from argon diffusing from multiple, non-interacting subgrain domains of different sizes that are stable both during the geologic history and laboratory heating of a feldspar. Others have suggested that complex argon diffusion behavior may also arise due to structural modifications, microtextural development, fluid alteration, or some combination therein [e.g. 95, 136–140]. In these cases, the timing of various mineralogical changes with respect to the thermal history of a feldspar matter greatly to the interpretation of complex argon diffusion behavior.

For planetary surface paleothermometry using cosmogenic neon, any subgrain alteration during the geologic history of a feldspar will have occurred at higher temperatures than those of interest, but will likely still affect the kinetics of neon diffusion at low temperature. It is thus important to distinguish complex neon behavior due to any existing crystallochemical heterogeneities from that resulting from potential structural changes during laboratory heating. In previous work on noble gas diffusion in quartz [87], we made this distinction by examining diffusion of both helium and neon in the same aliquots. If structural alteration during laboratory heating changes diffusion kinetics, we would expect deviations from a linear Arrhenius array to occur at a common temperature for both noble gases. On the other hand, if some stable subgrain property is responsible for complex diffusion behavior, then we anticipate the temperature at which deviation from Arrhenius linearity occurs to differ for different noble gases.

In a similar manner, in this work we present neon stepwise degassing experiments on a subset of the feldspars for which Cassata and Renne [95] conducted argon stepwise degassing experiments. Cassata and Renne [95] argued that a combination of temperature-dependent structural transitions and the presence of multiple diffusion domains caused deviations from linear Arrhenius behavior in their experiments. Here, we designed our experiments such that the majority of the neon present was released at temperatures lower than those used by Cassata and Renne [95] to characterize argon diffusion. As a result, all deviations from linear Arrhenius behavior interpreted by Cassata and Renne [95] to be a result of structural transitions should be absent from our neon experiments, if their interpretation is correct. We also examined feldspars that exhibit linear Arrhenius behavior for argon diffusion to determine whether simple diffusion behavior is also observed for neon. If simple diffusion behavior is observed for both noble gases in a particular feldspar, it suggests that there is a single diffusion domain with a single diffusion lengthscale, which may equal the physical grain size of the aliquots analyzed. In these cases, our experimental results and those of Cassata and Renne [95] can be compared with theoretical calculations of argon and neon

diffusivities.

In addition to addressing the questions outlined above, we use our experimentally-determined diffusion kinetics to model the sensitivity of cosmogenic neon diffusion to temperature and exposure duration amongst different feldspars. We use the modeled sensitivities to evaluate the potential for using cosmogenic neon in feldspar to constrain past planetary surface temperatures.

3.3 Methods

We conducted neon stepwise degassing experiments on a suite of feldspar that span the full range of feldspar compositions from orthoclase to anorthite. Brief sample descriptions including compositions are provided in Table 3.1; for more detailed information, see Cassata and Renne [95] and references therein. Samples were irradiated with a 220 MeV proton beam for 5 hours at the Francis H. Burr Proton Therapy Center at the Massachusetts General Hospital. Numerous grains from a given sample were packed together into an Sn foil in order to balance ejection of proton-induced Ne with implantation [e.g. 88]. These Sn foils were packaged into HDPE capsules (9.4 mm in diameter, 3.0 in mm height), which were stacked into quartz tubes to form a ~ 500 mm long cylindrical target; the approximate range of 220 MeV protons in HDPE is 300 mm. A 100 μm thick Pb foil in front of the target stack, in conjunction with the target stack itself, defocuses and scatters the proton beam intensity in attempt to evenly distribute the cross-section flux [88, 141]. The target was flipped halfway through the irradiation to ensure Ne production in both ends of the target stack despite proton energy dissipation; the feldspars examined here were located within 150 mm of either end of the target stack. Sample temperatures do not exceed 45 $^{\circ}\text{C}$ during irradiation [22]. Proton irradiation of the feldspars examined here took place in April 2013 with a total proton fluence of $\sim 8.5 \times 10^{15} \text{ p/cm}^2$, which was measured during irradiation by a thin foil transmission ionization chamber in front of the beam aperture.

Table 3.1: Description of feldspar samples studied in diffusion experiments.

Sample	Description	Phase	Composition		
			An	Ab	Or
BMk	Granitic pegmatite, Benson Mines, NY USA	Orthoclase	0	3	97
FCs	Rhyolitic ignimbrite, Fish Canyon Tuff, CO USA	Sanidine	1	27	72
GSs	Rhyolitic ash, Gulf of Salerno, Italy	Sanidine	3.7	31	66
SURTp	Basaltic lava, Surtsey, Iceland	Labradorite	60	40	0.8
OREGp	Basaltic lava, Plush, OR USA	Labradorite	64	35	0.7
GV-09	Anorthosite, Grass Valley, CA USA	Anorthite	94	5.2	0.6
76535	Troctolite, Moon	Anorthite	96	3.5	0.3

This irradiation design should lead to spatially uniform Ne production for crystal fragments $< 500 \mu\text{m}$ in radius [141] if the crystal fragments are compositionally uniform. With the exception of Fish Canyon sanidine and Grass Valley anorthite, the feldspars studied here are compositionally homogeneous with respect to these elements [95] and we therefore expect proton-induced Ne to be spatially uniform. The production of uniform, high concentrations of neon isotopes from proton irradiation allows us to conduct stepwise degassing experiments on single feldspar crystals [22, 87, 88]. Implications for compositional zonation of Fish Canyon sanidine and Grass Valley anorthite are detailed in the discussion.

The effects of lattice damage from proton irradiation on noble gas diffusion in feldspars has not been explicitly investigated. Previous work empirically demonstrates that lattice damage generated during proton irradiation with the magnitude of fluence and energy used here does not significantly modify noble gas diffusion kinetics in other mineral phases [22, 87, 88]. Although neutron irradiation, which typically has 2–3 orders of magnitude higher fluence than proton irradiation, has been shown to influence noble gas diffusion in apatite [107], several studies have demonstrated that damage generated during neutron irradiation minimally affects argon diffusion kinetics in feldspars [95, 142, 143]. Given this set of observations, we therefore assume that damage produced during proton irradiation does not significantly modify neon diffusion kinetics in feldspars, although this assumption should be tested with replicate experiments on aliquots irradiated with different proton fluences and energies.

Proton irradiated feldspars were inspected by binocular microscopy to select individual crystals lacking penetrative fractures and visible inclusions. Selected crystals were photographed to estimate crystal dimensions (Fig. S1 in Tremblay et al. [144]) and then placed under vacuum inside Pt-Ir alloy packets affixed to K-type thermocouples. Packets were heated with either a 30 or 150 W diode laser in a feedback control loop with the thermocouple via a PID temperature controller, enabling us to maintain a setpoint temperature to within 2°C . Samples were heated in fifty or more consecutive heating steps to temperatures between 100 and 1200°C . Each heating schedule contained at least two retrograde heating cycles, and individual heating steps lasted between 0.5 and 4 hours. All measurements were made on an MAP 215-50 sector field mass spectrometer in the Noble Gas Thermochronometry Lab of the Berkeley Geochronology Center; gas purification and mass spectrometric measurement techniques are detailed in Tremblay et al. [87]. For ^{21}Ne , we made no isobaric interference corrections; the MAP 215-50 cannot resolve $^{20}\text{Ne}^1\text{H}$ from ^{21}Ne , and we assume corrections due to this isobaric interference are negligible. ^{21}Ne background corrections were made by subtracting the average of six or more room temperature procedural blanks measured over the course of each experiment from measurement time-zero intercepts; the average correction for ^{21}Ne across all experiments was 0.06×10^6 atoms. ^{20}Ne and ^{22}Ne have isobaric interferences from $^{40}\text{Ar}^{++}$ and $^{44}\text{CO}_2^{++}$, respectively, which the MAP 215-50 sector field mass spectrometer used for these experiments also cannot resolve. Although these interferences can be corrected for by introducing an ^{39}Ar spike during neon measurements and observing a linear relationship between the $\text{Ar}^{++}/\text{Ar}^+$ and $\text{CO}_2^{++}/\text{CO}_2^+$ ratios [78] (Balco and Shuster, 2009), we did not use the spike procedure during these experiments. Instead,

we assumed that all of the ^{22}Ne signal observed during room-temperature procedural blanks was entirely from $^{44}\text{CO}_2^{++}$ and used the average blank 44/22 ratio and measured $^{44}\text{CO}_2^+$ signals to correct measured ^{22}Ne signals during heating steps. ^{20}Ne was not measured. Experiments were terminated when three or more consecutive heating steps yielded ^{21}Ne and ^{22}Ne time-zero intercepts at or below background level. We determined total neon amounts by comparison with the time-zero intercepts of a manometrically-calibrated air standard. Measurement of different calibrated pipette volumes of the air standard demonstrated that ^{21}Ne sensitivity was constant over the pressure range of the analyses in a given experiment. Blank corrected ^{21}Ne and ^{22}Ne abundances for each heating step are reported in Table S1 of Tremblay et al. [144]. The magnitude of the isobaric interference correction on ^{22}Ne signals for individual heating steps varies between 5 and 100%, with an average correction of 50%. These generally large-magnitude corrections propagate into very large ^{22}Ne uncertainties; therefore we do not use the ^{22}Ne data further. The concentrations of ^{21}Ne and ^{22}Ne present in the individual feldspar crystals analyzed ($> 10^{12}$ atoms/g) are orders of magnitude greater than any likely combination of atmospheric, cosmogenic, and nucleogenic neon components present prior to proton irradiation, which for terrestrial samples are typically on the order of 10^6 – 10^8 atoms/g [e.g. 21, 29]. We therefore assume that contributions from these components are negligible in comparison to the uniformly distributed, proton-induced neon, and that variations in the $^{21}\text{Ne}/^{22}\text{Ne}$ ratio between different heating steps reflect the very uncertain isobaric interference correction made for ^{22}Ne .

We used the equations of Fechtig and Kalbitzer [82] to calculate lengthscale-normalized diffusivities (D/a^2) from the fraction of ^{21}Ne measured and duration of each heating step for each stepwise degassing experiment. By using these equations, we make several assumptions. First, we assume that Ne diffusion is both Fickian and isotropic [83]. Ar stepwise degassing experiments on cleavage flakes with different lattice orientations indicate isotropic diffusion in feldspars at the temperatures over which we conduct neon step degassing experiments [95]. Second, we assume that the initial distribution of the diffusant is spatially uniform; proton irradiation should generate Ne uniformly, as discussed above. Third, we assume that each feldspar crystal has a spherical, fixed geometry. We approximate the spherically equivalent radius of the samples used in our experiments as the radius of a sphere whose surface area to volume ratio equals that of the crystal analyzed. Previous work demonstrates that this assumption is valid for materials with moderate aspect ratios, even for crystals with realistic shapes or irregular geometries [39, 145, 146].

We first estimated the surface to volume ratio of the crystals from optical microscopy measurements. Since feldspars do not have distinctive crystal habits and frequently bear surface irregularities such as cleavage steps, we had to make simplifying assumptions about the crystal geometries to make these estimates. To overcome this limitation, we obtained accurate surface area to volume ratio and size determinations of the feldspar crystals by X-ray computed tomography. X-ray computed tomography (CT) allows for three-dimensional, nondestructive characterization of geologic samples based on the variable attenuation of X-rays as they travel through different materials [147]. After the stepwise degassing experiments, we extracted each crystal from its packet to look for evidence of fracturing. Intact

fragments were mounted on double sided tape and scanned with 3.15 μm resolution on the Xradia MicroXCT scanner at the University of Texas at Austin High-Resolution X-ray CT Facility. Using the software Blob3D [148], feldspar crystals were segmented from mounting material using a grayscale threshold and separated into individual crystal volumes. We extracted numerous statistics about these volumes, including surface area, volume, aspect ratio, and maximum and minimum axis lengths, and calculated spherically equivalent radii of the crystals for comparison with our first estimates (Table S2 in Tremblay et al. [144]).

3.4 Results

Results of the neon stepwise degassing experiments are reported in Table S1 of Tremblay et al. [144] and plotted in Figs. 3.1A–3.6A, where the natural logarithm of calculated diffusivities ($\ln(D/a^2)$, where D is diffusivity and a is the diffusive lengthscale) is shown as a function of inverse temperature. Figs. 3.1A–3.6A also show the results from argon stepwise degassing experiments on different grains of the same feldspars reported by Cassata and Renne [95]. Additionally, in Fig. 3.7 we compare the result of a neon stepwise degassing experiment on a neutron-irradiated crystal of anorthite from lunar troctolite 76535 [126] to an ^{37}Ar stepwise degassing experiment on 76535 anorthite reported by Cassata and Renne [95]. For both neon and argon datasets, we use the Monte Carlo approach described by Tremblay et al. [87] to propagate uncertainties in gas release fraction into calculated diffusivities. If the temperature dependence of noble gas diffusion is Arrhenian and the feldspar analyzed is characterized by a single diffusion domain, then we expect to observe a linear correlation in this plotting space. In many cases we observe significant deviations from linearity; however, for all stepwise degassing experiments at least a subset of the data collected comprises a linear array. We fit least squares regressions to these subsets in Figs. 3.1A–3.7A, with the goal of including as many temperature steps as possible in the regression while minimizing the residuals between the regression and the data. We used these regressions and the Monte-Carlo derived uncertainties in D/a^2 to estimate the activation energy (E_a) and diffusion coefficient (D_0/a^2) from the slope and intercept of the linear regression, respectively, assuming an Arrhenius dependence of diffusivity on temperature:

$$\frac{D}{a^2} = \frac{D_0}{a^2} \exp\left(\frac{-E_a}{RT}\right) \quad (3.1)$$

where R is the gas constant and T is absolute temperature. These calculated diffusion parameters are reported in Table 3.2. While the significance of these calculated diffusion parameters is in some cases uncertain, as will be discussed below, fitting these regressions allows us to compare the temperatures and gas fractions over which linear Arrhenius behavior is observed. These comparisons are shown in Figs. 3.1B–3.7B and 3.1C–3.7C as residuals, which we define as the difference between the calculated diffusivity from a given heating step and the expected diffusivity from the linear regression at the same temperature.

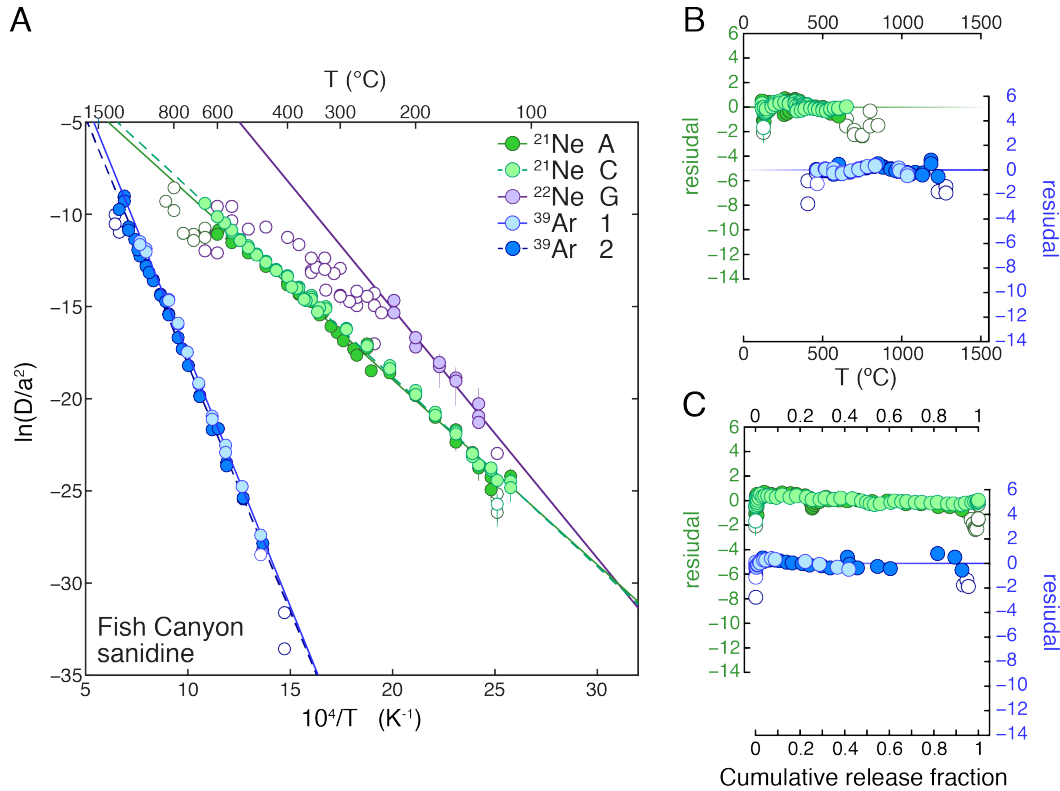


Figure 3.1: Arrhenius plot (A) and residual plots (B-C) for diffusion of proton-induced ²¹Ne (green), neutron-induced ³⁹Ar (blue; data from [95]), and neutron-induced ²²Ne (purple; data from [21]) in different crystals of Fish Canyon sanidine. For visual clarity, residuals are not shown for neutron-induced ²²Ne. D/a^2 values are normalized to s^{-1} . Uncertainties in $\ln(D/a^2)$ estimated using a Monte Carlo approach [87] are shown, although in most cases the uncertainty is smaller than the symbol plotted. Linear regressions in (A) are fit through the filled symbols and used to determine E_a and $\ln(D_0/a^2)$, assuming an Arrhenian dependence of diffusivity on temperature (Eq. 3.1). Residuals, defined as the difference between the calculated $\ln(D/a^2)$ from a given heating step and the expected $\ln(D/a^2)$ from the linear regression at the same temperature, are plotted against temperature (B) and cumulative gas release fraction (C). Filled symbols are the same as in (A).

Table 3.2: Summary of neon diffusion parameters. 1σ uncertainties are reported.

Sample	Spherical equiv. radius ^a (μm)	E_a (kJ/mol)	\pm	$\ln(D_0/a^2)$	\pm	Apparent D_0 (cm^2/s) ^b
BMk-D	283, 271	91.7	2.1	4.32	0.44	5.52×10^{-2}
FCs-A	308, 276	83.6	1.8	1.14	0.34	2.38×10^{-3}
FCs-C	327, 328	86.3	1.4	1.9	0.24	7.19×10^{-3}
GSS-A	178, 205	83.3	1.5	3.88	0.32	2.04×10^{-2}
SURTp-B	307	94.3	1.2	4.72	0.24	1.06×10^{-1}
OREGp-A	320, 336	102.1	1.9	6.28	0.46	6.03×10^{-1}
GV-09-A	230	103.3	3.5	12.84	0.89	1.99×10^2
76535-B ^c	296, 244	110.7	1.6	0.73	0.32	8.86×10^{-1}

^aSpherically equivalent radii were calculated in several different ways. In the first instance, the radius was calculated from the surface area to volume ratio (SA/V) of the crystal analyzed using optical microscope measurements. For some of the ^{21}Ne stepwise degassing experiments, a second radius is listed that was calculated from the SA/V determined from X-ray computed tomography measurements (Table S2 of Tremblay et al. [144]).

^bStepwise degassing experiment data presented in Garrick-Bethell et al. [126].

^cStepwise degassing experiment data presented in Garrick-Bethell et al. [126].

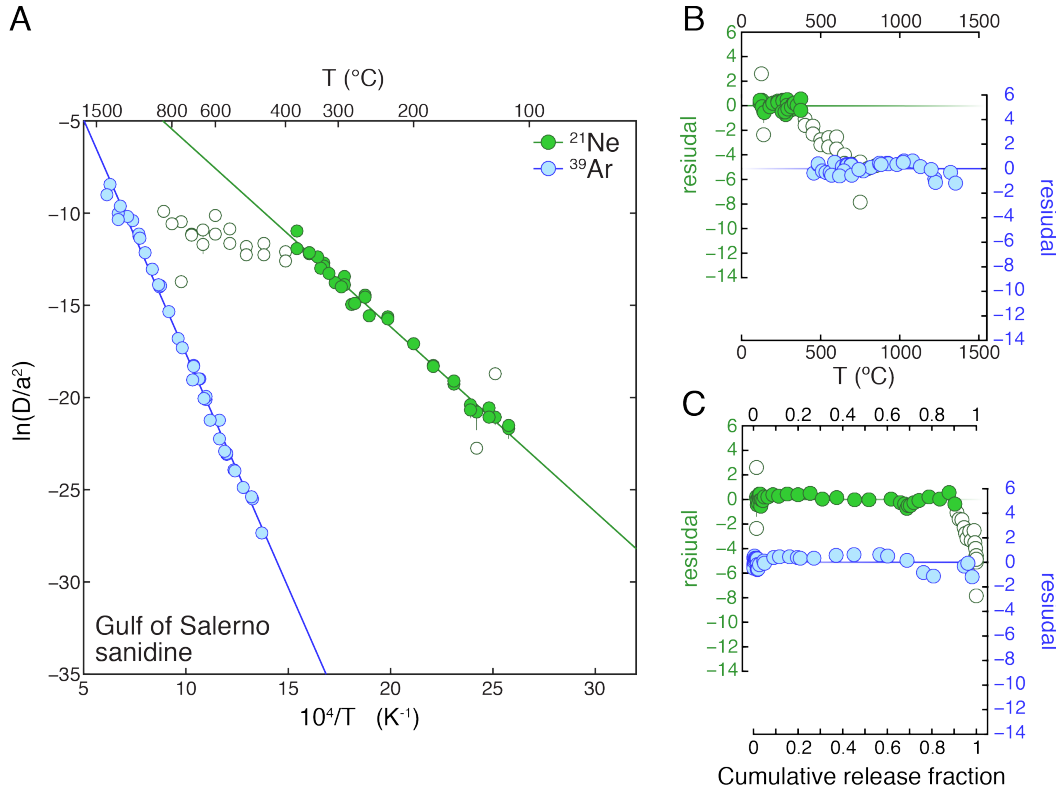


Figure 3.2: Arrhenius plot (A) and residual plots (B-C) for diffusion of proton-induced ^{21}Ne (green) and neutron-induced ^{39}Ar (blue; data from [95]) in different crystals of Gulf of Salerno sanidine. Units, uncertainties, linear regressions, and residuals are as described for Fig. 3.1.

The two neon stepwise degassing experiments we conducted on Fish Canyon sanidine exhibited single linear Arrhenius arrays over the duration of the experiment, which was also observed in replicate argon stepwise degassing experiments (Fig. 3.1). Deviation from linearity occurs at the end of neon experiment A; however, this deviation comprises less than 7% of the cumulative ^{21}Ne released (Fig. 3.1C), and the remaining steps do not form any clear additional linear arrays (Fig. 3.1A). Interestingly, our stepwise degassing experiments using proton-induced ^{21}Ne disagree significantly with the experiment using neutron-induced ^{22}Ne reported by Gourbet et al. [21], which showed complex neon diffusion behavior (Fig. 3.1A). Neon and argon stepwise degassing experiments on Gulf of Salerno sanidine likewise exhibit simple, linear Arrhenius behavior (Fig. 3.2). Although several of the high-temperature steps in the neon stepwise degassing experiment deviate from a linear Arrhenius array (Fig. 3.2B), these steps constitute less than 10% of the cumulative ^{21}Ne released (Fig. 3.2C) and do not form any clear additional linear arrays (Fig. 3.2A).

Feldspars other than sanidine exhibit disparate neon and argon Arrhenius behavior. The neon experiment on Benson Mines orthoclase shows a clear downward deviation from linear

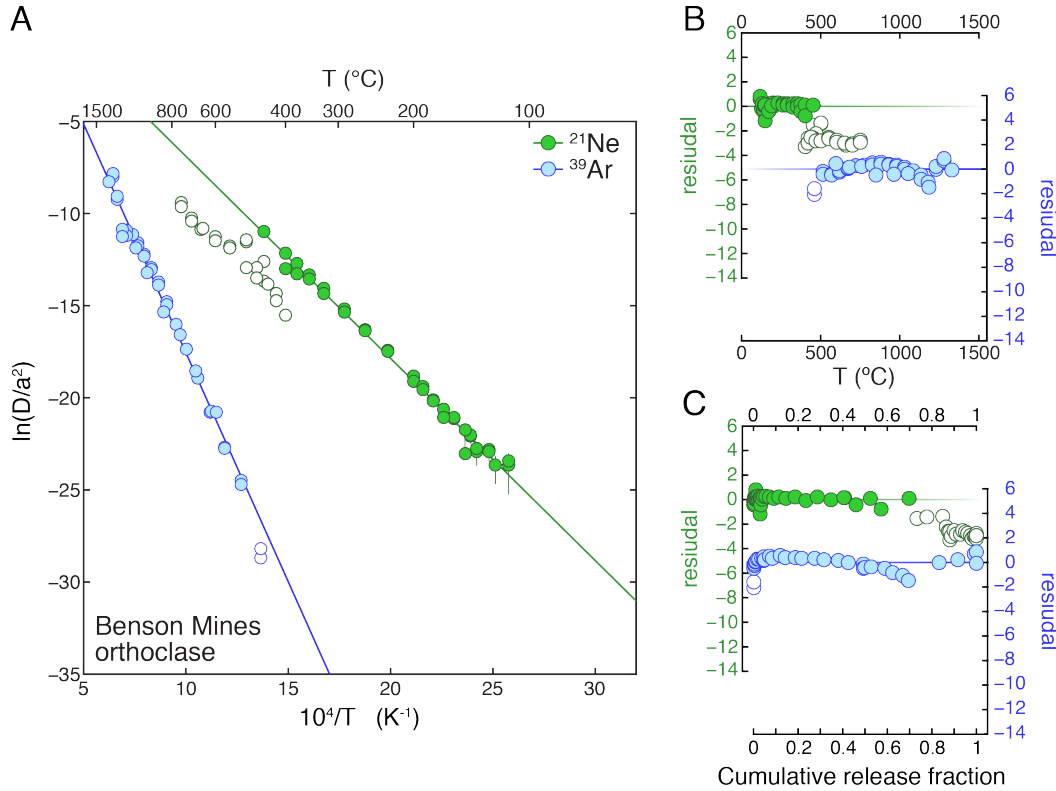


Figure 3.3: Arrhenius plot (A) and residual plots (B-C) for diffusion of proton-induced ²¹Ne (green) and neutron-induced ³⁹Ar (blue; data from [95]) in different crystals of Benson Mines orthoclase. Units, uncertainties, linear regressions, and residuals are as described for Fig. 3.1.

Arrhenius behavior at $\sim 70\%$ of the cumulative ²¹Ne release fraction (Figs. 3.3A and 3.3C). A second linear Arrhenius array, which includes a retrograde heating cycle, is observed at higher ²¹Ne release fractions (Fig. 3.3A). For comparison, we show the results of an ³⁹Ar stepwise degassing experiment reported by Cassata and Renne [95] on an equant crystal of Benson Mines orthoclase with an estimated spherical radius equal to that in the neon experiment. The ³⁹Ar experiment appears to comprise a single linear Arrhenius array (Fig. 3.3A). There is a slight downward deviation in diffusivity between 50 and 70% of the cumulative ³⁹Ar released as well (Fig. 3.3C). However, the steps following this downward deviation occur at temperatures exceeding 1100 °C (Fig. 3.3B), at which point the crystal used in the ³⁹Ar experiment is melting [149, 150]. The two labradorite samples studied from Surtsey, Iceland and Plush, Oregon, both exhibit upward deviations from linear Arrhenius behavior in ³⁷Ar stepwise degassing experiments at temperatures between 600 and 800 °C and at gas release fractions $< 10\%$ (Figs. 3.4 and 3.5; Cassata and Renne, [95]). Essentially all of the ²¹Ne in our stepwise degassing experiment on Surtsey labradorite was released during steps below 600 °C (Fig. 3.4C) and comprises a single linear Arrhenius array (Fig. 3.4A). The

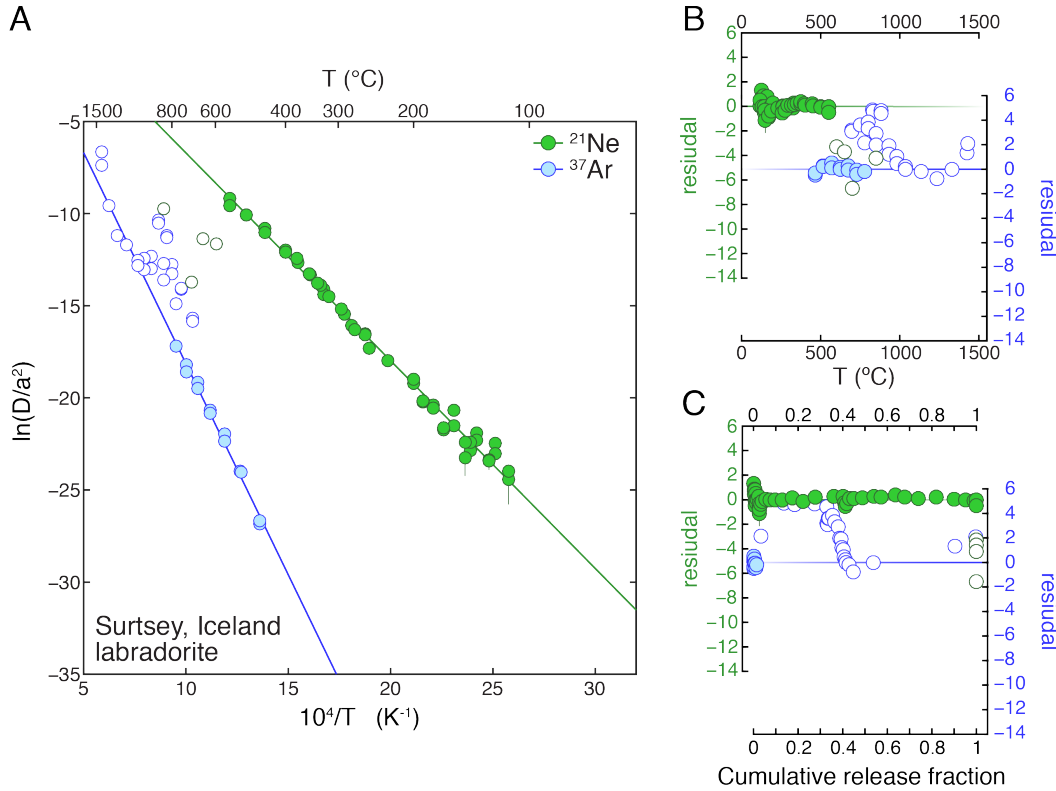


Figure 3.4: Arrhenius plot (A) and residual plots (B-C) for diffusion of proton-induced ²¹Ne (green) and neutron-induced ³⁷Ar (blue; data from [95]) in different crystals of Surtsey, Iceland labradorite. Units, uncertainties, linear regressions, and residuals are as described for Fig. 3.1.

²¹Ne step degassing experiment on Plush labradorite, on the other hand, shows a significant downward deviation from an initial linear Arrhenius array at 350 °C and 25% of the cumulative ²¹Ne released (Fig. 3.5). Lastly, we compare neon and argon degassing experiments on two samples of anorthite, the calcium endmember of plagioclase feldspar. In Grass Valley anorthite, neon and argon both show downward deviations from linear Arrhenius behavior, but at different temperatures and gas release fractions (Fig. 3.6). Anorthite from lunar sample 76535 shows linear Arrhenius behavior for 97% of the ²¹Ne measured but downward deviation from linear behavior at 30% of the cumulative ³⁷Ar and 1000 °C.

For the subset of each dataset comprising a linear Arrhenius array, we find that ²¹Ne activation energies range from 83.3 to 110.7 *kJ/mol* and apparent pre-exponential factors (D_0) range from 2.4×10^{-3} to 1.99×10^2 *cm²s⁻¹*. These diffusion parameters are within the range of those calculated by Gourbet et al. [21] for three alkali feldspars. Activation energies and apparent pre-exponential factors for ²¹Ne diffusion in plagioclase feldspars are generally greater than those in alkali feldspars, although a larger number of neon stepwise degassing

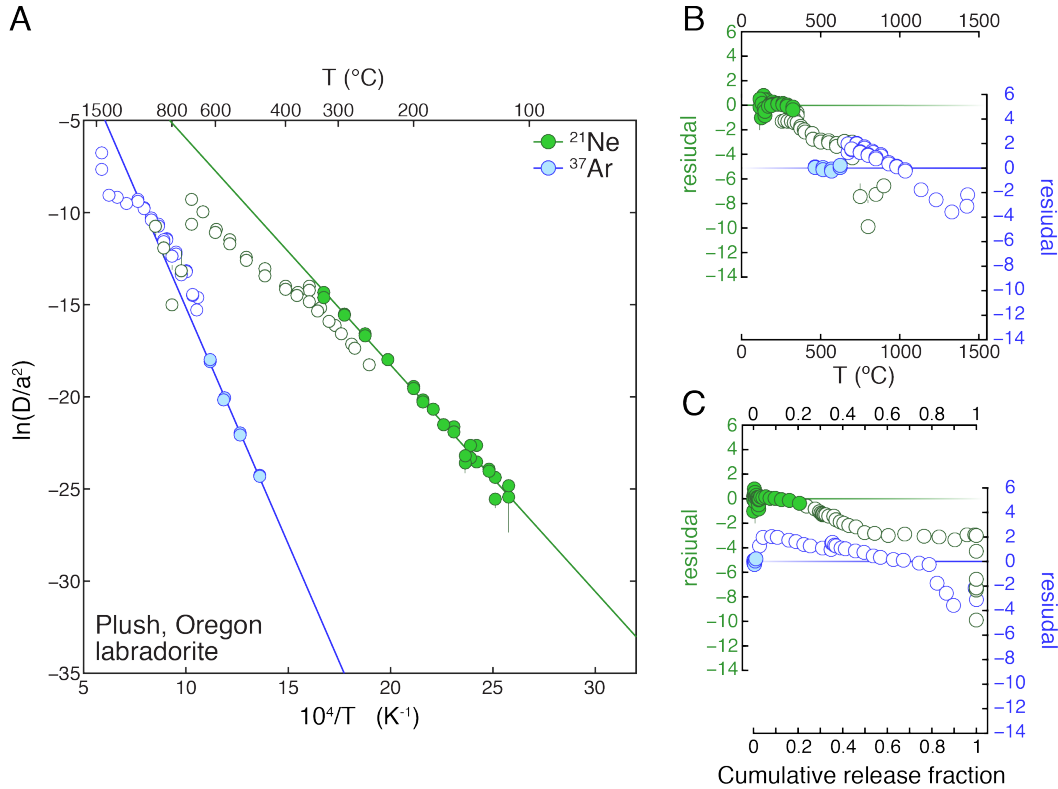


Figure 3.5: Arrhenius plot (A) and residual plots (B-C) for diffusion of proton-induced ^{21}Ne (green) and neutron-induced ^{37}Ar (blue; data from [95]) in different crystals of Plush, Oregon labradorite. Units, uncertainties, linear regressions, and residuals are as described for Fig. 3.1.

experiments are necessary to determine if this trend is systematic. Roughly the opposite trend was observed for the activation energy of argon diffusion as a function of composition [95].

3.5 Discussion

While argon diffusion in feldspars has been studied at length over several decades, this is only the second work to examine neon diffusion in feldspars and the first work to study neon diffusion in plagioclase feldspars. As such, these neon stepwise degassing experiments provide insight into the potential noble gas diffusion mechanisms in feldspars. Below we discuss evidence for both structural modifications and multiple diffusive lengthscales affecting noble gas diffusion in feldspars. For feldspars that exhibit complex neon diffusion behavior, we construct multiple diffusion domain (MDD) models. We use the diffusion parameters from these MDD models as well as the diffusion parameters determined for feldspars ex-

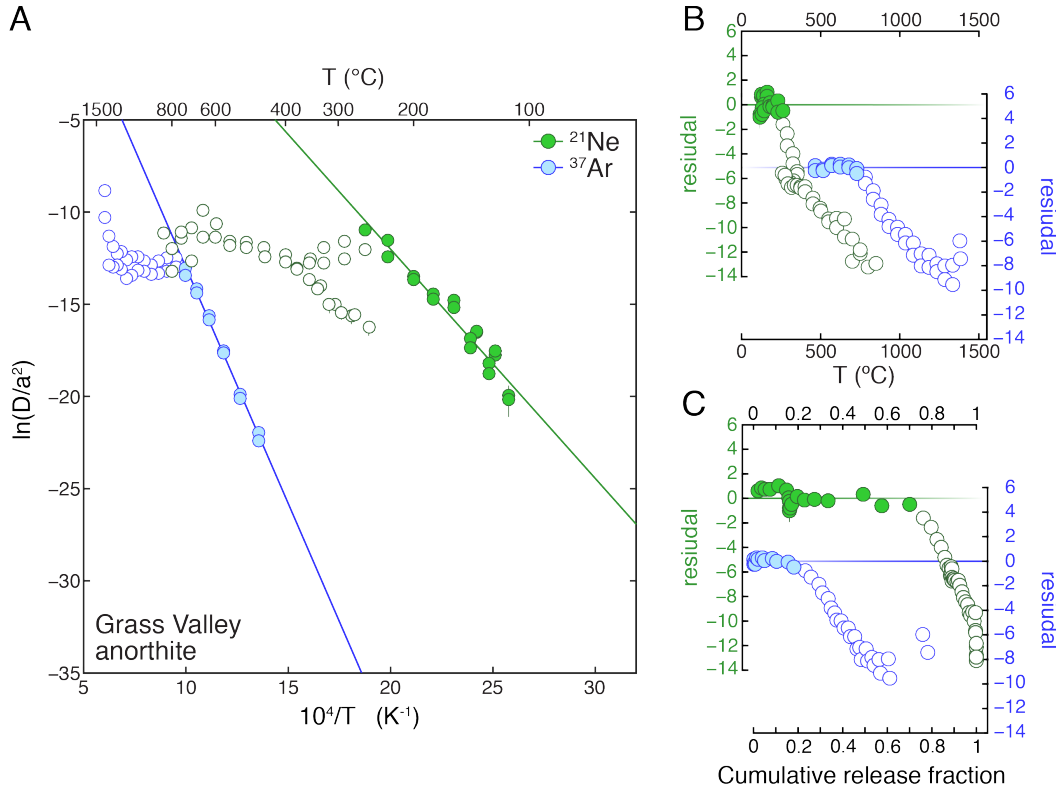


Figure 3.6: Arrhenius plot (A) and residual plots (B-C) for diffusion of proton-induced ²¹Ne (green) and neutron-induced ³⁷Ar (blue; data from [95]) in different crystals of Grass Valley anorthite. Units, uncertainties, linear regressions, and residuals are as described for Fig. 3.1.

hibiting simple Arrhenius behavior to explore the temperatures and exposure durations over which cosmogenic neon-in-feldspar paleothermometry can be applied to study past surface temperatures.

3.5.1 Comparison of neon and argon diffusion

3.5.1.1 Neon and argon diffusion in alkali feldspars

Of the samples we examined, Fish Canyon and Gulf of Salerno sanidine exhibited the simplest Arrhenius behavior for argon diffusion (Figs. 3.1 and 3.2; [95]). A single linear Arrhenius array characterizing all of the ³⁹Ar released during these experiments is consistent with a single diffusion lengthscale, which we assume is equal the grain size analyzed (in which case $a \approx 213, 332,$ and $407 \mu\text{m}$ for Fish Canyon sanidine 1, Fish Canyon sanidine 2, and Gulf of Salerno sanidine respectively, which we estimated from the total amount of ³⁹Ar, the duration of the neutron irradiation, and the stoichiometry of each feldspar). Cassata and Renne [95] also attribute simple behavior to the fact that sanidine has monoclinic

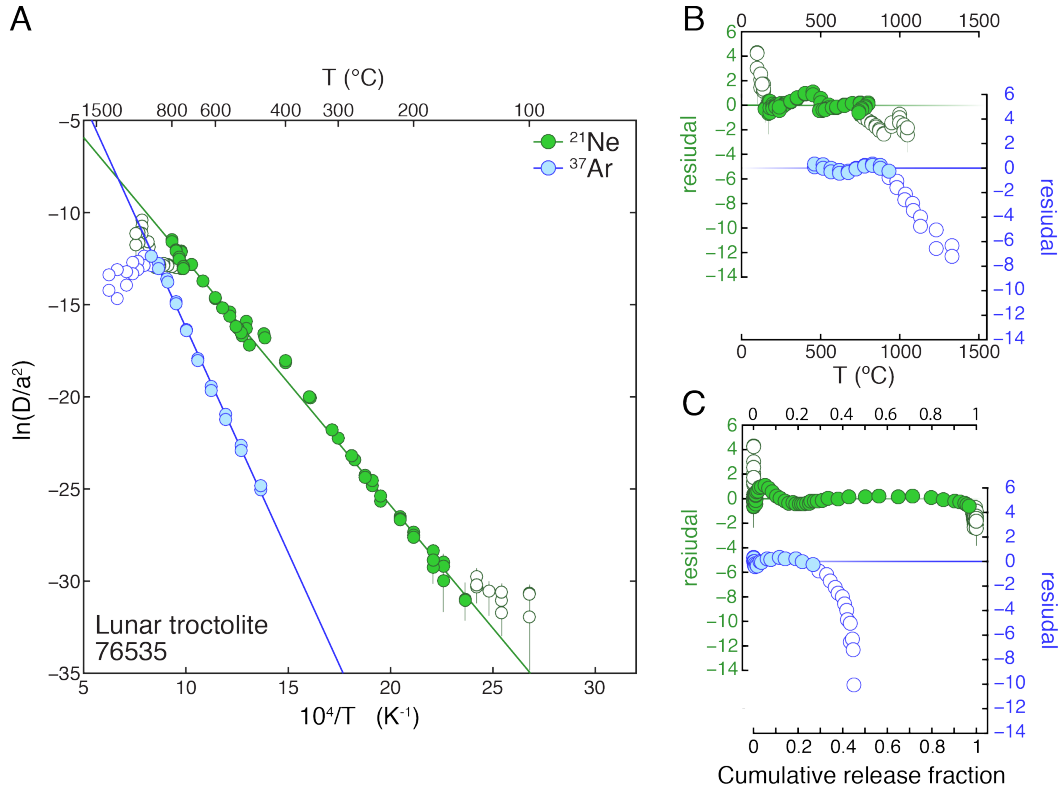


Figure 3.7: Arrhenius plot (A) and residual plots (B-C) for diffusion of proton-induced ²¹Ne (green) and neutron-induced ³⁹Ar (blue; data from [95]) in different crystals of lunar 76535 anorthite. Units, uncertainties, linear regressions, and residuals are as described for Fig. 3.1.

crystal symmetry at room temperature and does not undergo a displacive transition during heating. Consequently, thermal expansion proceeds linearly in all three unit cell directions [151, 152]. Our proton-induced ²¹Ne stepwise degassing experiments on Fish Canyon and Gulf of Salerno sanidine also exhibit simple diffusion behavior, with $\geq 90\%$ of the ²¹Ne degassed plotting on a single linear Arrhenius array and no additional arrays formed from the few high temperatures steps that deviate. The neutron-induced ²²Ne stepwise degassing experiment on Fish Canyon sanidine reported by Gourbet et al. [21] seemingly conflicts with our observation of simple neon diffusion behavior (Fig. 3.1A). One possibility is that the crystal fragment used in the neutron-irradiated experiment was fractured before or during the stepwise degassing experiment. Another possibility is that heating to > 250 °C during neutron irradiation caused some diffusive loss of neon. This latter possibility seems likely given the diffusion kinetics we determined for Fish Canyon sanidine; however, we would expect the initial neon data from the neutron-irradiated experiment to plot below the linear Arrhenius array in the proton-irradiated experiment if this were the case. Gourbet et al. [21] suggest that production of ²²Ne from the spallation reaction $^{23}\text{Na}(n,np)^{22}\text{Ne}$ during

neutron irradiation may have been spatially variable due to core-to-rim zonation of Na in Fish Canyon sanidine [153]. Spatially variable ^{22}Ne production violates the assumption of a uniform initial ^{22}Ne distribution and could lead to curved Arrhenius arrays. However, if spatially variable production of ^{22}Ne from ^{23}Na was the cause of nonlinear behavior, we would expect to observe nonlinear behavior in the argon experiments as well, given that ^{39}Ar is produced from ^{39}K and K is also zoned in Fish Canyon sanidine (Bachmann et al., 2002). Curvature in the proton-irradiated neon experiments might also be expected if this were the case, although spatially variable production from ^{23}Na would be buffered by reactions on Al and Si with similar cross sections [154]. Given these numerous potential complications with the Fish Canyon sanidine experiment reported by Gourbet et al. [21], we suggest that our stepwise degassing experiments using proton-irradiated Fish Canyon sanidine more accurately characterize neon diffusion in that sample. Our ^{21}Ne results, when paired with the ^{39}Ar stepwise degassing experiments, strongly support the case for these sanidine samples having a single diffusion domain with a single diffusion lengthscale, which we assume is defined by the physical grain size. Additionally, the diffusion parameters (E_a and D_0) for Fish Canyon and Gulf of Salerno sanidine are in good agreement with one another for the respective noble gases examined. The diffusion parameters reported in Table 3.2 for Fish Canyon and Gulf of Salerno sanidine can therefore be straightforwardly compared to theoretical calculations (e.g. density functional theory or molecular dynamics simulations) of interstitial neon and argon diffusion through the monoclinic sanidine crystal structure.

The Arrhenius behavior of ^{21}Ne diffusion in Benson Mines orthoclase is somewhat surprising, as monoclinic orthoclase is also expected to undergo linear thermal expansion. Cassata and Renne [95] conducted five argon stepwise degassing experiments on Benson Mines orthoclase, one on an equant fragment (Fig. 3.3) and four on sheet-like cleavage fragments (Fig. S2 of Tremblay et al. [144]). All five experiments exhibit deviations from a linear Arrhenius array at high temperatures and ^{39}Ar release fractions; however, in all experiments these deviations occur near the melting point of orthoclase [149, 150], making it difficult to assess its origin. The ^{21}Ne stepwise degassing experiment on Benson Mines orthoclase, on the other hand, shows a clear downward deviation from linear Arrhenius behavior beginning at 70% of the cumulative ^{21}Ne released and at 500 °C, hundreds of degrees below the melting temperature of orthoclase (Fig. 3.3). There was no visible evidence for fracturing or other alteration when we unpacked the crystal for X-Ray CT analysis, indicating that no change in the physical grain size occurred before or during the experiment. Additionally, a second linear Arrhenius array observed at higher temperatures and gas release fractions in the ^{21}Ne experiment includes a retrograde heating cycle (Fig. 3.3A). If nonlinear Arrhenius behavior resulted from a reversible, temperature-dependent structural transformation, we would expect diffusivities in the retrograde heating to approach diffusivities observed at the same temperatures in the preceding prograde heating, which was not observed. These observations leave two potential explanations for the nonlinear Arrhenius behavior. It is possible that the crystal of Benson Mines orthoclase we analyzed was fractured in a way that was not detected by either optical microscopy or X-ray CT, in which case replicating the neon step degassing experiment on a different crystal of Benson Mines orthoclase would result in different Arrhe-

nius behavior. Alternatively, these results could indicate that nonlinear Arrhenius behavior of ^{21}Ne reflects a preexisting material property (sub-grain domain distribution) of Benson Mines orthoclase. This latter possibility suggests that the same intrinsic property of Benson Mines orthoclase ought to cause nonlinear Arrhenius behavior for argon. Deviations from linearity observed in argon experiments reported by Cassata and Renne [95] occur between 15 and 80% of the Ar released, which at first appears to suggest that sub-grain features defining the diffusion lengthscale vary from grain to grain. However, these deviations all occur near the melting temperature of orthoclase, making the origin of these deviations ambiguous. A straightforward test of this hypothesis would be to conduct another ^{39}Ar stepwise degassing experiment on Benson Mines orthoclase with a revised heating schedule, such that all of the ^{39}Ar is released at temperatures significantly below the orthoclase melting temperature.

3.5.1.2 Neon and argon diffusion in plagioclase feldspars

Our neon stepwise degassing experiments on plagioclase feldspars highlight how the effects of both structural modification during laboratory heating and preexisting material properties can be convoluted to result in nonlinear Arrhenius behavior. Cassata and Renne [95] conducted a number of experiments on labradorite samples, all of which exhibit upward deviations from initial linear Arrhenius arrays at temperatures between 600 and 800 °C. They argue that in labradorite and other Ca-rich feldspars, upward deviations are the result of an increase in the rate of thermal expansion above 600 °C, which has been observed experimentally [152, 155]. This interpretation is consistent with our neon stepwise degassing experiments on Surtsey and Plush labradorite, as we observed no upward deviations from an initial Arrhenius array and degas > 99% of the ^{21}Ne below 600 °C in both experiments (Figs. 3.4 and 3.5). However, in the case of Plush labradorite, we observe a downward deviation from an initial linear Arrhenius array when ~25% of the ^{21}Ne had been released and at 350 °C (Fig. 3.5), a temperature for which no changes in the rate of thermal expansion are expected. Like our neon degassing experiment on Benson Mines orthoclase, retrograde heating steps in the Plush labradorite experiment do not overlap with the initial linear Arrhenius array, confirming that this behavior is not a result of a reversible structural change. If we assume that the crystal of Plush labradorite was not fractured, these results instead suggest that complex neon diffusion behavior reflects a preexisting material property of Plush labradorite. A very small fraction (< 10%) of the total gas is released below 600 °C in argon stepwise degassing experiments; therefore the effects of this preexisting material property are likely obscured by the coincident changes in rate of thermal expansion. Without the observation of temperature-independent complex Arrhenius behavior from the neon stepwise degassing experiment on Plush labradorite, simple down-temperature extrapolation of the initial linear Arrhenius array in the argon stepwise degassing experiment to geologically relevant temperatures may have seem justified. However, doing so would likely result in inaccurate thermal history reconstruction. In contrast to Plush labradorite, with Surtsey labradorite we observe a single linear Arrhenius array for ^{21}Ne (Fig. 3.4), suggesting this labradorite is characterized by a single diffusion domain with a single diffusion length-

scale, which may be defined by the physical grain size ($a \approx 307 \mu\text{m}$). Furthermore, this implies that nonlinear behavior for Ar diffusion, manifest as upward curvature on Arrhenius plots at $\sim 600 \text{ }^\circ\text{C}$, followed by downward curvature at higher temperatures, is likely related to structural modifications of the feldspar in response to heating [95]. Accurate geologic thermal history information could therefore be inferred for Surtsey labradorite by downward extrapolation of initial linear Arrhenius arrays.

Unlike the other feldspars we studied, anorthite undergoes a structural transition during neon stepwise degassing experiments. Between 225 and 300 $^\circ\text{C}$, anorthite transitions from a P1 to T triclinic crystal symmetry [156, 157]. The P1–T transition is accompanied by an increase in unit cell volume and in the rate of thermal expansion [155], both of which ought to decrease the energy barrier to interstitial diffusion and increase noble gas diffusivities. Therefore we expect to observe upward deviations from initial linear Arrhenius arrays associated with this transition in neon stepwise degassing experiments but not in argon stepwise degassing experiments, as the latter take place at temperatures above the P1–T transition. In the ^{21}Ne stepwise degassing experiment on Grass Valley anorthite, we observed the opposite: downward deviation from an initial linear Arrhenius array occurred at 300 $^\circ\text{C}$ (Fig. 3.6). However, we do not find this surprising given the crystallochemical complexity of Grass Valley anorthite, which is characterized by two phases of anorthite separated by antiphase boundaries, as well large muscovite inclusions, plagioclase subgrains, and Na-rich feldspar alteration patches [158, 159]. Thus we anticipate both the diffusion kinetics and initial distribution of neon to be spatially variable in this sample. Given this heterogeneity, it is also expected that the argon and neon diffusion experiments on different aliquots of Grass Valley anorthite are not reconcilable with one another. A neon stepwise degassing experiment on neutron-irradiated anorthite from lunar sample 76535 [126] exhibits linear Arrhenius behavior between 170 and 800 $^\circ\text{C}$ for essentially all of the gas released (Fig. 3.7). There appears to be a slight upward deviation in the diffusivities at $\sim 300 \text{ }^\circ\text{C}$, which may be associated with the P1–T transition. However, fitting a linear regression to only the data collected below 300 $^\circ\text{C}$ yields indistinguishable diffusion parameters from those calculated using all the data. Linear Arrhenius behavior at temperatures below 800 $^\circ\text{C}$ in the neon experiment is also consistent with the downward deviation from an initial linear Arrhenius array above 800 $^\circ\text{C}$ in the argon experiment being caused by the transition to an I1 symmetry [160, 161].

To summarize our comparison of neon and argon stepwise degassing experiments, we often see different Arrhenius behavior for neon diffusion than was observed for argon diffusion in the same feldspars. The origin of these differences depends on the feldspar in question. In several cases, the effects of a preexisting material property of a particular feldspar and the effects of a structural transformation during laboratory heating are conflated in argon stepwise degassing experiments; neon stepwise degassing experiments conducted at lower temperatures make such conflations apparent. It would be valuable to measure neon and argon isotopes simultaneously in future stepwise degassing experiments on neutron-irradiated feldspars in order to discern between such effects.

3.5.2 Multiple diffusion domain (MDD) model for neon diffusion in feldspars

At present, we cannot ascribe a specific intrinsic property or mechanism to nonlinear Arrhenius behavior that is not associated with a temperature-dependent structural transformation. Identifying the origin of this complex Arrhenius behavior in argon stepwise degassing experiments is critically important, because crystallochemical changes that could potentially be responsible for this behavior (e.g. strain-induced microtextural development, fluid alteration) may have occurred during the portion of a sample's geologic thermal history that is relevant to $^{40}\text{Ar}/^{39}\text{Ar}$ thermochronometry. For cosmogenic noble gas thermochronometry using neon in feldspars, wherein production and diffusion are only happening at planetary surfaces where feldspars are exposed to cosmic ray particles, we expect any major crystallochemical changes to have occurred at much higher temperatures than are relevant to the system of interest. In other words, all crystallochemical heterogeneities are present throughout the thermal history recorded by cosmogenic neon in feldspars, with the possible exception of those generated by shock during impact events. Thus although we do not have a mechanistic explanation for the nonlinear, temperature-independent Arrhenius behavior observed in some neon experiments, we think this complex behavior characterizes cosmogenic neon diffusivity and therefore must be accounted for to accurately reconstruct temperatures using cosmogenic neon in feldspars.

In order to account for complex neon diffusion in feldspars, we modeled the results of stepwise degassing experiments exhibiting complex Arrhenius behavior using multiple diffusion domain (MDD) theory [113, 134, 135]. MDD theory explains nonlinear Arrhenius behavior as the result of diffusion from multiple, non-interacting subgrain domains of varying sizes. Our modeling approach is similar to that described in Tremblay et al. [87], wherein diffusivities are calculated for the experiment heating schedule using the equations outlined by Fechtig and Kalbitzer [82] for a spherical geometry and for a given diffusion domain distribution. The number of subgrain domains was allowed to vary, and the models were designed to search over a large number of combinations of activation energy (E_a), pre-exponential factor (D_0/a^2), and gas fraction (f) attributed to each domain; activation energy was held in common for all domains. For a particular number of diffusion domains, we determined the combination of diffusion parameters and gas fractions that best agreed with the stepwise degassing experiments by calculating a misfit statistic M :

$$M = \sum_{j=1}^n |f_{p,j} - f_{m,j}| \quad (3.2)$$

where $f_{p,j}$ is the modeled cumulative ^{21}Ne released at heating step j , $f_{m,j}$ is the observed cumulative ^{21}Ne released at heating step j , and n is the total number of heating steps. This misfit statistic is analogous to the reduced chi-squared misfit statistic used in Tremblay et al. [87] in that the same set of diffusion parameters minimizes both quantities. However, the cumulative difference in predicted and observed gas fractions used here has more physical

meaning. For example, a misfit statistic of 0.15 can be thought of as not predicting 15% of the observed ^{21}Ne released with our MDD model. We continued to add diffusion domains until the minimized misfit statistic with $x + 1$ domains was within 0.03 of the minimized misfit statistic with x domains. In Fig. 3.8, we show the best fit MDD models for the neon stepwise degassing experiments on Benson Mines orthoclase, Plush labradorite, and Grass Valley anorthite; best fit diffusion parameters, gas fractions, and misfit statistics are reported in Table 3.3. By assuming that this model framework can be extrapolated over time and to lower temperatures, we use the MDD model fits for these feldspars in the remaining discussion to assess the sensitivity of cosmogenic neon-in-feldspar paleothermometry to exposure temperature and duration.

Table 3.3: Best fit multiple diffusion domain model parameters.

Sample	Domain	E_a (kJ/mol)	$\ln(D_0/a^2)$	f	Misfit
BMk-D	1	91.5	4.0	0.45	0.17
	2		5.6	0.3	
	3		1.2	0.25	
OREGp-A	1	96.9	2.4	0.74	0.16
	2		7.4	0.26	
GV-09-A	1	108.4	14.9	0.76	0.33
	2		19.2	0.08	
	3		8.0	0.08	
	4		4.3	0.08	

3.5.3 Implications for neon retentivity in feldspars

The seven neon stepwise degassing experiments reported here, combined with the experiments reported by Gournbet et al. [21] and Garrick-Bethell et al. [126], demonstrate that neon diffusion kinetics and behavior vary widely amongst feldspars of different compositions and geologic origins. This is perhaps not surprising, given the vast range of diffusion kinetics and behavior observed in argon stepwise degassing experiments [e.g. 95, 114, 138]. Nonetheless, the variability of neon diffusion kinetics and behavior has important implications for the applicability of laboratory-determined diffusion kinetics to applications of cosmogenic neon paleothermometry [68]. Specifically, these results indicate that sample-specific diffusion kinetics will be necessary to quantitatively reconstruct temperatures using cosmogenic neon in feldspars.

To illustrate this point, in Fig. 3.9 we show how cosmogenic neon retentivity will evolve as a function of exposure duration for a constant exposure temperature of 20 °C using the different diffusion parameters obtained in neon stepwise degassing experiments. Retentivity refers to the amount of cosmogenic neon produced during exposure to cosmic ray particles

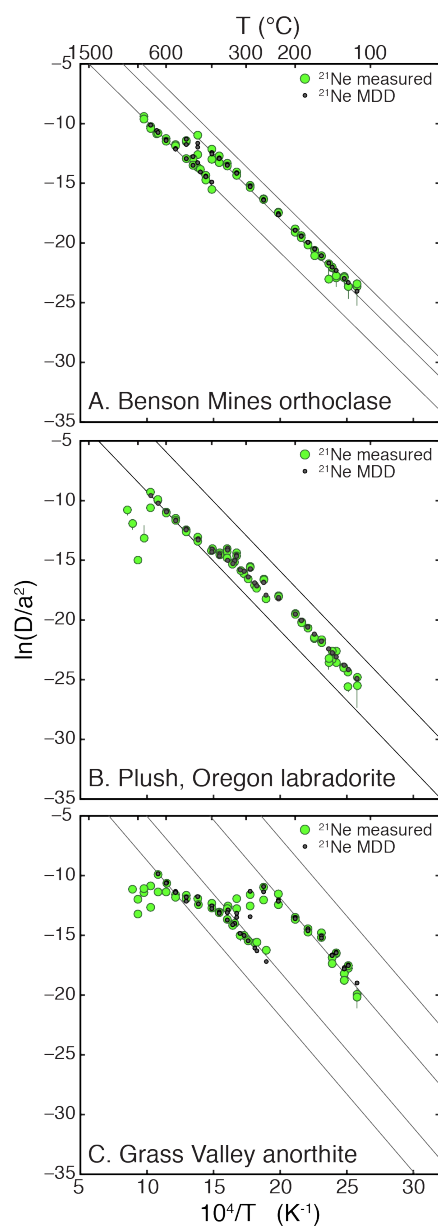


Figure 3.8: Arrhenius plots comparing calculated diffusivities from multiple diffusion domain (MDD) models (black) to calculated diffusivities from neon stepwise degassing experiments (green) for Benson Mines orthoclase (A), Plush labradorite (B), and Grass Valley anorthite (C). Lines correspond to diffusion parameters characterizing each diffusion domain, which are listed in Table 3.3 along with the fraction of gas comprising each domain and the misfit statistic of the models shown.

that has not diffused out of the feldspar; thus a retentivity of one indicates no diffusive loss, while a retentivity asymptoting to zero indicates that steady-state between production and diffusion has occurred. For feldspars exhibiting linear Arrhenius behavior, we assume that the physical grain size defines the diffusion lengthscale of a single diffusion domain and scale diffusivities to a common diffusion lengthscale of $500 \mu\text{m}$; retention curves for these feldspars are shown in Fig. 3.9A. Having normalized the diffusion lengthscale, we can see in Fig. 3.9A that differences in diffusion parameters (E_a and D_0) amongst different feldspars results in significant variability in retentivity. For example, while lunar 76535 anorthite is expected to retain all of its cosmogenic neon over 10 Ma of exposure at 20°C , Easy Chair Crater anorthoclase would retain $< 10\%$ given the same exposure history. In cases where we used MDD models to infer neon diffusion parameters, we do not know the diffusion lengthscale of the different domains as this cannot be separated from the pre-exponential factor D_0 without making additional assumptions. Furthermore, it is likely that the domain size distributions in feldspars exhibiting MDD-like behavior would depend on macroscopic grain size in a way that we cannot quantify. We therefore did the calculations in Fig. 3.9B using the spherically equivalent radius of each feldspar crystal analyzed in the stepwise degassing experiment. Fig. 3.9B highlights the difference in cosmogenic neon retentivities that would be expected for simple extrapolation of initial linear Arrhenius arrays versus MDD model calculated diffusion parameters in feldspars exhibiting complex Arrhenius behavior. For some feldspars such as Benson Mines orthoclase, the differences are small until very long exposure durations are reached ($> 1 \text{ Ma}$); for others such as Grass Valley anorthite, the differences become important on much shorter timescales ($> 0.01 \text{ Ma}$).

In previous theoretical calculations on the sensitivity of cosmogenic neon-in-feldspar paleothermometry [68], we used the diffusion kinetics for Madagascar cryptoperthite reported by Gourbet et al. [21]. However as can be seen in Fig. 3.9, we predict lower cosmogenic neon retentivity using neon diffusion kinetics from most of the feldspars we examined than when using Madagascar cryptoperthite kinetics. This means that the applicability of cosmogenic noble gas paleothermometry to geologic problems will vary depending on the specific feldspar and surface temperature environment. For example, Kober et al. [29] measured cosmogenic ^{21}Ne abundances in sanidine from a welded tuff in the Atacama Desert that were indistinguishable from what would be expected given theoretical ^{21}Ne production rates for sanidine and the known exposure duration, suggesting that no diffusive loss of cosmogenic ^{21}Ne occurred. Complete cosmogenic ^{21}Ne retention suggests that the sanidine studied by Kober et al. [29] is significantly more retentive to neon than the two sanidine samples we conducted stepwise degassing experiments on here, especially given the high amplitude temperature variations and peak temperatures that rocks experience in extreme environments like the Atacama Desert [50, 51]. Similarly, the lunar surface experiences extreme variations in temperature during a lunar day cycle, with peak temperatures in excess of 100°C and temperature minima less than -150°C [162]. However, because lunar 76535 anorthite is so retentive, Garrick-Bethell et al. [126] were able to measure cosmogenic neon abundances in multiple anorthite grains and calculate an accurate estimate of the effective lunar surface temperature ($75.5 \pm 4.2^\circ\text{C}$) over the 142 Ma exposure history of sample 76535. For any of

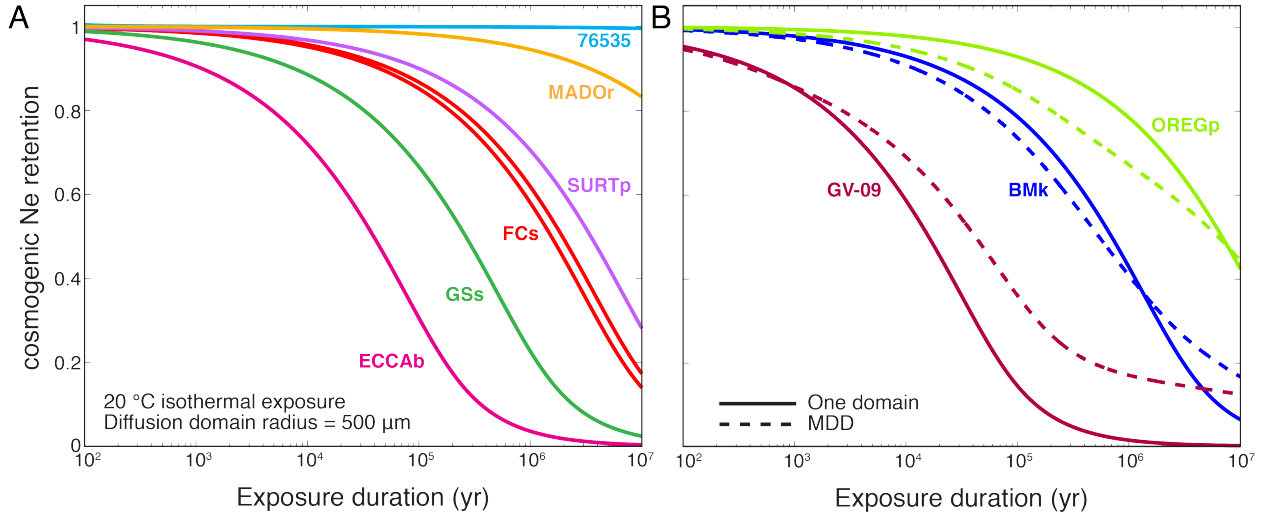


Figure 3.9: Demonstration of the variability of neon retentivity in feldspars. Using the neon diffusion parameters reported here and elsewhere [21, 126], we calculate how neon retention evolves as a function of exposure duration assuming a constant exposure temperature of 20 °C after Wolf et al. [37]. In (A), we show neon retention curves for the six feldspars that exhibit relatively simple linear Arrhenius behavior. Simple linear Arrhenius behavior suggests that the physical grain size defines the diffusion lengthscale for these feldspars; therefore we normalized the diffusion lengthscale to a common spherically equivalent radius of 500 μm . In (B), we show neon retention curves for exhibiting complex Arrhenius behavior using diffusion parameters calculated both from the initial linear Arrhenius array (solid curves) observed in stepwise degassing experiments as well as using an MDD model (dashed curves). As discussed in the text, we use the grain size analyzed in the stepwise degassing experiment for these calculations, as there is no straightforward way to normalize the diffusion lengthscale for feldspars exhibiting complex diffusion behavior.

the diffusion parameters we obtained for the other feldspars, we would predict substantially lower and incorrect effect lunar surface temperatures.

3.6 Conclusions

We present stepwise neon degassing experiments on feldspars of various compositions and geologic origins. This suite of experiments reveals that neon diffusion behavior and kinetics vary significantly amongst different feldspars. Comparison with argon stepwise degassing experiments on the same feldspars provides insight into the source of complex noble gas diffusion behavior. For some feldspars, the absence of nonlinear Arrhenius behavior in neon experiments conducted at lower temperatures suggests that the nonlinear behavior observed in argon experiments resulted from temperature-dependent structural transformations. For

other feldspars, nonlinear Arrhenius behavior observed in both neon and argon experiments suggests that some sample-specific material property is contributing to complex diffusion behavior. When extrapolated down to planetary surface temperatures, the set of available neon diffusion kinetics predicts a wide range of temperatures and exposure durations over which cosmogenic noble gas paleothermometry may be applicable. This wide range indicates that (1) sample specific diffusion kinetics will be necessary for quantitative applications, and (2) the temperature sensitivity of cosmogenic noble gas paleothermometry will depend greatly on a combination of the specific feldspar and surface thermal environment of interest.

3.7 Acknowledgements

We thank R. Wenk and D. Mark for providing samples. We also thank N. Fylstra, T. Becker, and J. Maisano for analytical assistance. AE Greg Herzog and three reviewers provided constructive feedback that strengthened this work. We acknowledge support from the NSF Petrology and Geochemistry Program (EAR-1322086), the UC Berkeley Larsen Grant, and the Ann and Gordon Getty Foundation. MMT was supported by an NSF Graduate Research Fellowship.

Chapter 4

Applications of cosmogenic noble gas paleothermometry to questions in Earth and planetary science

A portion of this chapter was previously published within Garrick-Bethell, I., Weiss, B.P., Shuster, D.L., Tikoo, S.M., and Tremblay, M.M., *Journal of Geophysical Research: Planets* **120** (2017). doi:10.1002/2016JE005154.

4.1 Abstract

Here, we present two applications of cosmogenic noble gas paleothermometry: one to a question in paleoclimate and one to a question in planetary science. Together, these two applications are representative of the range of potential temperatures and geologic problems that can be addressed with cosmogenic noble gas paleothermometry, and highlight some of the challenges associated with applying the technique at each end of the spectrum.

First, we explore whether cosmogenic noble gas paleothermometry can be used to constrain temperatures in the Maritime Alps of Italy since the last glacial maximum (LGM). While an extensive network of Late Quaternary proxy records has been used to quantitatively reconstruct climate parameters throughout much of the European Alps, only qualitative proxy data extend back to the LGM in the Maritime Alps, where it has been hypothesized that climatic conditions and glacier dynamics differed from other Alpine sectors during deglaciation. Here, we present measurements of cosmogenic ^3He in quartz from boulders in a series of nested moraines in the Gesso Valley, Italy. Paired with previous constraints on the exposure duration of these boulders from cosmogenic ^{10}Be measurements and with ^3He diffusion experiments on proton-irradiated quartz fragments, we use the cosmogenic ^3He measurements to place constraints on the possible temperatures these boulders experienced during their exposure since the LGM. To a first order, effective diffusion temperatures (EDTs) over the last ~ 22 thousand years—calculated from the cosmogenic ^3He measure-

ments and sample-specific diffusion kinetics—are broadly consistent with temperatures inferred from other proxies in the nearby Alps and with temperature estimates from a general circulation model (GCM). In detail, however, we calculate significantly different EDTs for boulders sampled from the same moraines. These discrepancies could result from (1) the fact that we have not accounted for variations in radiative heating of the boulder surfaces (e.g, due to variations in overhead vegetation cover or snow cover), (2) limitations in our understanding of and ability to model accurately complex helium diffusion kinetics, (3) uncertainties associated with our grain size analyses, or (4) some combination of the three. Additional work to understand the effects of radiative heating and to better understand complex diffusion kinetics is necessary to provide better resolution on temperatures since the LGM in this setting.

Second, we present the results of a neon diffusion experiment and cosmogenic neon measurements on plagioclase feldspar grains from lunar sample 76535. Sample 76535, collected during the Apollo 17 mission, has the oldest known (4.25 Ga) paleomagnetic record for the Moon and provides the strongest evidence that the Moon had an early core dynamo. Understanding the thermal history of 76535 is key to the interpretation that the paleomagnetic record is primary, and therefore 4.25 Ga old. With the neon diffusion kinetics and cosmogenic isotope measurements we present here and in Garrick-Bethell et al. [126], we demonstrate that 76535 has experienced an EDT of 75.5 ± 4.2 °C over 142 Ma of exposure to cosmic ray particles at the lunar surface. An EDT of 75.5 ± 4.2 °C is in excellent agreement with EDTs determined from cosmogenic argon measurements in other lunar samples as well as with ground temperature measurements made at the Apollo 17 landing site. Therefore the cosmogenic neon isotope abundances observed in 76535 are most consistent with diurnal radiative heating by the Sun only; there is no evidence for impact-related heating after its initial exposure to cosmic ray particles. Paired with existing argon isotope thermochronometric constraints, these results support the interpretation that the paleomagnetic record in 76535 is primary and therefore that the Moon had an early core dynamo.

4.2 Introduction

Past surface temperatures on Earth and other planetary bodies can, in principle, be reconstructed using observations of cosmogenic noble gases, such as ^3He and ^{21}Ne , in mineral phases that experience simultaneous production and diffusive loss of these gases at surface temperatures [68]. Experiments quantifying the diffusion kinetics of ^3He in quartz and ^{21}Ne in feldspars confirm that these noble gas–mineral pairs are sensitive to surface temperature conditions [87, 144]. These experiments also demonstrate that noble gas diffusion kinetics vary significantly between mineral samples of different geologic origins, and that sample-specific diffusion kinetics are necessary for quantitative temperature reconstructions using cosmogenic noble gas observations. Here, we present two applications of cosmogenic noble gas paleothermometry to problems in Earth and planetary science that span the range of timescales and temperatures over which this technique can potentially be utilized. In

both applications, we combine measurements of cosmogenic noble gas isotope abundances with experimentally-determined, sample-specific noble gas diffusion kinetics to quantitatively model the samples' temperature histories during exposure to cosmic ray particles. While some bounds on the temperature histories in both applications can be inferred from other proxy records, observations, and models, the specific thermal histories are unknown.

4.2.1 Reconstructing Late Quaternary temperatures in the Maritime Alps, Italy

In this first application, we attempt to reconstruct temperatures since the last glacial maximum (LGM) using cosmogenic ^3He measurements in quartz from moraine boulders in the Gesso Valley. The Gesso Valley is located in the southernmost Maritime Alps of Italy approximately 40 km from the Gulf of Genoa in the Mediterranean Sea (Fig. 4.1) and was extensively glaciated during the last glacial period. Glacial moraine complexes and other geomorphic features have been mapped throughout the basin [163], and cosmogenic ^{10}Be exposure ages have been determined for boulders from three moraine complexes that span from the LGM to the Younger Dryas (YD) cold period [164–166]. A number of younger, undated moraines are preserved in the valley at higher elevations (Fig. 4.1), and small glaciers restricted to the highest elevation cirques persist today [166]. Methodologically, the presence of numerous moraines with different exposure ages within the same valley is advantageous because it allows us to reconstruct temperatures over different time intervals for an area with a shared climate history (with the caveat that the moraines are at substantially different elevations, as will be discussed later).

Constraints on temperatures since the LGM in the Gesso Valley and the Maritime Alps are scientifically interesting for several reasons. Due to the Maritime Alps' (1) southerly latitude, (2) generally lower elevations and (3) proximity to the Mediterranean Sea, the Late Quaternary climatic evolution and glacier dynamics in this region likely differed substantially from those in Alpine regions further north and further inland, despite the apparent synchronicity of glacier advances during stadials recorded by moraines throughout the region [e.g. 18, 166, 167]. However, our knowledge of deglacial climate conditions in the Maritime Alps from proxy records is somewhat limited. While there are a handful of pollen-based reconstructions from the Maritime Alps of particular climate parameters, such as mean temperature during the coldest month and mean annual precipitation, through the Holocene [10, 168–171], no records from the region extend back to the LGM. Similarly, there is only one reconstruction of mean July temperatures from fossil assemblages of chironomids (midges) proximal to the Maritime Alps from Lago Piccolo di Avigliana with coverage from 14 to 9.5 thousand years ago [172]. There are only two proxy studies from the Maritime Alps that extend into the latest Pleistocene which we are aware of—one reporting pollen fossil assemblages in sixteen high elevation (> 1700 m) lakes [173] and one reporting fossil chironomid assemblages from Lac Long Inférieur in France [174]—and neither study interprets the proxies in terms of quantitative climate parameters. Reconstructing temperatures in the

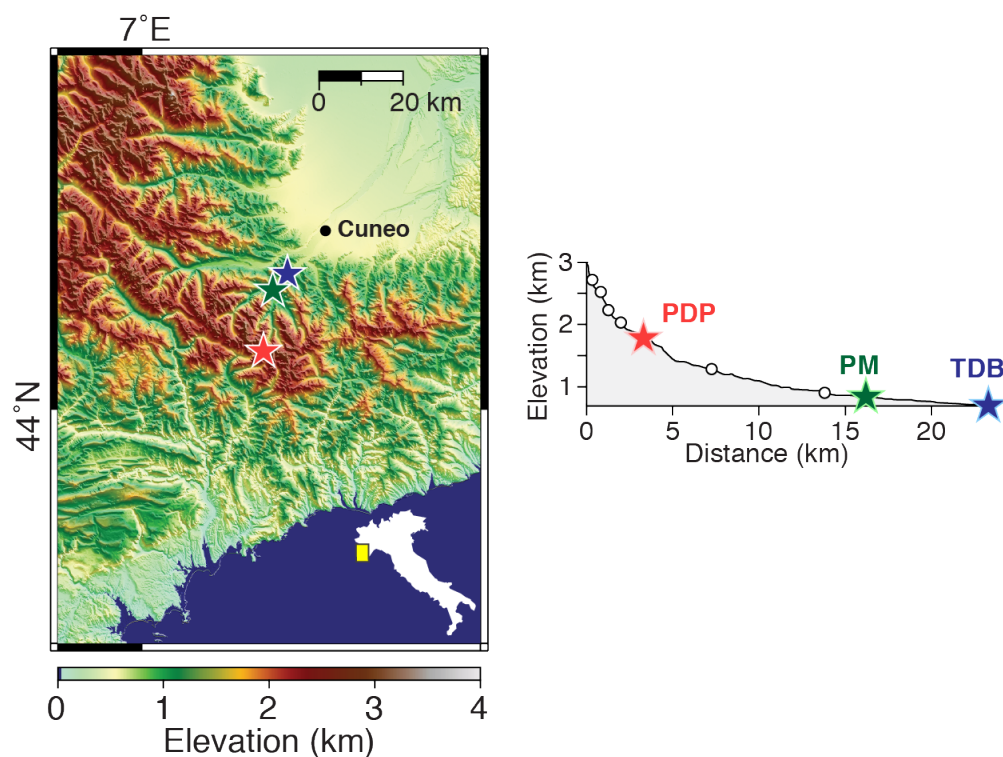


Figure 4.1: Sample locations in the Maritime Alps of Italy. The map shows the topography of the Gesso Valley and surrounding areas and the locations of the three moraines sampled: Piano del Praiet (PDP), Ponte Murato (PM), and Tetti del Bandito (TDB). Map location is shown in the inset of Italy. The longitudinal profile shows the moraine locations with respect to elevation along the Gesso Valley. White circles denote moraine complexes in the Gesso Valley not studied here.

Gesso Valley from the LGM to the present with cosmogenic noble gas paleothermometry would therefore fill a gap in an otherwise extensive network of proxy-based reconstructions of post-LGM climate across Europe [e.g. 10, and references therein], and address the specific question of how climate evolution in the Maritime Alps during deglaciation differed from other Alpine sectors. For example, in combination with the positions and chronology of moraines, a well-resolved local temperature record could be used to inform a simple glacier mass balance model in the Gesso Valley during the deglacial period. With independent constraints on deglacial temperatures, a mass balance model could be used to invert (in a crude sense) for changes in precipitation during deglaciation [e.g. 175]. This paired temperature-precipitation reconstruction could then be compared to proxy records further north and further inland in the Alps to assess how climate and glacier dynamics varied across the region during deglaciation.

In addition to assessing climatic variability during deglaciation across the European Alps,

temperature records from cosmogenic noble gas paleothermometry could provide needed tests of different methodologies for reconstructing climate parameters over this time interval. Reconstructions of climate parameters from existing proxies in the European Alps commonly exhibit significant disagreement with climate model simulations prior to the Holocene. Pollen-based reconstructions suggest much lower temperatures, particularly in the winter, than the models simulations [e.g. 176], while models suggest higher summertime temperatures than chironomid-based reconstructions during interstadials [177]. It is unclear whether these disagreements are attributable to limitations in the general circulation models (GCMs) used to simulate paleoclimate, a breakdown in the assumptions of biologically-based reconstructions, or some combination of both. Having independent pre-Holocene temperature proxies in the European Alps that are mechanistically governed by different processes would therefore help in assessing the cause of the current proxy-model discrepancies.

4.2.1.1 Existing proxy constraints on the Late Quaternary climate of the Maritime Alps

Over the historical period, the Maritime Alps are characterized by higher mean annual temperatures (MAT), smaller annual temperature amplitudes, lower mean annual precipitation (MAP), and snow cover that is thinner and lasts for smaller fraction of the year than in other Alpine sectors [178, 179]. The Maritime Alps most likely remained the warmest Alpine sector during the Late Quaternary, given that the Maritime alps are $\sim 6^\circ$ south of the northernmost eastern Alps, and thus would have experienced greater insolation and generally higher temperatures during this time period. Warmer overall conditions are consistent with species distribution and phylogeographical models, which suggest that the Maritime Alps remained significantly warmer than other parts of the Alps and functioned as a refugium for plant species during the last glacial period [180]. However, temperature and precipitation anomalies in the Maritime Alps during specific climatic intervals of the Late Quaternary may have been distinct from other Alpine sectors. For example, during the Mid-Holocene Warm Period 6,000 years ago, pollen-based reconstructions indicate that Maritime Alps winters may have been as much as 2–3 °C colder than today, while throughout the rest of the Alps winter temperatures were comparable to today [10, 168, 170]. For the same time period, pollen-based reconstructions indicate that the Maritime Alps were wetter ($\Delta P - E > 0$) during the Mid-Holocene, while the rest of the Alps were dryer ($\Delta P - E < 0$) [10, 168].

No proxy-based reconstructions from the Maritime Alps extend back to the LGM. The nearest pollen-based reconstructions indicate 15–20 °C lower winter temperatures and ~ 500 mm/yr lower MAP during the LGM than today [10, 176]. For the Mediterranean region as a whole, LGM winter temperatures range anywhere from 0 to 30 °C lower than today, while MAP varies between 0 and 800 mm/yr less than today [170]. In contrast to pollen-based reconstructions, Kuhlemann et al. [167], to explain spatial patterns of Mediterranean sea surface temperatures (SSTs) and ELA depressions, suggested that incursions of cold polar air between the Pyrenees and the Alps were more frequent during the LGM. These incursions would have resulted in greater moist air convection and cyclogenesis as these air

masses encountered the warm SSTs in the Gulf of Genoa and therefore greater precipitation in the Maritime Alps and other Mediterranean-proximal glaciated areas (e.g., Corsica). The interpretation of Kuhleemann et al. [167] implies wetter conditions in the Maritime Alps, not dryer as suggested by pollen-based reconstructions, during the LGM and potentially during subsequent stadials marked by glacier readvances, assuming the same atmospheric phenomena took place.

4.2.2 Surface temperatures of the Moon recorded in lunar sample 76535

In the second application, we use observations of cosmogenic neon isotopes in grains of the plagioclase feldspar anorthite from lunar sample 76535 to constrain the thermal history of the sample during its exposure to cosmic ray particles at the lunar surface. Sample 76535 is a clast of troctolite, a mafic intrusive rock comprised of $\sim 35\%$ olivine, $\sim 60\%$ plagioclase, and $\sim 5\%$ orthopyroxene [181, 182], that cooled slowly at 30–50 km depth in the lunar crust [183]. Sample 76535 is the oldest Apollo sample, with ages of 4.2–4.3 Ga from the U/Pb, Th/Pb, Sm/Nd, $^{40}\text{Ar}/^{39}\text{Ar}$, and fission track chronometers [126, 184–190], that is unbrecciated and has no textural evidence for shock due to impact events. Because of its age and the absence of shock evidence, 76535 has been utilized in paleomagnetic studies to assess the presence and intensity of an early lunar magnetic field, which have implications for the early thermal evolution of the Moon and the mechanisms by which a lunar dynamo may have been generated [126, 189].

Interpreting the paleomagnetic record in 76535 to have formed at ~ 4.25 Ga in the presence of a lunar magnetic field and not due to brief fields created during impact events relies upon a detailed understanding of the thermal history of the sample, as at elevated temperatures the minerals carrying the magnetic signal can be ‘unblocked,’ meaning that their magnetic signal is reset. Detailed studies of the radiogenic ^{40}Ar and cosmogenic ^{38}Ar systematics in subsamples of 76535 place the firmest constraints on its thermal evolution [126, 189]. The most recent and most precise step degassing measurements on neutron irradiated aliquots of 76535 indicate almost no loss of radiogenic ^{40}Ar or cosmogenic ^{38}Ar , as evidenced by essentially constant apparent ages for all heating steps as a function of cumulative ^{39}Ar or ^{37}Ar (two isotopes generated uniformly by neutron irradiation) [126]. No diffusive loss of radiogenic or cosmogenic argon from 76535 contrasts with the argon systematics in many other Apollo samples that have been studied, which exhibit partial resetting either due to impact events or insolation of the lunar surface [e.g. 33, 125]. Using the diffusion kinetics of argon determined in the same aliquots of 76535, models of production and diffusion of radiogenic ^{40}Ar indicate that a heating due to an impact event at ~ 142 Ma that likely brought 76535 to the lunar surface could not have heated the sample above 400 °C. Because 76535 is more retentive to argon than some other lunar samples [e.g. 125], production and diffusion modeling of cosmogenic ^{38}Ar only places an upper bound on the temperatures experienced during exposure to cosmic rays to < 170 °C [126], which is significantly greater than typical

effective diffusion temperatures (EDTs) at the Moon’s surface of 70–80 °C [e.g. 125].

Given that ^{38}Ar is stable, it is hypothetically possible that the total 142 Ma exposure duration determined from cosmogenic ^{38}Ar measurements represents more than one exposure interval. More than one exposure interval implies burial interval(s) associated with impact event(s), during which temperatures of 76535 could have exceeded EDTs at the lunar surface but not exceeded 170 °C. While such temperatures are well below the blocking temperatures of the magnetic carrier minerals in 76535 [191] and thus not relevant to the fidelity of its paleomagnetic record, observations of a cosmogenic isotope sensitive to lunar surface temperatures could (1) corroborate the temperature constraints of the ^{38}Ar observations, and (2) demonstrate that only heating due to solar radiation affected 76535 since its initial exposure to cosmic ray particles. Here, we demonstrate that neon in anorthite from 76535 experiences open system behavior (i.e., simultaneous production and diffusion) at lunar surface conditions and make observations of cosmogenic neon in anorthite grains to test the assumption that this sample has only experienced heating due to insolation in the last 142 Ma.

4.3 Methods

The methods for cosmogenic noble gas paleothermometry with helium in quartz, as is the case for the Maritime Alps application, and with neon in feldspars, as is the case for the lunar application, are in many ways comparable to one another. In both applications, we determine sample-specific diffusion kinetics for the diffusant–mineral pair of interest by conducting step degassing experiments on irradiated single mineral grains, and we measure cosmogenic noble gas isotope abundances in multiple aliquots of each sample. Because we do not measure the noble gas diffusion kinetics and cosmogenic abundances in the same aliquot of sample, we must scale the diffusion lengthscale relevant to the step degassing experiment to the diffusion lengthscale appropriate for the cosmogenic abundance measurements. In the case of lunar sample 76535, scaling the diffusion kinetics is relatively straightforward because cosmogenic neon concentrations are so high that they can be measured on single anorthite grains, for which the diffusion lengthscale is readily estimated. The very high concentrations of cosmogenic neon are due to the lack of a lunar atmosphere, which makes *in situ* cosmogenic nuclide production rates substantially higher than those on Earth for a given nuclide–mineral pair [e.g. 192], and the long, 142 Ma exposure duration of 76535 to cosmic ray particles at the lunar surface. In contrast, the exposure durations of the Gesso Valley samples are four orders of magnitude smaller than that of 76535; as a consequence, cosmogenic ^3He abundances in quartz from the Gesso Valley samples must be measured from many hundreds to thousands of quartz grains at once. The need to analyze large aliquots of material for Earth-based applications requires that we quantify the variance in the size of quartz grains we analyze for cosmogenic ^3He , which introduces an additional uncertainty when reconstructing temperatures based on these observations. With properly scaled diffusion kinetics and observed cosmogenic abundances for each application, we forward model

production and diffusion over the known exposure duration and compare the observed cosmogenic ^3He or neon retention to that calculated for different temperature scenarios.

Below, we describe the details of the irradiations, noble gas measurements, and diffusion lengthscale analyses specific to each application of cosmogenic noble gas paleothermometry.

4.3.1 Helium measurements in quartz from Gesso Valley moraine boulders

Of the Gesso Valley samples for which ^{10}Be measurements exist, we obtained archived material (either whole rock or crushed, sieved fractions) from five samples for cosmogenic ^3He measurements: one from the Piano del Praiet moraine (PDP10), two from the Ponte Murato moraine (PM1, and PM4), and two from the Tetti del Bandito moraine (TDB1 and TDB3; Fig. 4.1 and Table 4.1). We obtained a seventh sample, PDP-11, for which there are no existing ^{10}Be measurements. However, probative measurements of neon isotope abundances in PDP-10 and PDP-11 indicated that PDP-11 has a substantial inherited cosmogenic nuclide inventory (i.e., prolonged exposure to cosmic rays before being deposited atop the Piano del Praiet moraine) and will therefore not be discussed further. We separated quartz from other phases using standard crushing, sieving, and magnetic methods, followed by a ‘frothing’ technique commonly used in the ceramics industry to separate quartz from feldspars in the largest sieve fraction that lacked composite grains [193]. Purified quartz was then used to both measure cosmogenic ^3He abundances and determine sample-specific ^3He diffusion kinetics. All helium isotope measurements were made with an MAP 215-50 sector field mass spectrometer in the BGC Noble Gas Thermochronometry Lab. Gas purification techniques and mass spectrometer analyses are as described in Tremblay et al. [87].

Table 4.1: Locations and sample information for moraine boulders previously dated in the Gesso Valley with cosmogenic ^{10}Be , originally reported in Federici et al. [164, 165].

Sample	Latitude (decimal degrees)	Longitude (decimal degrees)	Elevation (m)	Sample thickness (cm)	Shielding factor
PDP10	44.421534	7.819950	1806	3.0	0.9200
PM1	44.252667	7.385500	860	3.0	0.9653
PM4	44.252667	7.385500	860	3.0	0.9653
TDB1	44.289712	7.432528	770	3.0	0.9825
TDB3	44.289712	7.432528	770	3.0	0.9819

For cosmogenic ^3He measurements, 100–500 mg aliquots of quartz were weighed and packed into tantalum metal cups with both ends crimped, placed under vacuum in a sample chamber, and heated with a feedback-controlled 150 W diode laser to either 500, 800, or 1100 °C for 15 minutes until subsequent extractions yielded He signals indistinguishable from the

instrumental detection limit. Empty tantalum cup blanks, heated to the same temperatures as the samples, and room temperature procedural blanks were measured throughout each analytical session and subtracted from the sample measurements; ^3He blank corrections were typically $2\text{--}3 \times 10^4$ atoms, corresponding to blank correction magnitudes on the order of 3–11%. Aliquots of air and ^3He -spiked helium standards of different manometrically-calibrated pipette volumes were analyzed throughout an instrumental tuning period used to determine helium sensitivities; sensitivities varied linearly over the pressure range of the sample analyses, approximated by the size of the ^4He signal. We propagated uncertainties from the blank corrections and sensitivity regression into the cosmogenic ^3He concentrations. We assume that all ^3He is cosmogenic.

To determine sample-specific diffusion kinetics, we conducted stepwise degassing experiments on a proton-irradiated quartz grain from each sample. Proton irradiation generates a uniform distribution of ^3He in quartz through similar nuclear reactions to those induced by cosmic ray particles but with ten orders of magnitude or higher production rates, enabling step degassing diffusion experiments to be conducted on single irradiated quartz grains [22, 87, 88]. Quartz aliquots were irradiated with a 228.5 MeV proton beam for 6 hours at the Francis H. Burr Proton Therapy Center at the Massachusetts General Hospital in December 2015; the total proton fluence of this irradiation was 9.14×10^{15} p/cm². The irradiation target design and setup are detailed in Tremblay et al. [144]. Proton irradiated quartz aliquots were examined with a binocular microscope, and single crystals lacking penetrative fractures and visible inclusions (fluid or mineral) were selected for stepwise degassing. The dimensions of the chosen grains were measured to estimate the spherical equivalent radius used in later calculations to scale the diffusion lengthscale. Details of the stepwise degassing setup and helium measurements are detailed in Tremblay et al. [87].

In addition to determining the spherical equivalent radius of the quartz grains used in diffusion experiments, we also determined the spherical equivalent radii of the quartz grains used for cosmogenic measurements and assessed whether these radii are representative of the quartz size distribution in whole rock. Such an assessment is important because if we significantly reduced the grain size of quartz during the crushing process, this could lead to both an underestimation of the diffusion lengthscale to which the diffusion experiment size is scaled and missing cosmogenic ^3He from our measurements. First, we photographed and measured the dimensions of at least 100 quartz grains from the sieve fraction of each sample used for cosmogenic ^3He measurements. We determined major, intermediate, and minor axes of best fitting ellipsoids using the software ImageJ [194] and calculated the radius of a sphere with the same surface area to volume ratio for each grain. We compared the spherical equivalent radii calculated using this approach to spherical equivalent radii determined from micro x-ray computed tomography (CT) analyses on a smaller number of grains from the same samples, wherein the grains were mapped in three dimensions with a resolution better than 5 μm . CT scans were obtained on the Xradia MicroXCT scanner at the University of Texas at Austin High-Resolution X-ray CT Facility and processed using the software Blob3D [148] as described in Tremblay et al. [144]. This comparison demonstrates that the ellipsoid approach consistently overestimates the spherical equivalent radius by $\sim 50\%$ likely because

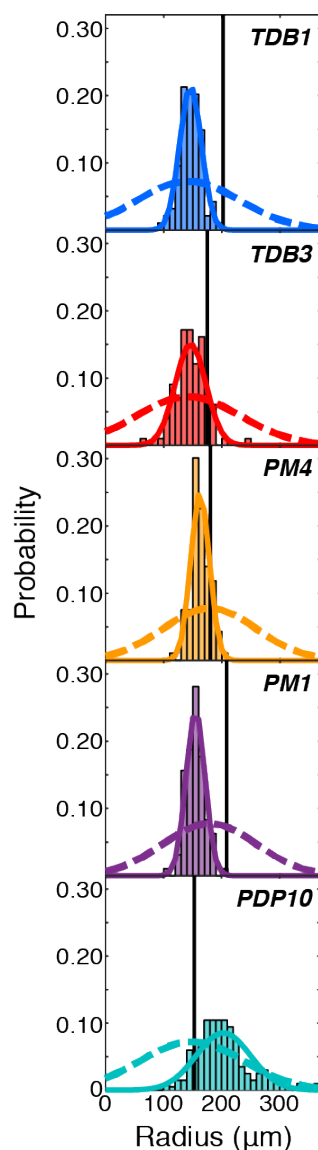


Figure 4.2: Grain size analysis for Gesso Valley samples. Histograms and solid curves denote the distribution of spherical equivalent radii for representative quartz grains (≥ 100) from the sieve fraction analyzed for cosmogenic ^3He abundances. Dashed curves denote the distribution of spherical equivalent radii in whole rock, inverted from the distribution of sectional circles (≥ 100) of quartz grains measured in thin section. Thin sections were made from the same sample as the crushed fraction, in the case of PDP10, or from a resampled boulder on the same moraine, in all other cases. Vertical black lines denote the spherical equivalent radius of the single quartz grain analyzed in each diffusion experiment shown in Fig. 4.4.

the ellipsoid method significantly underestimates the surface area of grains. We therefore scaled the spherical equivalent radii from loose grain measurements by a factor 1.5; the distribution of grain sizes from these measurements are shown in Fig. 4.2. Also shown in Fig. 4.2 is the probability distribution of spherical equivalent radii of quartz grains in whole rock. To determine this distribution, we calculated circular equivalent radii from measured sectional areas of at least 100 quartz grains in thin sections, and inverted the distribution of circular equivalent radii to a distribution of spherical equivalent radii using the code STRIPSTAR and the methodology described by Heilbronner and Barrett [195]. For PDP10, the thin section was made from the same sample as the sample crushed for cosmogenic ^3He measurements. For the PM and TDB moraines, no whole rock material from the original samples was preserved; we therefore collected additional material from boulders exposed atop each of these moraines for thin sections, and assume that the grain size observed in these samples is representative of the samples for which we have cosmogenic ^3He data.

For all samples, the distribution of spherical equivalent radii for the sieve fraction has a smaller standard deviation than the radii determined from thin section measurements (Fig. 4.2), which is not surprising given that the sieving process removes grains larger and smaller than the sieve size. With the exception of the PM samples, we find that the mean spherical equivalent radius of quartz in the sieve fraction is equal to or slightly greater than the mean radius determined from thin section measurements (Fig. 4.2). The mean quartz radius in the sieve fraction from the PM samples is only slightly smaller than the mean radius from thin section measurements, and the two distributions show significant overlap. Given the good agreement between mean spherical equivalent radii for the sieve fraction and thin section quartz, we assume that the grain size has not been substantially reduced by sample crushing and use the mean and standard deviation of the sieve fraction radii distributions as the appropriate diffusion lengthscale for modeling the diffusion of cosmogenic ^3He in each sample.

4.3.2 Neon measurements in 76535 anorthite

To quantify neon diffusion kinetics in anorthite from 76535, we conducted a step degassing experiment on a neutron irradiated grain of anorthite. Small aliquots of 76535 were neutron irradiated for 50 hours at the University of Oregon TRIGA reactor in the Cadmium-Lined In-Core Irradiation Tube (CLICIT) facility. The choice of neutron irradiation over proton irradiation was primarily a practical one, as neutron irradiation was necessary for the argon measurements presented in Garrick-Bethell et al. [126] and generates high, uniform concentrations of ^{21}Ne and ^{22}Ne like proton irradiation, albeit through different nuclear reactions. From the irradiated aliquot, we isolated a single, intact grain of anorthite (76535 sample material is friable and readily disaggregated into single component grains). The anorthite grain, which has a spherically equivalent radius of $296\ \mu\text{m}$ determined from microscope measurements, was heated over 97 consecutive heating steps, including three retrograde heating cycles, to temperatures between 100 and $1050\ ^\circ\text{C}$ and lasting between 0.5 and 10 hours using a feedback-controlled laser heating system (Table S5 in [126]). We used the gas purifi-

cation and mass spectrometric measurement techniques described in Tremblay et al. [87]. Thirteen room temperature procedural blanks measured over the course of the experiment were subtracted from the measurement time zero intercepts; average blank corrections were 0.05×10^6 atoms for ^{21}Ne and 1.5×10^6 atoms for ^{22}Ne . The MAP-215 sector field mass spectrometer in the BGC Noble Gas Thermochronometry Lab used to conduct these measurements cannot resolve $^{22}\text{Ne}+$ from $^{44}\text{CO}_2++$. However, we found that the $\text{CO}_2+/\text{CO}_2++$ was constant over the H_2 partial pressure range in the stepwise degassing experiment, and that the average signals on $m/e = 44$ for room-temperature blanks and heating steps are equal. Therefore we accounted for the $^{44}\text{CO}_2++$ interference in the blank correction described above. No isobaric interference corrections were necessary for ^{21}Ne . Aliquots of a manometrically-calibrated air standard were also analyzed after approximately every fifth heating step to determine neon sensitivities of the mass spectrometer, which we found to be constant over the pressure range of the analyses.

For the cosmogenic neon measurements, we measured ^{20}Ne , ^{21}Ne , and ^{22}Ne in five unirradiated anorthite grains using the same feedback-controlled laser system. During these measurements, we corrected for interferences on ^{22}Ne from $^{44}\text{CO}_2++$ and ^{20}Ne from $^{40}\text{Ar}++$ by introducing a ^{39}Ar spike during neon analyses as described by Balco and Shuster [78]. Like the step degassing experiment, room temperature procedural blanks and aliquots of the manometrically-calibrated air standard were measured throughout the analytical session. Prior to the neon analyses, each anorthite grain was precisely weighed. The mass of each sample, combined with the compositionally-determined density of 76535 anorthite, was used to estimate the volume of each grain and, assuming a spherical geometry, each grain's radius. These spherical equivalent radii were then used to scale the diffusion experiment results in forward models of production and diffusion.

4.4 Results and Discussion

Although the methods for applying cosmogenic noble gas paleothermometry to questions about paleoclimate on Earth and past surface temperatures on the Moon are quite similar, below we describe how the results of applying this new technique in terms of the temperatures that we reconstruct can be dramatically different. While for the Maritime Alps we reconstruct temperatures since the LGM that range between 5 and 25 °C, on the Moon we estimate effective diffusion temperatures (EDTs) between 70 and 80 °C, which reflects the large temperature variations characterizing a planetary body without an atmosphere. The magnitude of the temperatures, and more importantly the temperature variations, we are interested reconstructing for each application directly affects our ability to interpret each dataset. In the case of the Moon, uncertainties in the assumptions we make to reconstruct temperatures from cosmogenic neon observations in anorthite have little effect on our interpretation that 76535 has only experienced solar radiative heating while at the lunar surface for the last 142 Ma. Conversely, for the Maritime Alps there are a number of sources of uncertainty in our temperature reconstruction from ^3He in quartz that, at this point, limit

our ability to quantify of past climate variations since the LGM.

4.4.1 Cosmogenic ^3He retention in quartz and temperature reconstruction from Gesso Valley moraine boulders

We report measured abundances of cosmogenic ^3He in quartz aliquots from each of the Gesso Valley samples in Table 4.2. We used version 3 (v3) of the online exposure age calculator code, a more recent version of the code published in Balco et al. [54] that implements the cosmogenic ^3He production rate in quartz determined by Vermeesch et al. [53], to calculate an apparent exposure age from the measured ^3He abundance in each aliquot. We assume that the erosion rate is negligible for all boulders sampled, as was assumed in the original publications reporting ^{10}Be exposure ages from these boulders [164, 165]. Sample coordinates, elevations, thicknesses, and shielding correction factors used in exposure age calculations are reported in Table 4.1. In Table 4.3, we report the weighted mean apparent ^3He exposure age for each sample determined using the scaling scheme of Stone [69]. We also recalculated the ^{10}Be exposure ages, normalizing the ^{10}Be concentrations to the isotope ratio standards of Nishiizumi et al. [71], using v3 of the online exposure calculator and the global ^{10}Be production rate calibration dataset, and assuming the scaling scheme of Stone [69] (Table 4.2). We divided the weighted mean apparent ^3He exposure ages by the ^{10}Be exposure ages to calculate ^3He retention, which represents the fraction of cosmogenic ^3He produced during surface exposure that remains in the quartz analyzed [68].

Fig. 4.3 shows ^3He retention as a function of exposure duration in the five samples we analyzed. All Gesso Valley samples retain less than 50% of the cosmogenic ^3He that was produced during their exposure (Table 4.3, Fig. 4.3). Retention generally decreases with increasing exposure duration: quartz from PDP10, sampled from the youngest and highest elevation moraine, retains 46% of its cosmogenic ^3He , while quartz from TDB1, sampled from the lowest elevation moraine correlated to the LGM, retains only 6% of its cosmogenic ^3He . Samples PM1 and PM4, both from the Ponte Murato moraine, have ^{10}Be exposure ages that agree within uncertainty but significantly different ^3He retention (Table 4.3, Fig. 4.3). Similarly, the ^{10}Be exposure ages for the two Tetti del Bandito moraine samples, TDB1 and TDB3, are in agreement, but the ^3He retentions in these two samples are drastically different (Table 4.3, Fig. 4.3).

In order to reconstruct temperatures from the observed ^3He retention in each quartz sample and assess the differences in ^3He retention between samples from the same moraine, we need to know the diffusion kinetics of ^3He in each sample. Fig. 4.4 shows the results of step degassing experiments on proton-irradiated quartz from the Gesso Valley samples in Arrhenius plots where the natural log of diffusivity, calculated from the cumulative fraction of gas released during each heating step [82], is plotted as a function of inverse temperature (gray circles).

All Gesso Valley quartz samples exhibit some degree of nonlinearity in the Arrhenius plots (Fig. 4.4). While we do not have a mechanistic explanation or model for this type of

Table 4.2: Observations of cosmogenic ^3He in Gesso Valley quartz samples.

Sample, aliquot	Mass of quartz analyzed (g)	$[^3\text{He}]$ (10^3 atoms/g)
PDP10-1	0.109	2.20 ± 0.38
PDP10-2	0.101	2.38 ± 0.37
PDP10-3	0.102	3.65 ± 0.35
PDP10-4	0.126	2.91 ± 0.26
PDP10-5	0.121	2.99 ± 0.39
PDP10-6	0.136	2.99 ± 0.31
PDP10-7	0.117	3.12 ± 0.37
PDP10-8	0.125	2.44 ± 0.35
PM1-1	0.101	1.14 ± 0.42
PM1-2	0.101	0.89 ± 0.60
PM1-3	0.304	1.11 ± 0.18
PM1-4	0.266	0.88 ± 0.15
PM1-5	0.290	1.05 ± 0.15
PM4-1	0.113	1.29 ± 0.34
PM4-2	0.309	1.51 ± 0.17
PM4-3	0.268	1.63 ± 0.19
PM4-4	0.247	1.60 ± 0.12
TDB1-1	0.216	0.62 ± 0.28
TDB1-2	0.269	0.11 ± 0.14
TDB1-3	0.306	0.28 ± 0.13
TDB1-4	0.292	0.26 ± 0.13
TDB1-5	0.482	0.36 ± 0.08
TDB3-1	0.216	1.38 ± 0.27
TDB3-2	0.124	1.35 ± 0.39
TDB3-3	0.279	1.20 ± 0.19
TDB3-4	0.301	1.31 ± 0.27
TDB3-5	0.268	1.32 ± 0.18

Table 4.3: Apparent ^3He exposure ages and retention in Gesso Valley quartz samples. See text for details about the input parameters to the exposure age calculation. We report external uncertainties for both ^3He and ^{10}Be exposure ages.

Sample	Apparent exposure age (yr), ^3He	Exposure age (yr), ^{10}Be	^3He retention
PDP10	6402 ± 341	14071 ± 1220	0.46 ± 0.05
PM1	4534 ± 452	16356 ± 1601	0.28 ± 0.04
PM4	7006 ± 512	19213 ± 1654	0.36 ± 0.04
TDB1	1407 ± 271	23397 ± 2072	0.06 ± 0.01
TDB3	6187 ± 561	21003 ± 1854	0.29 ± 0.04

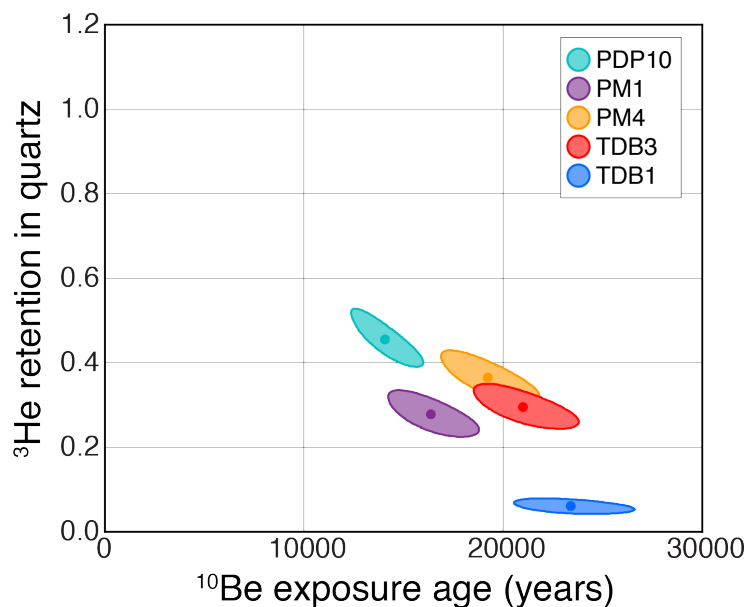


Figure 4.3: Cosmogenic ^3He retention as a function of ^{10}Be exposure age in quartz from Gesso Valley moraine samples. Ellipses represent 1σ uncertainty.

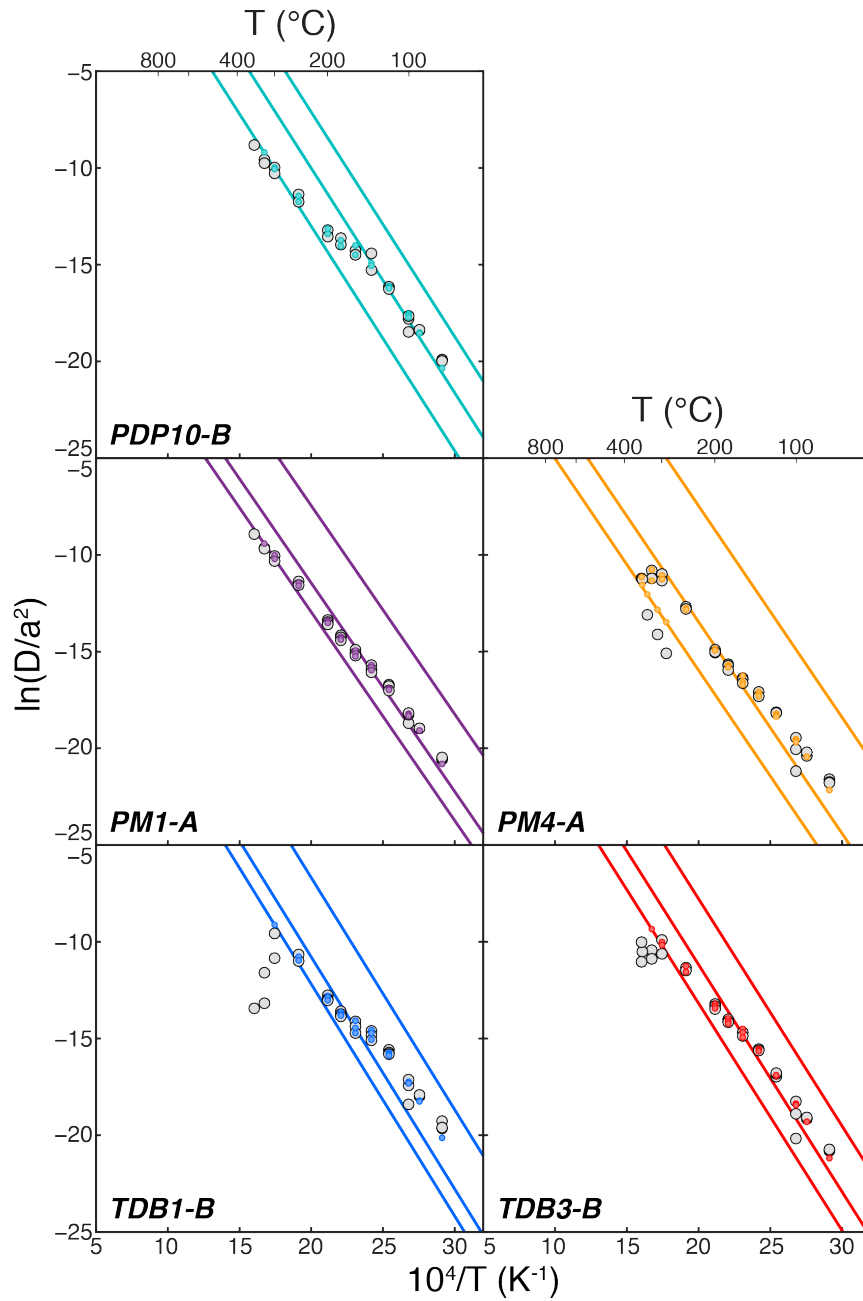


Figure 4.4: Arrhenius plots for helium diffusion experiments on Gesso Valley quartz samples. D/a^2 values are normalized to s^{-1} . Experimental data are plotted as gray circles. Diffusivities were calculated using the equations of Fechtig and Kalbitzer [82] and the uncertainty propagation outlined in Tremblay et al. [87]. Color circles and lines denote three-domain multiple diffusion domain (MDD) models that minimize misfit with the experimental data. Tremblay et al. [144] describe MDD modeling approach used here.

complex diffusion behavior [87], multiple diffusion domain (MDD) models [113, 134, 135] can reproduce the nonlinearity observed in laboratory degassing experiments and appear to be relevant to ^3He diffusive loss over 10^3 – 10^4 year timescales, as demonstrated for a geologic case study for which the temperatures during surface exposure are reasonably well known [87]. We constructed MDD models optimized to fit each of the helium step degassing experiments on Gesso Valley quartz samples following the approach outlined in Tremblay et al. [144]. Fig. 4.5 shows the misfit between the calculated diffusivities from MDD models and the experimentally-determined diffusivities as a function of number of diffusion domains, where the misfit statistic was calculated using Eq. 3.2 in Chapter 3. The misfit shown for a given number of diffusion domains is the minimum misfit found after searching over a large range of model parameters (activation energy E_a , pre-exponential factor(s) D_0/a^2 , and gas fractions).

We found that, for all five step degassing experiments, increasing the number of diffusion domains from 1 to 2 and from 2 to 3 significantly reduced the misfit between the observed diffusivities and those calculated with the MDD model (Fig. 4.5). However, increasing the number of diffusion domains from 3 to 4 did not significantly reduce the misfit between the observed and calculated diffusivities (Fig. 4.5). For experiment PM1-A, attempts at constructing a four domain model yielded two domains with the same pre-exponential factor and thus are the equivalent of the three domain model. Therefore for all experiments we use the diffusion parameters corresponding to the optimized three domain model. Lines corresponding to the diffusion parameters of the three domains, as well as the calculated diffusivities for the three domain models, are shown in color over the experimentally determined diffusivities in Fig. 4.4. The activation energies, pre-exponential factors, gas fractions, and misfit statistic for these three domain models are reported in Table 4.4.

As discussed in Section 4.3, we need to scale the diffusion kinetics determined from the step degassing experiments to the diffusion lengthscale appropriate for the cosmogenic ^3He abundance measurements. In constructing MDD models, we cannot independently parameterize the diffusivity at infinite temperature, D_0 , and the diffusion lengthscale, a . Instead, we model them together as the natural logarithm of the pre-exponential factor in the Arrhenius expression, $\ln(D_0/a^2)$, which in an Arrhenius plot corresponds to the y-intercept. Because we cannot independently model the diffusion lengthscale a , we must make an assumption about how to scale the MDD models appropriately. This is not a problem in the $^{40}\text{Ar}/^{39}\text{Ar}$ thermochronometry community in which MDD models were developed, because in almost all cases argon diffusion kinetics and naturally-occurring argon isotope abundances are measured in the same mineral grain [e.g. 114]. Here, we assume that the diffusion lengthscale of all domains, and by inference all the pre-exponential factors in a given MDD model, scales with the spherical equivalent radius of the quartz grain analyzed. Theoretically, this implies that diffusion lengthscale of the most retentive domain (the domain with the lowest $\ln(D_0/a^2)$ or intercept in Arrhenius space) is the spherical equivalent radius of the grain analyzed. Practically, this scaling is accomplished as follows:

$$\left(\frac{D_0}{a^2}\right)_{scaled} = \left(\frac{D_0}{a^2}\right)_{MDD} \left(\frac{a_{sde}^2}{a_{cosmo}^2}\right) \quad (4.1)$$

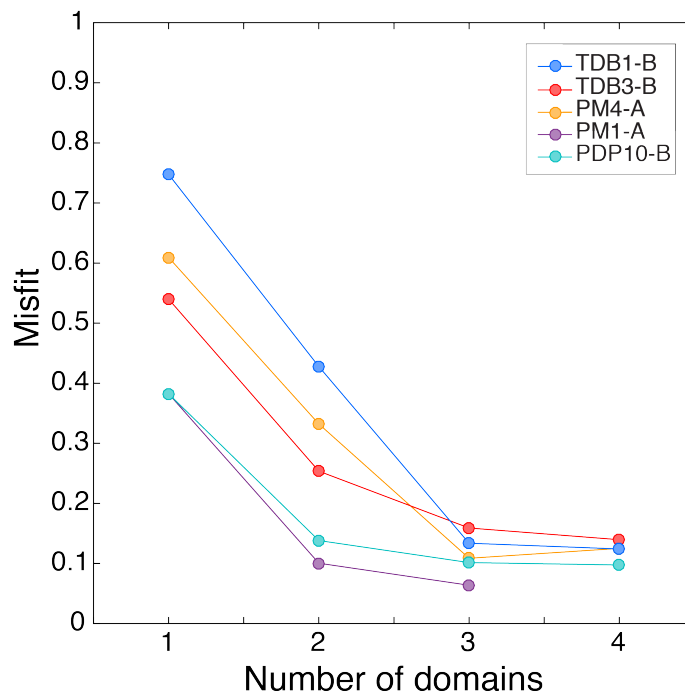


Figure 4.5: Minimized misfit between observed and MDD-modeled ^3He diffusivities as a function of number of diffusion domains for Gesso Valley quartz samples.

Table 4.4: Three domain multiple diffusion domain model parameters for ^3He diffusion experiments in Gesso Valley quartz samples.

Experiment	Domain	E_a (kJ/mol)	$\ln(D_0/a^2)$	fraction	Misfit
PDP10-B	1	96.5	10.2	0.61	0.097
	2		16.1	0.21	
	3		13.2	0.18	
PM1-A	1	89.6	8.6	0.54	0.067
	2		10.1	0.36	
	3		14.1	0.10	
PM4-A	1	90.9	8.4	0.74	0.109
	2		5.9	0.20	
	3		14.4	0.06	
TDB1-B	1	99.7	11.8	0.46	0.161
	2		13.2	0.30	
	3		17.3	0.24	
TDB3-B	1	97.6	10.3	0.42	0.149
	2		12.3	0.41	
	3		15.7	0.17	

where a_{sde} is the spherical equivalent radius of the step degassing experiment quartz grain and a_{cosmo} is the spherical equivalent radius of the quartz grains used for the cosmogenic ^3He measurements (Fig. 4.2).

With the scaled, sample-specific diffusion kinetics, we explore possible temperature scenarios to explain the observed cosmogenic ^3He abundances in the Gesso Valley samples. To do this, we use forward models of simultaneous production and diffusion to model how cosmogenic ^3He retention evolves as a function of exposure duration under different temperature scenarios. We begin with the simplest possible scenario of constant temperature over time, as this allows us to assess the effective diffusion temperature (EDT) integrated over the exposure duration of each sample (hereafter referred to as the integrated EDT). Fig. 4.6 shows the evolution of ^3He retention as a function of exposure duration for constant temperature scenarios in 2 °C increments from 0 °C to 30 °C. These retention evolution curves differ for each Gesso Valley quartz sample for several reasons: (1) each sample has a different set of diffusion kinetics, assuming a three domain diffusion model (Fig. 4.4, Table 4.4), (2) these sample specific diffusion kinetics are scaled to different spherical equivalent radii based on the measured grain size distributions of quartz in the sieve fraction used for cosmogenic ^3He measurements (Fig. 4.2), and (3) the cosmogenic ^3He production rate in quartz differs between samples. In each panel of Fig. 4.6 we report the integrated EDT that agrees with the observed cosmogenic ^3He retention in each quartz sample. We provide two uncertainty estimates on this integrated EDT. One σ EDT uncertainties in parentheses account for the uncertainty in ^3He retention and exposure duration as determined from ^{10}Be measurements; the second set of uncertainties also account for uncertainty in the spherical equivalent radius to which the experimentally-determined diffusion kinetics are scaled.

The most readily observable feature of the models in Fig. 4.6 is that the integrated EDT calculated for each quartz sample is different. This is in part expected because the different moraines represented by these samples are located at different elevations in the Gesso Valley and thus will experience different temperatures at any point in time due to the atmospheric lapse rate. This may also in part be due to the samples having different exposure durations; for example, a change in temperature between the deposition of the TDB moraine and the PM moraine would only be reflected in the cosmogenic ^3He retention and integrated EDT of the TDB moraine samples. Differences in integrated EDT between samples from the same moraine, on the other hand, are unexpected. For PM1 we calculate an integrated EDT of 7.6 °C, while for PM4 we calculate a much higher integrated EDT of 19.7 °C. Similarly, for TDB1 we calculate an integrated EDT of 24.5 °C, while for TDB3 we calculate a much lower integrated EDT of 15.8 °C.

To put these integrated EDTs into context, in Fig. 4.7 we use modern daily temperature records from 2002 to 2016 to calculate mean temperatures (solid lines) and EDTs (dashed lines) at the elevation of each moraine. We obtained temperature records at the elevation of each moraine by scaling daily mean, minimum, and maximum temperature data from two meteorological stations within the Gesso Valley: Diga della Piastra (44.227 °E, 7.389 °N, 959 m) and Diga del Chiotas (44.168 °E, 7.334 °N, 1980 m). These data are publicly available through the Environmental Protection Agency for the Piemonte Region

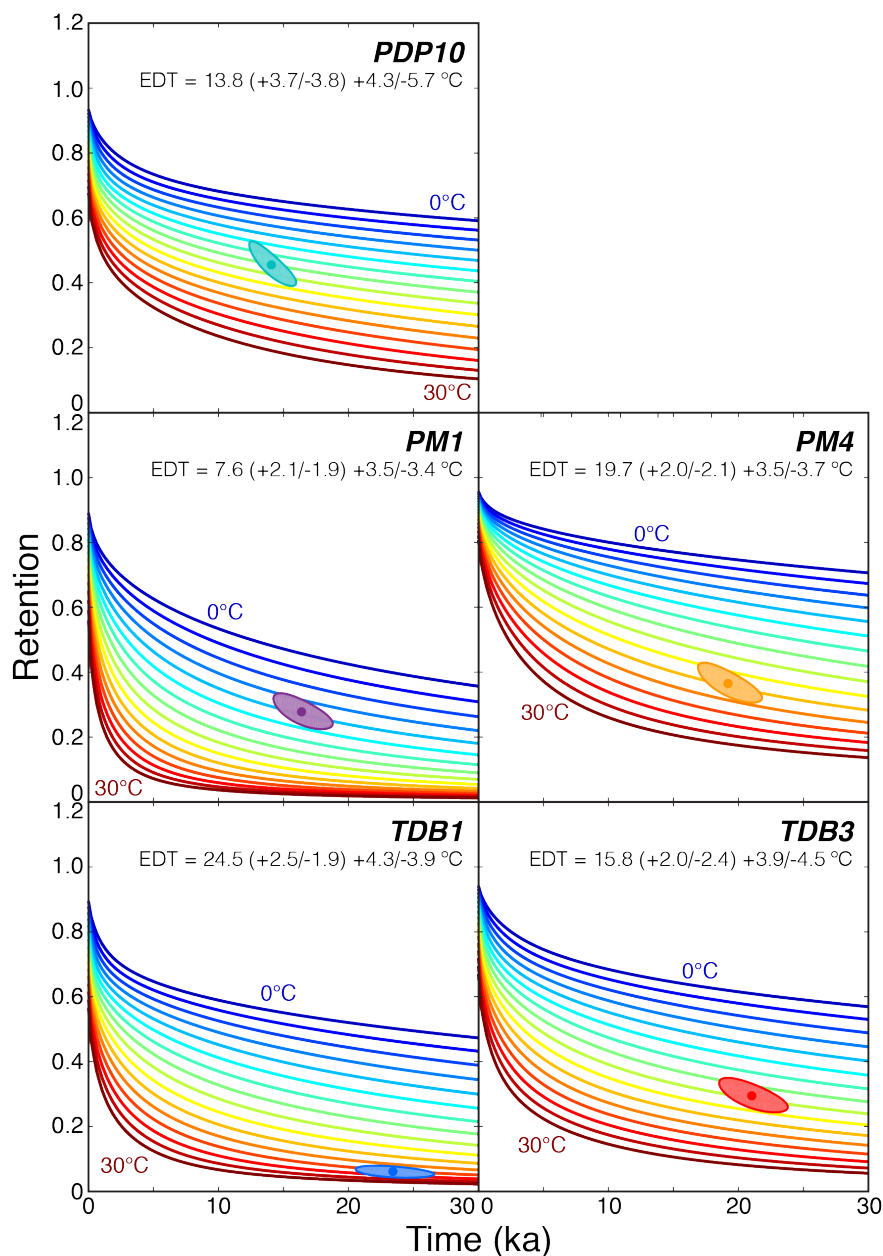


Figure 4.6: EDTs integrated over the exposure duration of Gesso Valley moraine samples. For each sample, we plot cosmogenic ^3He retention as a function of exposure duration assuming a constant EDT and the MDD model diffusion kinetics reported in Table 4.3. Observed cosmogenic ^3He retention ellipses are plotted as in Fig. 4.4 for comparison. One σ EDT uncertainties in parentheses account for the uncertainty in ^3He retention and exposure duration as determined from ^{10}Be measurements; the second set of uncertainties also account for uncertainty in the spherical equivalent radius to which the experimentally-determined diffusion kinetics are scaled.

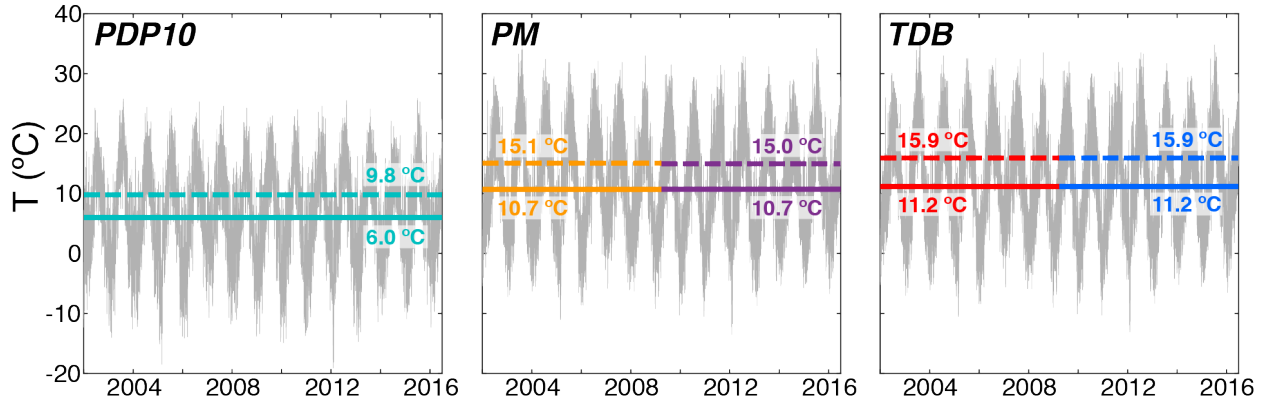


Figure 4.7: EDTs calculated from modern meteorological data. In gray we show the time series of mean, minimum, and maximum temperatures from 2002 to mid-2016 at the elevations of the PDP, PM, and TDB moraines, scaled from the nearest two meteorological stations using average monthly lapse rates. Solid color lines denote the mean temperature for each time series; dashed color lines denote the EDT for each time series calculated using the activation energies of the best fit MDD models in Fig. 4.4 and Table 4.4. Colors for specific samples are the same as in Figs. 4.3–4.6.

(arpa.piemonte.gove.it). We scaled the temperature data at Diga della Piastra to the elevation of the TDB and PM moraines and the temperature data at Diga del Chiotas to the elevation of the PDP moraine using monthly average lapse rates determined from the same dataset. For PDP10, PM4, and TDB1, the modern EDT estimate (9.8, 15.1, and 15.9 °C) is several degrees lower than the EDT integrated over each sample’s exposure duration (13.8, 19.7, and 24.5 °C). In contrast, the modern EDT estimate for TDB3 (15.9 °C) is comparable to the EDT integrated over its exposure duration (15.8 °C), and for PM1 the modern EDT estimate (15.0 °C) is several degrees higher (vs. 7.6 °C).

In addition to comparing the integrated EDTs calculated from observed cosmogenic ^3He abundances to modern day EDTs in the Gesso Valley, we can compare our observations to temperatures from general circulation model (GCM) simulations and nearby temperature records from other proxy data. In Figs. 4.8–4.10, we show how cosmogenic ^3He retention would evolve as a function of exposure duration using seasonal temperature outputs from the TraCE-21ka transient simulation. TraCE-21ka uses the National Center for Atmospheric Research (NCAR) Community Climate System Model version 3 (CCSM3), a synchronously coupled atmosphere-ocean general circulation model (GCM) [196], to simulate the Earth’s climate from the LGM (22 thousand years ago) to the present [197, 198]. We obtained seasonal (DJF, MAM, JJA, and SON) mean and maximum temperatures from the TraCE-21ka simulation for the 44.3 °N, 7.4 °E grid cell including the Gesso Valley. These simulated temperatures were determined for a mean elevation above sea level for the grid cell, which changed through the simulation as simulated sea level changed. However, the elevation of

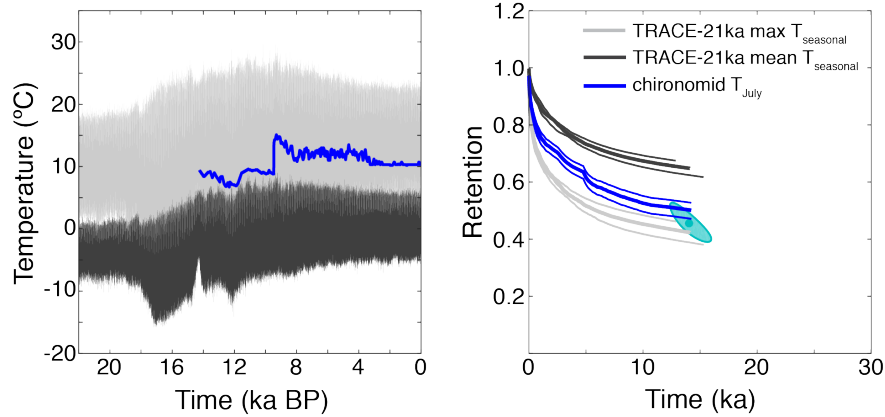


Figure 4.8: Cosmogenic ^3He retention calculated in PDP10 from scaled TraCE-21ka seasonal temperatures and spliced chironomid July temperatures. The left panel shows the mean and maximum seasonal temperature from the TraCE-21ka climate simulation and the mean July temperature from two spliced chironomid records, scaled to the elevation of PDP10 using modern lapse rate data. The right panel shows the evolution of ^3He retention with time assuming the TraCE-21ka and chironomid temperatures represent the EDT experience over PDP10’s exposure duration. Thick retention curves assume the mean exposure duration and grain size for diffusion kinetics scaling; lower thin retention curves assume the $+1\sigma$ exposure duration and grain size, while upper thin curves assume the -1σ exposure duration and grain size. The ellipse shows the observed retention and exposure duration, as in Fig. 4.3.

our sample sites with respect to sea level would have also changed through time, meaning that the relative offset between our sample site elevation and the mean grid cell elevation would have remained constant. We therefore scale the TraCE-21ka simulation temperatures to our sample sites using the present day difference between the sample site elevations and TraCE-21ka mean elevation assuming the modern seasonal lapse rate determined from the meteorological stations discussed above. The atmospheric lapse rate in the Gesso Valley likely changed between the LGM and the present, especially considering the fact that the valley was more extensively glaciated during part of this interval. Nonetheless, we assume the modern rate because (1) we have no independent means for assessing how different paleo-lapse rates may have been, and (2) any differences from the modern lapse rate when the valley was glaciated were likely $\leq 2\text{ }^\circ\text{C}/\text{km}$ [e.g. 169, 199, 200], which will not be resolvable using our cosmogenic noble gas observations that span $\leq 1\text{ km}$ in elevation [68]. For all Gesso Valley quartz samples, the observed cosmogenic ^3He retention is bracketed by the ^3He retention calculated assuming mean seasonal temperatures and the ^3He retention calculated assuming maximum seasonal temperatures scaled from the TraCE-21ka simulation. For PDP10 (Fig. 4.8), PM4 (Fig. 4.9), and TDB1 (Fig. 4.10), we calculate cosmogenic ^3He retention from the TraCE-21ka simulation maximum seasonal temperature that is in agreement within uncertainty with the observed retention in these samples. Cosmogenic

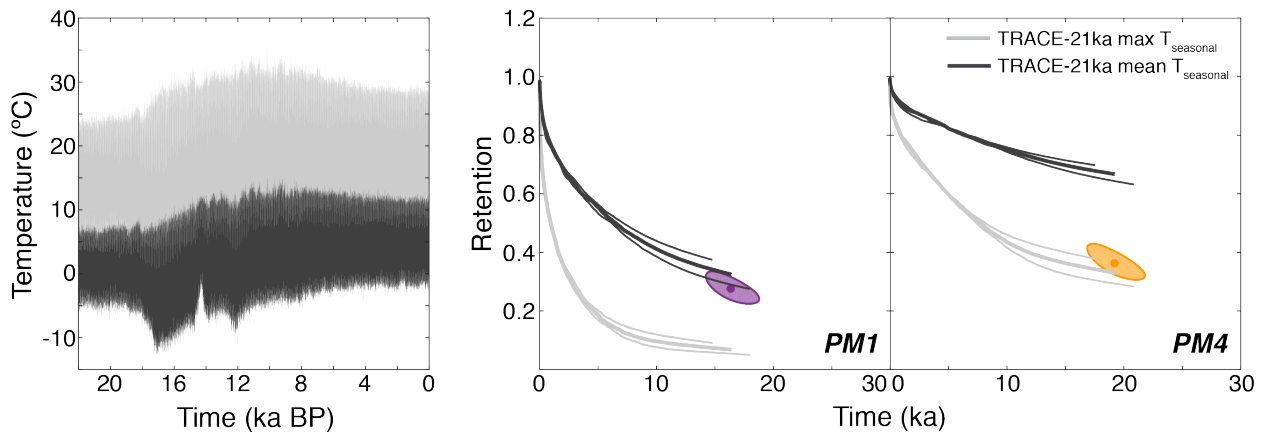


Figure 4.9: Cosmogenic ^3He retention calculated in PM1 and PM4 from scaled TraCE-21ka seasonal temperatures. The left panel shows the mean and maximum seasonal temperature from the TraCE-21ka climate simulation, scaled to the elevation of the PM moraine using modern lapse rate data. The right panels shows the evolution of ^3He retention with time assuming the TraCE-21ka temperatures represent the EDT experience over the PM samples' exposure duration. Thick and thin retention curves are as in Fig. 4.8. Ellipses show the observed retention and exposure duration, as in Fig. 4.3.

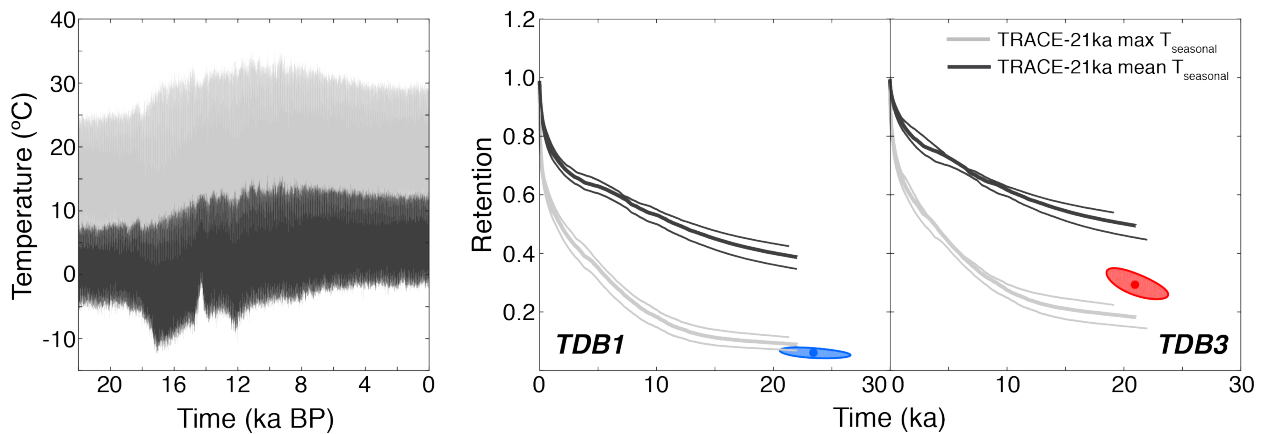


Figure 4.10: Cosmogenic ^3He retention calculated in TDB1 and TDB3 from scaled TraCE-21ka seasonal temperatures. The left panel shows the mean and maximum seasonal temperature from the TraCE-21ka climate simulation, scaled to the elevation of the TDB moraine using modern lapse rate data. The right panels shows the evolution of ^3He retention with time assuming the TraCE-21ka temperatures represent the EDT experience over the TDB samples' exposure duration. Thick and thin retention curves are as in Fig. 4.8. Ellipses show the observed retention and exposure duration, as in Fig. 4.3.

^3He retention calculated from the TraCE-21ka mean seasonal temperatures agrees with the observed cosmogenic ^3He retention in PM1 within uncertainty (Fig. 4.9).

PDP10, which has the youngest ^{10}Be exposure age of 14071 ± 1220 years, is the only sample for which proxy data with continuous, coeval coverage are readily compared. For this comparison, we spliced two chironomid-based July temperature reconstructions from locations close to the Maritime Alps. One record is from Lago de Piccolo di Avigliana, located in the Italian Alps ~ 25 km north of the Gesso Valley (45.05°N ; 7.38°E , 365 m), where the chironomid-based mean July temperature reconstruction covers 14200 to 9500 years ago [172]. The other record is from Schwarzsee ob Sölden, a high-alpine lake in the Austrian Alps (46.96583°N , 10.94611°E , 2796m), where the chironomid record extends from the present day back 10200 years [201]. Like the GCM simulation, we scaled the July temperature reconstructions from both locations to the elevation of PDP10 using modern lapse rate information. We recognize that the Schwarzsee ob Sölden chironomid record is a substantial distance inland from our study site the Maritime Alps; however, there are no closer chironomid records that extend to the present day. Therefore we splice this record with the Lago de Piccolo di Avigliana record with caution, and note that a simple lapse rate scaling of the Schwarzsee ob Sölden reconstruction to our sample elevations is likely problematic. Fig. 4.8 shows the scaled, spliced chironomid temperature reconstruction and the corresponding model for cosmogenic ^3He retention. Like the maximum seasonal temperatures from the TraCE-21ka simulation, we calculate cosmogenic ^3He retention from the mean July temperature reconstruction in agreement with our observations from PDP10.

To a first order, the fact that modern EDTs calculated from meteorological data are within a few degrees of the EDTs integrated over the exposure duration of each Gesso Valley quartz sample, and the fact that cosmogenic ^3He retention calculated with temperatures from a GCM simulation and an independent proxy reconstruction are in broad agreement with our cosmogenic ^3He observations, is promising. This first order agreement suggests that our cosmogenic ^3He measurements are, in fact, providing some information on ambient temperature conditions during exposure. For example, we do not calculate integrated EDTs below 0°C , as we do for cosmogenic ^3He measurements made on Holocene-age glacial erratics in Antarctica [68], nor do we calculate integrated EDTs unfeasibly high for Earth surface conditions (e.g, EDTs of $70\text{--}80^\circ\text{C}$ that we obtain for the Moon [125, 126]). However, for the purposes of reconstructing past climate variations, the substantial intra-moraine differences in EDTs are problematic and require explanation. For both the PM and TDB moraines, the difference in integrated EDTs between samples from the same moraine is $\sim 10^\circ\text{C}$.

One possibility is that these intra-moraine temperature differences are real and reflect differential shading of the samples by vegetation, snow cover or topography. Unshaded rock samples can experience significantly higher daytime temperatures due to insolation than shaded samples. As discussed in Chapter 1, heating of rocks due to incident solar radiation can substantially raise rock temperatures above daily maximum air temperatures. Amplification of temperatures $5\text{--}10^\circ\text{C}$ above the daily maximum is common in non-desert environments [48, 49, 202, 203]. Considering our modern EDT calculations from meteorological station data, if we increase the maximum daily temperature by 5 or 10°C , we find

significant increases in the EDT. For example, using the diffusion kinetics for TDB1, by increasing the maximum daily temperature in the meteorological data by 5 °C, we find that EDT increases from 15.9 to 19.2 °C. Increasing the maximum daily temperature by 10 °C increases the EDT to 23.0 °C, which is within the uncertainty of the EDT integrated over TDB1's exposure duration. Therefore it is possible that, in the case of the TDB moraine, TDB3 may have been shaded or snow covered during all or some of its exposure history, while TDB1 was fully exposed to incoming solar radiation throughout its exposure. Similarly, PM1 may have been shaded or snow covered while PM4 was not since the PM moraine was deposited.

This interpretation is consistent with the comparison of observed cosmogenic ^3He retention to calculated retention from TraCE-21ka and chironomid temperatures. TraCE-21ka simulation maximum seasonal temperature calculations agree well with PDP10, PM4, and TDB1 observations, while observations from PM1 and TDB3 are closer to the calculations with the mean seasonal temperature from TraCE-21ka. We would expect mean temperatures to agree with our cosmogenic ^3He observations, as is the case for PM1, if no heating due to insolation occurred. Following the same reasoning, we anticipate that samples experiencing nonzero insolation will have cosmogenic ^3He abundances that are lower than what is expected from mean temperatures, as is the case for PDP10, PM4, TDB1, and TDB3. Likewise, the good agreement between the observed cosmogenic ^3He retention in PDP10 and the chironomid-based reconstruction of mean July temperatures, which will be significantly greater than mean temperatures throughout most of the year, supports the interpretation that the temperatures experienced by sample PDP10 exceeded air temperatures during its exposure to cosmic ray particles. Relating maximum seasonal air temperatures or mean July air temperatures to insolation-induced daily rock temperature amplifications is not straightforward, although an empirical relationship could be obtained by monitoring *in situ* rock temperatures adjacent to meteorological stations. We attempted to obtain such a record by installing temperature sensor network inside a boulder at the PDP moraine in 2015; however, a pesky rodent chewed through the sensor cables and only one month of data was collected.

We note that shading from solar radiation and shielding of cosmic rays are not equivalent. Vegetative cover can have a substantial effect on heating by insolation, but in most cases a negligible effect on cosmogenic nuclide production rates due to its relatively low density. Similarly, thin snow cover will not substantially affect cosmogenic nuclide production rates but will cause rock temperatures to differ substantially from air temperatures. Thick snow cover (≥ 1 m) will affect both production rates and temperatures. Today, there is significant vegetation cover on the TDB and PM moraines, but no cover at PDP. Unfortunately, we have no way of assessing the degree of vegetation cover on the TDB and PM moraines before the modern, and no way to assess the past degree of snow cover for all moraines. Topography can shield rocks from cosmic ray particles, but these effects are accounted for in our calculations of cosmogenic nuclide production rates (Table 4.1); in contrast, we have not accounted for the effects of topographic shading on rock surface temperatures. We do not have detailed enough locations for the TDB and PM samples to identify the original boulders that were sampled and assess differences in topographic shading, although we suspect this would be

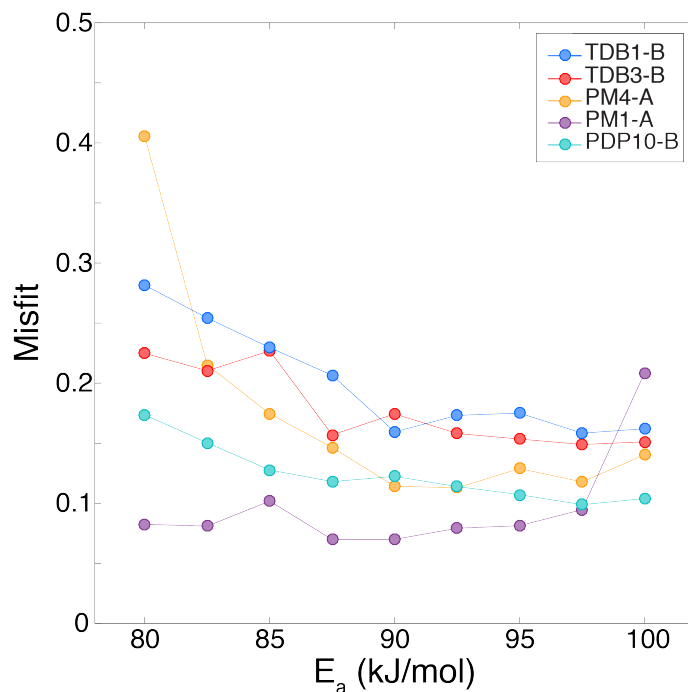


Figure 4.11: Minimized misfit between observed and MDD-modeled ^3He diffusivities as a function of activation energy E_a for Gesso Valley quartz samples, assuming a three domain diffusion model. Pre-exponential factors and gas fractions for each domain covary with E_a ; we show misfit as a function of E_a because it is assumed to be common to all diffusion domains in our modeling approach.

secondary to vegetation effects.

Another possible explanation for the intra-moraine differences is that our MDD model representations of helium diffusion kinetics in Gesso Valley quartz samples are inaccurate and/or inadequate. The MDD models we construct are inherently non-unique, and while the models we use do minimize the misfit between the observed and calculated diffusivities in our step degassing experiments for a given number of domains, comparable fits can be achieved over a range of diffusion parameters. To illustrate this, in Fig. 4.11 we show minimized values of MDD model misfit, calculated using Eq. 3.2 in Chapter 3, as a function of activation energy E_a for three domain models fit to each of the step degassing experiments shown in Fig. 4.4. For most of the step degassing experiments, there is a broad range of activation energies (and associated pre-exponential factors and gas release fractions) over which the misfit with the MDD model changes only slightly; these changes in misfit are much smaller than the change in misfit associated with increasing the number of diffusion domains and the model complexity (Fig. 4.5).

For example, the MDD misfit for the PM1-A step degassing experiment ranges between 7.0 and 10.2% between activation energies of 80 and 97.5 kJ/mol (Fig. 4.11). The MDD

diffusion kinetics we use in the forward models for PM1 quartz presented above assume an activation energy of 89.6 kJ/mol . If instead we use a different set of diffusion kinetics for a three domain model that yields a comparable misfit with the step degassing experiment ($E_a = 97.5 \text{ kJ/mol}$; $\ln(D_0/a^2) = 12.2, 10.1, 16.8$; $f_{gas} = 0.45, 0.44, 0.11$; $Misfit = 0.095$), we calculate an integrated EDT from the cosmogenic ^3He retention in PM1 quartz of $17.8 (\pm 2.3) +3.8/-3.9 \text{ }^\circ\text{C}$, which is in agreement with the integrated EDT we calculated for PM4 (Fig. 4.6). This highlights how sensitive the temperatures we calculate from an observed amount of cosmogenic ^3He retention are to the diffusion kinetics we use. While different MDD models might reproduce diffusivities observed in laboratory step degassing experiments comparably well, the downward extrapolation of these models results in significantly different diffusivities at the temperatures characterizing Earth's surface. This suggests that some or all of the intra-moraine differences in integrated EDTs could be attributed to uncertainties in how we extrapolate laboratory-determined diffusion kinetics. Given that we do not yet have a mechanistic understanding of what controls the complex noble gas diffusion behavior we observe in our experiments, discriminating between different MDD models of comparably good fit (and even assessing whether MDD models adequately represent the processes responsible for complex behavior) is difficult at this stage.

A third possible explanation for the intra-moraine variation could arise from our grain size analysis and scaling of MDD models. Uncertainty in the physical significance of our MDD models translates into an uncertainty in our assumptions about how to scale our MDD model fits from step degassing experiments to the cosmogenic ^3He measurements. However, because we have scaled the results of each experiment using the same assumptions in Eq. 4.1, the effects will be systematic. Similarly, the factor of 1.5 we applied to estimated spherical equivalent radii of quartz from the sieve fractions, based on different approaches to estimate surface area to volume ratios and ground truthing with x-ray computed tomography data, will have systematic effects on all integrated EDTs. Assuming that the MDD model scaling and correction applied to sieve fraction measurements are appropriate, we must also consider the possibility that our grain size analysis for the PM and TDB samples does not represent the actual grain size and diffusion lengthscale of quartz in these samples. Since we did not have whole rock material from the original PM and TDB samples, we made thin sections from other boulders collected from the PM and TDB moraines to compare with the size distributions of quartz in the sieved fraction. While there is good agreement between the mean spherical equivalent radii of quartz measured in these thin sections and in the sieve fractions, it is possible that in the original sample the mean quartz size before crushing was much larger. As a sensitivity test, we again use PM1 as an example. In order to obtain an integrated EDT for PM1 equivalent to that calculated for PM4 of $19.7 \text{ }^\circ\text{C}$, we must increase the spherical equivalent radius assumed for the cosmogenic ^3He measurement by 110% (without changing the spherical equivalent radius for PM4). While such a dramatic underestimation of the PM1 grain size, and more generally $>100\%$ uncertainty in all our PM and TDB grain size analyses, seems unlikely, we cannot rule out such a possibility given that whole rock material from these samples was unavailable.

In summary, integrated EDTs since the LGM, calculated from our observations of cosmo-

genic ^3He concentrations in quartz, are broadly consistent with what we expect from modern meteorological station data, a GCM simulation of Earth’s climate since the LGM, and data from independent proxies in the region. Nonetheless, there are nontrivial differences between the integrated EDTs we calculate, particularly for samples with equivalent exposure ages from the same moraine, that require explanation. We identify three major potential sources of uncertainty that could account for these discrepancies: (1) the fact that we have not accounted for variations in radiative heating of the boulder surfaces across samples, (2) limitations in our understanding of and ability to model and extrapolate helium diffusion kinetics when complex behavior is observed, or (3) uncertainties associated with our quartz grain size analyses. At this stage, all three of these possibilities could be contributing to intra-moraine and inter-moraine variability in reconstructed temperatures. Because of these nontrivial uncertainties, and the fact that we have no cosmogenic ^3He observations from younger moraines that record only more recent, Holocene temperatures in the Gesso Valley, it is difficult to fully compare our results to the TraCE-21ka and chironomid temperature records and not yet possible to comment on the hypothesis that the post-LGM climate evolution and glacier dynamics of the Maritime Alps differed from other Alpine sectors. Nonetheless these results are promising, and suggest that with additional work and better understanding of diffusion kinetics and rock-air temperature relationships we can address questions in paleoclimate like this one in future applications.

4.4.2 Cosmogenic neon retention in 76535 anorthite and recorded lunar surface paleotemperatures

Four of the five unirradiated anorthite grains we analyzed have neon isotopic compositions that plot on a mixing line between solar wind neon [204] and cosmogenic neon as determined by Lugmair et al. [185] (solid line, Fig. 4.12). Our data are offset to the right from an alternative mixing line between solar wind neon and the nominal cosmogenic neon production rate ratios calculated by Leya et al. [192] (dashed line, Fig. 4.12). However, the uncertainties on these latter cosmogenic production rate calculations are large enough [12%; 192] that they overlap with the Lugmair et al. [185] determination within uncertainty. The fifth analysis (aliquot v) plots below this mixing line, suggesting neon isotope fractionation during solar wind implantation [204], and is not used in thermal history calculations.

We deconvolved the cosmogenic component from the solar wind component in the remaining four analyses (Table 4.5). Using the elemental production rates of cosmogenic neon in Leya et al. [192] and the composition of 76535 anorthite from Dymek et al. [182], we calculated the total cosmogenic abundance of each neon isotope produced in these anorthite grains during the 142 ± 3 Ma exposure of 76535 (Table 4.5). Because we do not know the shielding depth of the specific anorthite grains we analyzed, depth-averaged production rates for each neon isotope were calculated over the maximum dimension of the whole rock sample inferred from photographs (6.5 cm). Cosmogenic neon retention was then calculated by dividing the observed cosmogenic neon abundances by the total amount of cosmogenic

neon produced during cosmic ray exposure. Retention values indicate that between 8 and 67% of the cosmogenic neon produced was diffusively lost (Table 4.5), with the amount of diffusive loss inversely correlated to the grain size analyzed.

Table 4.5: Observations of naturally-occurring neon isotopes in 76535 anorthite. Measured abundances, cosmogenic abundances, total cosmogenic neon produced during 142 Ma of exposure, and cosmogenic neon retention are reported.

Aliquot	^{20}Ne	\pm	^{21}Ne	\pm	^{22}Ne	\pm
Measured abundances (10^6 atoms)						
v (0.74 mg)	306027	6155	2650	42	26500	385
w (1.89 mg)	127928	2586	6155	99	16836	250
x (0.46 mg)	661	187	625	15	831	20
y (2.71 mg)	17266	536	10239	316	14077	363
z (1.68 mg)	5119	158	4995	78	6469	100
Cosmogenic abundances (10^6 atoms)						
w	5801	442	5862	179	7973	297
x	618	262	625	22	828	25
y	10115	705	10222	409	13572	370
z	4943	312	4995	149	6454	113
Total cosmogenic neon produced during 142 ± 3 Ma of exposure (10^6 atoms)						
w	7726	970	8292	1041	9954	716
x	1880	236	2018	253	2423	174
y	11078	1390	11890	1492	14273	1026
z	6868	862	7371	925	8848	636
Cosmogenic neon retention						
w	0.75	0.11	0.71	0.09	0.80	0.06
x	0.33	0.15	0.31	0.04	0.34	0.03
y	0.91	0.13	0.86	0.11	0.95	0.07
z	0.72	0.10	0.68	0.09	0.73	0.05

The results of our step degassing experiment to examine neon diffusion in 76535 anorthite are discussed extensively in Tremblay et al. [144] and in Chapter 3. To summarize, 76535 anorthite shows linear Arrhenius behavior for 97% of the ^{21}Ne measured (Fig. 4.13). Steps at low temperature that deviate from the linear array are most likely measurements of background but are statistically above the instrument detection limit. Deviations from linear behavior above 800 °C occur after a known structural transformation in anorthite [160, 161]. Although anorthite also undergoes a structural transition from a P1 to T triclinic crystal symmetry during our step degassing experiment around 300 °C [156, 157], the diffusion parameters we calculate from only the temperature steps below 300 °C are indistinguishable from those calculated using all the data between 170 and 800 °C. Therefore we interpret the

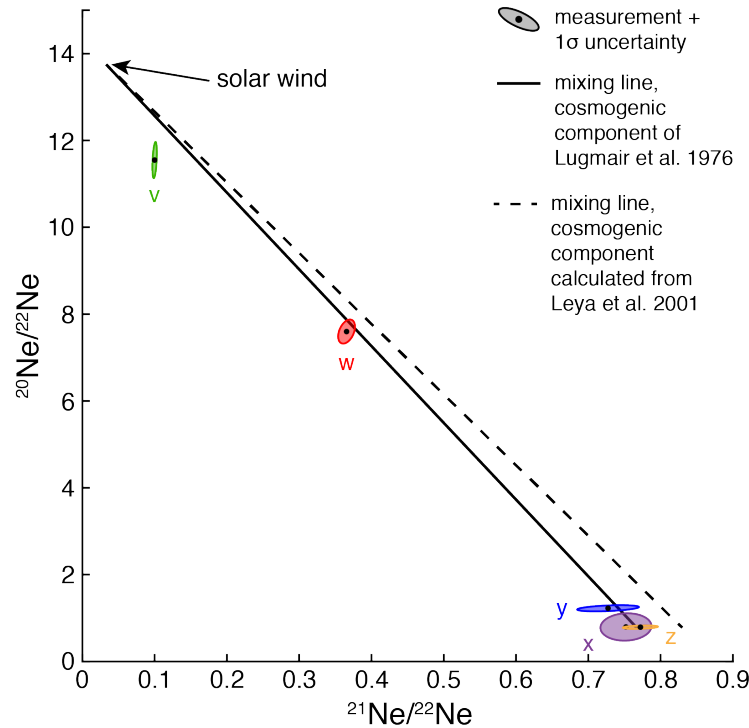


Figure 4.12: Three isotope plot showing the naturally-occurring neon isotopic composition of the five anorthite grains from 76535 we analyzed. Four of the five analyses plot on a mixing line between solar wind neon [204] and cosmogenic neon as determined by Lugmair et al. [185]. Analysis v plots below both mixing lines, which indicates that neon isotope fractionation occurred during solar wind implantation [204].

step degassing experiment on 76535 anorthite to reflect neon diffusion from a single diffusion domain, and assume that the diffusion lengthscale is equivalent to the spherical equivalent radius of the anorthite grain analyzed (296 μm).

Using the diffusion parameters calculated from the step degassing experiment (Fig. 4.13) scaled to the spherical equivalent radius of each anorthite grain in which we measured natural neon abundances, we modeled the simultaneous production and diffusion of cosmogenic neon for different EDTs. We calculated a reduced χ^2 misfit statistic for each EDT as follows:

$$\chi^2 = \frac{1}{n-1} \sum_{i=1}^n \left(\frac{R_{o,i} - R_{c,i}}{\sigma_i} \right)^2 \quad (4.2)$$

Where n is the number of measurements, R_c and R_o are the calculated and observed retention values for each measurement, respectively, and σ is the observed retention uncertainty. We calculated this misfit statistic using both the ^{21}Ne and ^{22}Ne diffusion parameters derived from the Arrhenius relationships shown in Fig. 4.13. We estimated the standard

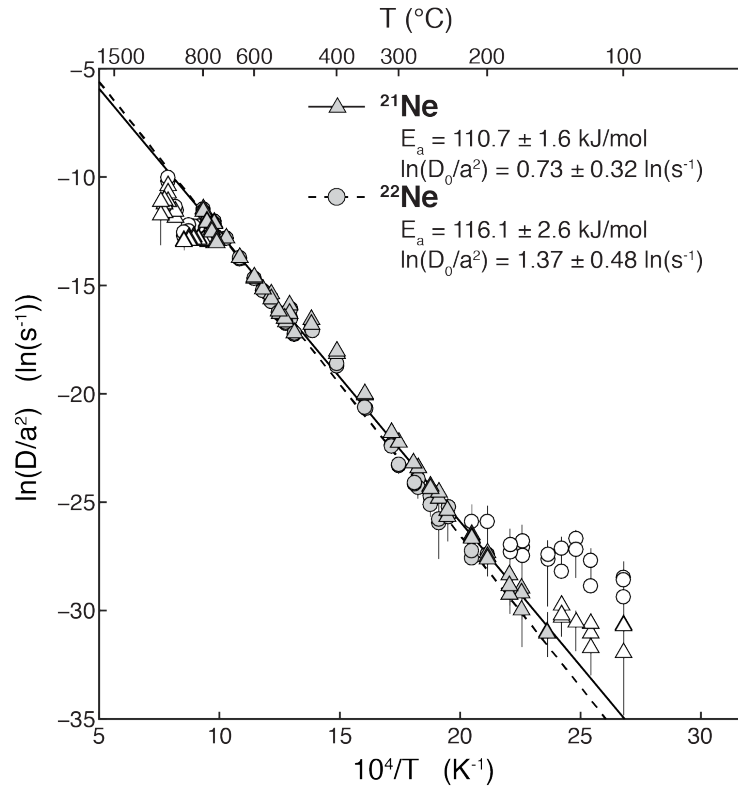


Figure 4.13: Arrhenius plot for diffusion of neutron-induced ^{21}Ne (triangles) and ^{22}Ne (circles) in a single crystal fragment of 76535 anorthite. Diffusivities were calculated using the equations of Fechtig and Kalbitzer [82] and the uncertainty propagation outlined in Tremblay et al. [87]. Filled symbols were used to fit linear regressions and calculate diffusion parameters. Initial low temperature steps that plot above the linear regression are close to the detection limit.

deviations from the EDTs 1.2 units greater than the minima in χ^2 , after Shuster and Cassata [125].

We find that a weighted mean EDT of 75.5 ± 4.2 °C best agrees with the observed cosmogenic neon abundances (Fig. 4.14). This is in excellent agreement with the weighted mean EDT of 77.0 ± 1.3 °C calculated from $^{40}\text{Ar}/^{39}\text{Ar}$ and $^{38}\text{Ar}/^{37}\text{Ar}$ whole rock measurements of Apollo 15 samples [125]. Given our calculated neon diffusion parameters and direct lunar surface temperature measurements [162], we estimate a modern EDT at the Apollo 17 landing site of ~ 83 °C (Fig. 4.15). Collectively, these results demonstrate that 76535 has only experienced heating due to insolation during its 142 Ma exposure at the lunar surface. There is no evidence to suggest that 76535 experienced heating associated with impact events that exceeded lunar surface EDTs at any point since the sample's initial exposure to cosmic ray particles.

These results from cosmogenic neon observations in 76535 anorthite suggest cosmogenic

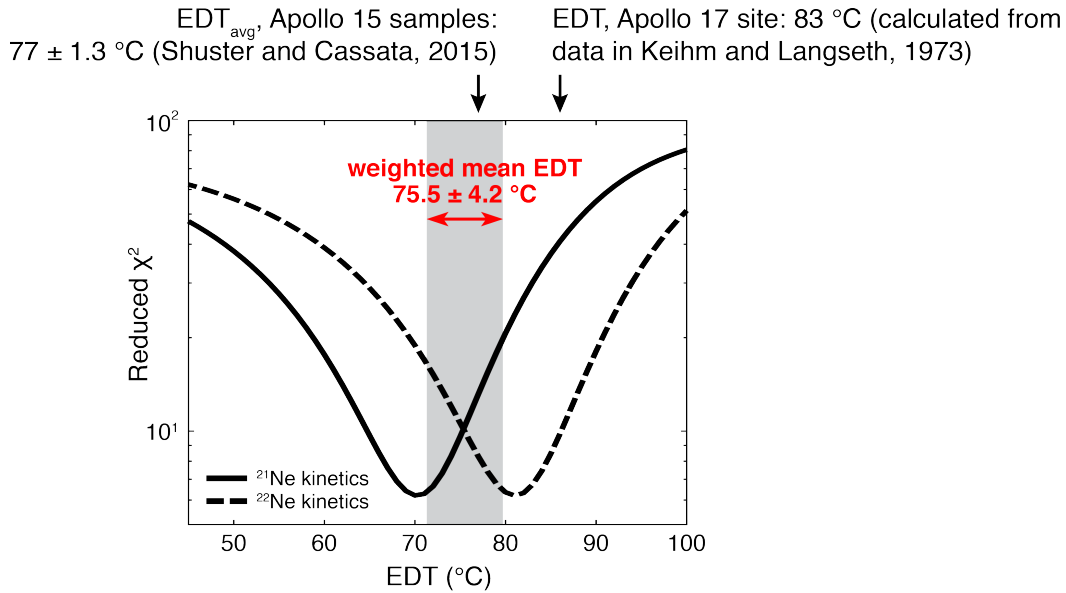


Figure 4.14: Reduced χ^2 misfit statistic calculated for different EDTs following Eq. 4.2. We calculated this misfit statistic using the diffusion parameters for ^{21}Ne (solid curve) and ^{22}Ne (dashed curve) derived from the Arrhenius relationships shown in Fig. 4.13. The weighted mean EDT from these two χ^2 distributions is 75.5 ± 4.2 °C.

neon paleothermometry may be feasible for meteorite or mission return samples from other planetary bodies, both in feldspars and in other mineral phases like quartz whose neon diffusion kinetics are sensitive to planetary surface temperatures. For example, cosmogenic neon observations either made at the Martian surface by an instrumented rover [e.g. 205] or in samples stored for return during the Mars 2020 mission could be used to assess near-surface Martian thermal conditions over million or billion year timescales, which could place important constraints the past habitability of the Martian surface [125]. This could be especially useful in samples for which cosmogenic and radiogenic argon are quantitatively retained at planetary surface temperatures and only able to place upper bounds on surface temperatures. In cases where both argon and neon exhibit open-system behavior, observations of cosmogenic isotopes of both noble gases will provide robust constraints on time-integrated planetary surface temperatures.

4.5 Conclusions

Having established the theoretical basis for cosmogenic noble gas paleothermometry and presented experimental data that quantify noble gas diffusion kinetics in relevant mineral phases in the previous chapters, in this chapter we presented applications of cosmogenic noble gas paleothermometry to a study of Late Quaternary paleoclimate and to a study of

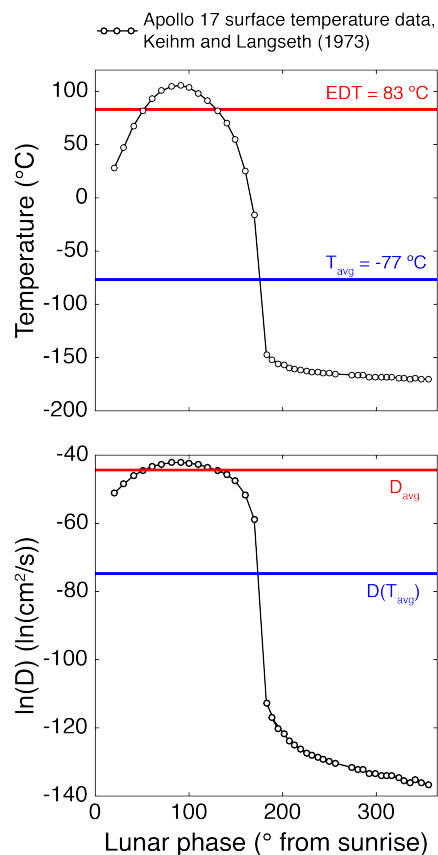


Figure 4.15: Relationship between EDT and mean temperature (T_{avg}) through the lunar daily insolation cycle at the Apollo 17 site, calculated using the ^{21}Ne diffusion kinetics for 76535 anorthite and surface temperature measurements in Keihm and Langseth [162].

lunar surface temperatures over tens of millions of years.

For the paleoclimate application, we used observations of cosmogenic ^3He in quartz from moraine boulders to reconstruct integrated effective diffusion temperatures since the LGM in the Gesso Valley, Maritime Alps, Italy. Although we cannot yet evaluate hypotheses about the climate evolution and glacier dynamics during deglaciation in the Maritime Alps from these data, our initial temperature reconstructions over the last 22 ka are reasonable in the context of temperatures predicted by other proxies in the southern Italian Alps and with temperature estimates from a GCM simulation. Future work to better understand rock-air temperature relationships and helium diffusion systematics in particular should improve uncertainties in our temperature reconstructions and allow for more direct comparisons with proxy and model-based reconstructions.

For the lunar application, we used cosmogenic neon observations in anorthite from Apollo 17 sample 76535 to reconstruct temperatures during this sample's 142 million year residence at the surface of the Moon. Our neon observations suggest that 76535 has only experienced

heating due to insolation while at the lunar surface; we find no evidence to support impact-related heating since initial exposure to cosmic ray particles. These results indicate promise for cosmogenic neon observations in other planetary materials and on other planetary bodies for reconstructing near surface temperatures on million or billion year timescales.

4.6 Acknowledgements

We thank M. Spagnolo and A. Ribolini for providing the Gesso Valley samples and for locating meteorological station and proxy data. H. Renssen kindly obtained TraCE-21ka data. We also thank M. Uebner, S. Woodmansee, N. Fylstra, T. Becker, and G. Balco for analytical assistance. We acknowledge support from the NSF Petrology and Geochemistry Program (EAR-1322086), the UC Berkeley Larsen Grant, and the Ann and Gordon Getty Foundation. MMT was supported by an NSF Graduate Research Fellowship.

Bibliography

1. Eiler, J. M. Paleoclimate reconstruction using carbonate clumped isotope thermometry. *Quaternary Science Reviews* **30**, 3575–3588 (2011).
2. Kim, S.-T. & O’Neil, J. R. Equilibrium and nonequilibrium oxygen isotope effects in synthetic carbonates. *Geochimica et Cosmochimica Acta* **61**, 3461–3475 (1997).
3. Rowley, D. B. & Garzzone, C. N. Stable isotope-based paleoaltimetry. *Annual Review of Earth and Planetary Sciences* **35**, 463–508 (2007).
4. Eiler, J. M. “Clumped isotope” geochemistry—The study of naturally, occurring, multiply-substituted isotopologues. *Earth and Planetary Science Letters* **262**, 309–327 (2007).
5. Ghosh, P. *et al.* ^{13}C – ^{18}O bonds in carbonate minerals: A new kind of paleothermometer. *Geochimica et Cosmochimica Acta* **70**, 1439–1456 (2006).
6. Quade, J., Breecker, D. O., Daëron, M. & Eiler, J. The paleoaltimetry of Tibet: An isotopic perspective. *American Journal of Science* **311**, 77–115 (2011).
7. Peters, N. A., Huntington, K. W. & Hoke, G. D. Hot or not? Impact of seasonally variable soil carbonate formation on paleotemperature and O-isotope records from clumped isotope thermometry. *Earth and Planetary Science Letters* **361**, 208–218 (2013).
8. Forest, C. E., Wolfe, J. A., Molnar, P. & Emanuel, K. A. Paleoaltimetry incorporating atmospheric physics and botanical estimates of paleoclimate. *Geological Society of America Bulletin* **111**, 497–511 (1999).
9. Gregory, K. M. & McIntosh, W. Paleoclimate and paleoelevation of the oligocene pitch-pinnacle flora, Sawatch Range, Colorado. *Geological Society of America Bulletin* **108**, 545–561 (1996).
10. Bartlein, P. *et al.* Pollen-based continental climate reconstructions at 6 and 21 ka: a global synthesis. *Climate Dynamics* **37**, 775–802 (2011).
11. Craig, H. & Poreda, R. Cosmogenic ^3He in terrestrial rocks: The summit lavas of Maui. *Proceedings of the National Academy of Sciences* **83**, 1970–1974 (1986).
12. Kurz, M. D. Cosmogenic helium in a terrestrial igneous rock. *Nature* **320**, 435–439 (1986).

13. Marti, K. & Craig, H. Cosmic-ray-produced neon and helium in the summit lavas of Maui. *Nature* **325**, 335–337 (1987).
14. Granger, D. E., Lifton, N. A. & Willenbring, J. K. A cosmic trip: 25 years of cosmogenic nuclides in geology. *Geological Society of America Bulletin* **125**, 1379–1402 (2013).
15. Dunai, T. J. *Cosmogenic nuclides: principles, concepts and applications in the earth surface sciences* (Cambridge University Press, 2010).
16. Bruno, L. A. *et al.* Dating of Sirius Group tillites in the Antarctic Dry Valleys with cosmogenic ^3He and ^{21}Ne . *Earth and Planetary Science Letters* **147**, 37–54 (1997).
17. Cerling, T. E. Dating geomorphologic surfaces using cosmogenic ^3He . *Quaternary Research* **33**, 148–156 (1990).
18. Ivy-Ochs, S., Kober, F., Alfimov, V., Kubik, P. & Synal, H.-A. Cosmogenic ^{10}Be , ^{21}Ne and ^{36}Cl in sanidine and quartz from Chilean ignimbrites. *Nuclear Instruments and Methods in Physics Research Section B: Beam Interactions with Materials and Atoms* **259**, 588–594 (2007).
19. Schäfer, J. M. *et al.* Cosmogenic noble gas studies in the oldest landscape on earth: surface exposure ages of the Dry Valleys, Antarctica. *Earth and Planetary Science Letters* **167**, 215–226 (1999).
20. Cherniak, D., Thomas, J. & Watson, E. Neon diffusion in olivine and quartz. *Chemical Geology* **371**, 68–82 (2014).
21. Gourbet, L. *et al.* Neon diffusion kinetics in olivine, pyroxene and feldspar: retentivity of cosmogenic and nucleogenic neon. *Geochimica et Cosmochimica Acta* **86**, 21–36 (2012).
22. Shuster, D. L. & Farley, K. A. Diffusion kinetics of proton-induced ^{21}Ne , ^3He , and ^4He in quartz. *Geochimica et Cosmochimica Acta* **69**, 2349–2359 (2005).
23. Trull, T. W., Kurz, M. & Jenkins, W. Diffusion of cosmogenic ^3He in olivine and quartz: implications for surface exposure dating. *Earth and Planetary Science Letters* **103**, 241–256 (1991).
24. Brook, E. J. & Kurz, M. D. Surface-exposure chronology using in situ cosmogenic ^3He in Antarctic quartz sandstone boulders. *Quaternary Research* **39**, 1–10 (1993).
25. Brook, E. J. *et al.* Chronology of Taylor Glacier advances in Arena Valley, Antarctica, using in situ cosmogenic ^3He and ^{10}Be . *Quaternary Research* **39**, 11–23 (1993).
26. Trull, T., Brown, E., Marty, B., Raisbeck, G. & Yiou, F. Cosmogenic ^{10}Be and ^3He accumulation in Pleistocene beach terraces in Death Valley, California, USA: Implications for cosmic-ray exposure dating of young surfaces in hot climates. *Chemical Geology* **119**, 191–207 (1995).
27. Brook, E. J., Kurz, M. D., Ackert, R. P., Raisbeck, G. & Yiou, F. Cosmogenic nuclide exposure ages and glacial history of late Quaternary Ross Sea drift in McMurdo Sound, Antarctica. *Earth and Planetary Science Letters* **131**, 41–56 (1995).

28. Ackert, R. P. *et al.* West Antarctic Ice Sheet elevations in the Ohio Range: Geologic constraints and ice sheet modeling prior to the last highstand. *Earth and Planetary Science Letters* **307**, 83–93 (2011).
29. Kober, F. *et al.* In situ cosmogenic ^{10}Be and ^{21}Ne in sanidine and in situ cosmogenic ^3He in Fe–Ti–oxide minerals. *Earth and Planetary Science Letters* **236**, 404–418 (2005).
30. Kober, F. *et al.* Denudation rates and a topography-driven rainfall threshold in northern Chile: Multiple cosmogenic nuclide data and sediment yield budgets. *Geomorphology* **83**, 97–120 (2007).
31. Harrison, T. M. & Zeitler, P. K. Fundamentals of noble gas thermochronometry. *Reviews in Mineralogy and Geochemistry* **58**, 123–149 (2005).
32. Shea, E. K. *et al.* A long-lived lunar core dynamo. *Science* **335**, 453–456 (2012).
33. Shuster, D. L. *et al.* A record of impacts preserved in the lunar regolith. *Earth and Planetary Science Letters* **290**, 155–165 (2010).
34. Suavet, C. *et al.* Persistence and origin of the lunar core dynamo. *Proceedings of the National Academy of Sciences* **110**, 8453–8458 (2013).
35. Dohmen, R. & Milke, R. Diffusion in polycrystalline materials: grain boundaries, mathematical models, and experimental data. *Reviews in Mineralogy and Geochemistry* **72**, 921–970 (2010).
36. Baxter, E. F. Diffusion of noble gases in minerals. *Reviews in Mineralogy and Geochemistry* **72**, 509–557 (2010).
37. Wolf, R., Farley, K. & Kass, D. Modeling of the temperature sensitivity of the apatite (U–Th)/He thermochronometer. *Chemical Geology* **148**, 105–114 (1998).
38. Farley, K., Shuster, D., Watson, E., Wanser, K. & Balco, G. Numerical investigations of apatite $^4\text{He}/^3\text{He}$ thermochronometry. *Geochemistry, Geophysics, Geosystems* **11** (2010).
39. Meesters, A. & Dunai, T. Solving the production–diffusion equation for finite diffusion domains of various shapes: Part I. Implications for low-temperature (U–Th)/He thermochronology. *Chemical Geology* **186**, 333–344 (2002).
40. Ketcham, R. A. Forward and inverse modeling of low-temperature thermochronometry data. *Reviews in Mineralogy and Geochemistry* **58**, 275–314 (2005).
41. Gosse, J. C. & Phillips, F. M. Terrestrial in situ cosmogenic nuclides: theory and application. *Quaternary Science Reviews* **20**, 1475–1560 (2001).
42. Lal, D. Cosmic ray labeling of erosion surfaces: in situ nuclide production rates and erosion models. *Earth and Planetary Science Letters* **104**, 424–439 (1991).
43. Jungers, M. C. *et al.* Active erosion–deposition cycles in the hyperarid Atacama Desert of Northern Chile. *Earth and Planetary Science Letters* **371**, 125–133 (2013).

44. Schaller, M., Ehlers, T., Blum, J. & Kallenberg, M. Quantifying glacial moraine age, denudation, and soil mixing with cosmogenic nuclide depth profiles. *Journal of Geophysical Research: Earth Surface* **114** (2009).
45. Christodoulides, C., Ettinger, K. V. & Fremlin, J. H. The use of TL glow peaks at equilibrium in the examination of the thermal and radiation history of materials. *Modern Geology* **2**, 275–280 (1971).
46. Durrani, S. *et al.* Thermoluminescence of Apollo 12 samples: implications for lunar temperature and radiation histories in *Lunar and Planetary Science Conference Proceedings* **3** (1972), 2955.
47. Deardorff, J. Efficient prediction of ground surface temperature and moisture, with inclusion of a layer of vegetation. *Journal of Geophysical Research: Oceans* **83**, 1889–1903 (1978).
48. Hall, K., Lindgren, B. S. & Jackson, P. Rock albedo and monitoring of thermal conditions in respect of weathering: some expected and some unexpected results. *Earth Surface Processes and Landforms* **30**, 801–812 (2005).
49. McGreevy, J. Thermal properties as controls on rock surface temperature maxima, and possible implications for rock weathering. *Earth Surface Processes and Landforms* **10**, 125–136 (1985).
50. McFadden, L., Eppes, M., Gillespie, A. & Hallet, B. Physical weathering in arid landscapes due to diurnal variation in the direction of solar heating. *Geological Society of America Bulletin* **117**, 161–173 (2005).
51. McKay, C. P. *et al.* Temperature and moisture conditions for life in the extreme arid region of the Atacama Desert: four years of observations including the El Nino of 1997–1998. *Astrobiology* **3**, 393–406 (2003).
52. Fowler, C. M. R. *The solid earth: an introduction to global geophysics* (Cambridge University Press, 1990).
53. Vermeesch, P. *et al.* Cosmogenic ^3He and ^{21}Ne measured in quartz targets after one year of exposure in the Swiss Alps. *Earth and Planetary Science Letters* **284**, 417–425 (2009).
54. Balco, G., Stone, J. O., Lifton, N. A. & Dunai, T. J. A complete and easily accessible means of calculating surface exposure ages or erosion rates from ^{10}Be and ^{26}Al measurements. *Quaternary geochronology* **3**, 174–195 (2008).
55. Balco, G. Contributions and unrealized potential contributions of cosmogenic-nuclide exposure dating to glacier chronology, 1990–2010. *Quaternary Science Reviews* **30**, 3–27 (2011).
56. Stone, J. O. *et al.* Holocene deglaciation of Marie Byrd land, west Antarctica. *Science* **299**, 99–102 (2003).

57. Clark, P. U. *et al.* Global climate evolution during the last deglaciation. *Proceedings of the National Academy of Sciences* **109**, E1134–E1142 (2012).
58. Shakun, J. D. *et al.* Global warming preceded by increasing carbon dioxide concentrations during the last deglaciation. *Nature* **484**, 49–54 (2012).
59. Farrera, I. *et al.* Tropical climates at the Last Glacial Maximum: a new synthesis of terrestrial palaeoclimate data. I. Vegetation, lake-levels and geochemistry. *Climate dynamics* **15**, 823–856 (1999).
60. Annan, J. & Hargreaves, J. A new global reconstruction of temperature changes at the Last Glacial Maximum. *Climate of the Past* **9**, 367–376 (2013).
61. Balco, G. & Rovey, C. W. Absolute chronology for major Pleistocene advances of the Laurentide Ice Sheet. *Geology* **38**, 795–798 (2010).
62. Haug, G. H. *et al.* North Pacific seasonality and the glaciation of North America 2.7 million years ago. *Nature* **433**, 821–825 (2005).
63. Raymo, M. The initiation of Northern Hemisphere glaciation. *Annual Review of Earth and Planetary Sciences* **22**, 353–383 (1994).
64. Fujioka, T. *et al.* Global cooling initiated stony deserts in central Australia 2–4 Ma, dated by cosmogenic ^{21}Ne – ^{10}Be . *Geology* **33**, 993–996 (2005).
65. Dunai, T. J., López, G. A. G. & Juez-Larré, J. Oligocene–Miocene age of aridity in the Atacama Desert revealed by exposure dating of erosion-sensitive landforms. *Geology* **33**, 321–324 (2005).
66. Evenstar, L. A. *et al.* Multiphase development of the Atacama Planation Surface recorded by cosmogenic ^3He exposure ages: Implications for uplift and Cenozoic climate change in western South America. *Geology* **37**, 27–30 (2009).
67. Bierman, P. R. & Caffee, M. Slow rates of rock surface erosion and sediment production across the Namib Desert and escarpment, southern Africa. *American Journal of Science* **301**, 326–358 (2001).
68. Tremblay, M. M., Shuster, D. L. & Balco, G. Cosmogenic noble gas paleothermometry. *Earth and Planetary Science Letters* **400**, 195–205 (2014).
69. Stone, J. O. Air pressure and cosmogenic isotope production. *Journal of Geophysical Research: Solid Earth* **105**, 23753–23759 (2000).
70. Balco, G. *et al.* Regional beryllium-10 production rate calibration for late-glacial north-eastern North America. *Quaternary Geochronology* **4**, 93–107 (2009).
71. Nishiizumi, K. *et al.* Absolute calibration of ^{10}Be AMS standards. *Nuclear Instruments and Methods in Physics Research Section B* **258**, 403–413 (2007).
72. Tremblay, M. M., Shuster, D. L. & Balco, G. Quantifying the open-system behavior of cosmogenic noble gases in quartz. *Mineralogical Magazine* **77**, 2297–237 (2013).

73. Nylén, T. H., Fountain, A. G. & Doran, P. T. Climatology of katabatic winds in the McMurdo dry valleys, southern Victoria Land, Antarctica. *Journal of Geophysical Research: Atmospheres* **109** (2004).
74. Jouzel, J. *et al.* A new 27 ky high resolution East Antarctic climate record. *Geophysical Research Letters* **28**, 3199–3202 (2001).
75. Masson, V. *et al.* Holocene climate variability in Antarctica based on 11 ice-core isotopic records. *Quaternary Research* **54**, 348–358 (2000).
76. Graf, W., Reinwarth, O., Oerter, H., Mayer, C. & Lambrecht, A. Surface accumulation on foundation ice stream, Antarctica. *Annals of Glaciology* **29**, 23–28 (1999).
77. Niedermann, S. The ^{21}Ne production rate in quartz revisited. *Earth and Planetary Science Letters* **183**, 361–364 (2000).
78. Balco, G. & Shuster, D. L. Production rate of cosmogenic ^{21}Ne in quartz estimated from ^{10}Be , ^{26}Al , and ^{21}Ne concentrations in slowly eroding Antarctic bedrock surfaces. *Earth and Planetary Science Letters* **281**, 48–58 (2009).
79. Kober, F., Alfimov, V., Ivy-Ochs, S., Kubik, P. & Wieler, R. The cosmogenic ^{21}Ne production rate in quartz evaluated on a large set of existing ^{21}Ne – ^{10}Be data. *Earth and Planetary Science Letters* **302**, 163–171 (2011).
80. Masarik, J. & Reedy, R. C. Terrestrial cosmogenic-nuclide production systematics calculated from numerical simulations. *Earth and Planetary Science Letters* **136**, 381–395 (1995).
81. Masarik, J. & Reedy, R. C. Monte Carlo simulation of in-situ-produced cosmogenic nuclides. *Radiocarbon* **38**, 163–164 (1996).
82. Fechtig, H. & Kalbitzer, S. in *Potassium argon dating* 68–107 (Springer, 1966).
83. Crank, J. *The Mathematics of Diffusion: 2d Ed* (Clarendon Press, 1975).
84. Watson, E. & Cherniak, D. Lattice diffusion of Ar in quartz, with constraints on Ar solubility and evidence of nanopores. *Geochimica et Cosmochimica Acta* **67**, 2043–2062 (2003).
85. Cherniak, D., Watson, E. & Thomas, J. Diffusion of helium in zircon and apatite. *Chemical Geology* **268**, 155–166 (2009).
86. Niedermann, S., Graf, T. & Marti, K. Mass spectrometric identification of cosmic-ray-produced neon in terrestrial rocks with multiple neon components. *Earth and Planetary Science Letters* **118**, 65–73 (1993).
87. Tremblay, M. M., Shuster, D. L. & Balco, G. Diffusion kinetics of ^3He and ^{21}Ne in quartz and implications for cosmogenic noble gas paleothermometry. *Geochimica et Cosmochimica Acta* **142**, 186–204 (2014).
88. Shuster, D. L., Farley, K. A., Sisterson, J. M. & Burnett, D. S. Quantifying the diffusion kinetics and spatial distributions of radiogenic ^4He in minerals containing proton-induced ^3He . *Earth and Planetary Science Letters* **217**, 19–32 (2004).

89. Bromley, G. R., Hall, B. L., Stone, J. O., Conway, H. & Todd, C. E. Late Cenozoic deposits at Reedy Glacier, Transantarctic mountains: implications for former thickness of the West Antarctic Ice Sheet. *Quaternary Science Reviews* **29**, 384–398 (2010).
90. Kelly, M. A. *et al.* Late glacial fluctuations of Quelccaya Ice Cap, southeastern Peru. *Geology* **40**, 991–994 (2012).
91. Kelly, M. A. *et al.* A locally calibrated, late glacial ^{10}Be production rate from a low-latitude, high-altitude site in the Peruvian Andes. *Quaternary Geochronology* **26**, 70–85 (2015).
92. Sasnett, P., Goehring, B. M., Christie-Blick, N. & Schaefer, J. M. Do phreatomagmatic eruptions at Ubehebe Crater (Death Valley, California) relate to a wetter than present hydro-climate? *Geophysical Research Letters* **39** (2012).
93. Niedermann, S. *et al.* Cosmic-ray-produced ^{21}Ne in terrestrial quartz: the neon inventory of Sierra Nevada quartz separates. *Earth and Planetary Science Letters* **125**, 341–355 (1994).
94. Reich, M., Ewing, R. C., Ehlers, T. A. & Becker, U. Low-temperature anisotropic diffusion of helium in zircon: implications for zircon (U–Th)/He thermochronometry. *Geochimica et Cosmochimica Acta* **71**, 3119–3130 (2007).
95. Cassata, W. S. & Renne, P. R. Systematic variations of argon diffusion in feldspars and implications for thermochronometry. *Geochimica et Cosmochimica Acta* **112**, 251–287 (2013).
96. Shuster, D. L., Flowers, R. M. & Farley, K. A. The influence of natural radiation damage on helium diffusion kinetics in apatite. *Earth and Planetary Science Letters* **249**, 148–161 (2006).
97. Flowers, R. M., Ketcham, R. A., Shuster, D. L. & Farley, K. A. Apatite (U–Th)/He thermochronometry using a radiation damage accumulation and annealing model. *Geochimica et Cosmochimica Acta* **73**, 2347–2365 (2009).
98. Guenther, W. R., Reiners, P. W., Ketcham, R. A., Nasdala, L. & Giester, G. Helium diffusion in natural zircon: Radiation damage, anisotropy, and the interpretation of zircon (U–Th)/He thermochronology. *American Journal of Science* **313**, 145–198 (2013).
99. Saadoune, I., Purton, J. A. & de Leeuw, N. H. He incorporation and diffusion pathways in pure and defective zircon ZrSiO_4 : a density functional theory study. *Chemical Geology* **258**, 182–196 (2009).
100. Müller, A., Wiedenbeck, M., Van Den Kerkhof, A. M., Kronz, A. & Simon, K. Trace elements in quartz—a combined electron microprobe, secondary ion mass spectrometry, laser-ablation ICP-MS, and cathodoluminescence study. *European Journal of Mineralogy* **15**, 747–763 (2003).

101. Götze, J., Plötze, M., Graupner, T., Hallbauer, D. K. & Bray, C. J. Trace element incorporation into quartz: a combined study by ICP-MS, electron spin resonance, cathodoluminescence, capillary ion analysis, and gas chromatography. *Geochimica et Cosmochimica Acta* **68**, 3741–3759 (2004).
102. Dennen, W. Stoichiometric substitution in natural quartz. *Geochimica et Cosmochimica Acta* **30**, 1235–1241 (1966).
103. Lifton, N., Sato, T. & Dunai, T. J. Scaling in situ cosmogenic nuclide production rates using analytical approximations to atmospheric cosmic-ray fluxes. *Earth and Planetary Science Letters* **386**, 149–160 (2014).
104. Goehring, B. M. *et al.* A reevaluation of in situ cosmogenic ^3He production rates. *Quaternary Geochronology* **5**, 410–418 (2010).
105. Heaney, P. J. & Veblen, D. R. Observations of the α - β phase transition in quartz; a review of imaging and diffraction studies and some new results. *American Mineralogist* **76**, 1018–1032 (1991).
106. Ackermann, R. & Sorrell, C. A. Thermal expansion and the high–low transformation in quartz. I. High-temperature X-ray studies. *Journal of Applied Crystallography* **7**, 461–467 (1974).
107. Shuster, D. L. & Farley, K. A. The influence of artificial radiation damage and thermal annealing on helium diffusion kinetics in apatite. *Geochimica et Cosmochimica Acta* **73**, 183–196 (2009).
108. Botis, S. *et al.* Natural radiation-induced damage in quartz. I. Correlations between cathodoluminescence colors and paramagnetic defects. *The Canadian Mineralogist* **43**, 1565–1580 (2005).
109. Krickl, R., Nasdala, L., Götze, J., Grambole, D. & Wirth, R. Alpha-irradiation effects in SiO_2 . *European Journal of Mineralogy* **20**, 517–522 (2008).
110. Götze, J. Chemistry, textures and physical properties of quartz—geological interpretation and technical application. *Mineralogical Magazine* **73**, 645–671 (2009).
111. Argunova, T. *et al.* The influence of defects in the crystal structure on helium diffusion in quartz. *Physics of the Solid State* **45**, 1910–1917 (2003).
112. Clay, P. *et al.* Two diffusion pathways in quartz: a combined UV-laser and RBS study. *Geochimica et Cosmochimica Acta* **74**, 5906–5925 (2010).
113. Lovera, O. M. & Richter, F. M. The $^{40}\text{Ar}/^{39}\text{Ar}$ Thermochronometry for Slowly Cooled Samples. *Journal of Geophysical Research* **94**, 17917–17935 (1989).
114. Lovera, O. M., Grove, M., Harrison, T. M. & Mahon, K. Systematic analysis of K-feldspar $^{40}\text{Ar}/^{39}\text{Ar}$ step heating results: I. Significance of activation energy determinations. *Geochimica et Cosmochimica Acta* **61**, 3171–3192 (1997).
115. Hetzel, R. *et al.* Low slip rates and long-term preservation of geomorphic features in Central Asia. *Nature* **417**, 428–432 (2002).

116. Bradley, R. S., Keimig, F. T., Diaz, H. F. & Hardy, D. R. Recent changes in freezing level heights in the Tropics with implications for the deglaciation of high mountain regions. *Geophysical Research Letters* **36** (2009).
117. Thompson, L. G., Mosley-Thompson, E., Davis, M. E., *et al.* Late glacial stage and Holocene tropical ice core records from Huascarán, Peru. *Science* **269**, 46–50 (1995).
118. Herman, F. *et al.* Worldwide acceleration of mountain erosion under a cooling climate. *Nature* **504**, 423–426 (2013).
119. Min, K., Reiners, P. W., Nicolescu, S. & Greenwood, J. P. Age and temperature of shock metamorphism of Martian meteorite Los Angeles from (U-Th)/He thermochronometry. *Geology* **32**, 677 (2004).
120. Cassata, W. S., Shuster, D. L., Renne, P. R. & Weiss, B. P. Evidence for shock heating and constraints on Martian surface temperatures revealed by $^{40}\text{Ar}/^{39}\text{Ar}$ thermochronometry of Martian meteorites. *Geochimica et Cosmochimica Acta* **74**, 6900–6920 (2010).
121. Jourdan, F., Moynier, F., Koeberl, C. & Eroglu, S. $^{40}\text{Ar}/^{39}\text{Ar}$ age of the Lonar crater and consequence for the geochronology of planetary impacts. *Geology* **39**, 671–674 (2011).
122. Richter, F. M., Lovera, O. M., Mark Harrison, T. & Copeland, P. Tibetan tectonics from $^{40}\text{Ar}/^{39}\text{Ar}$ analysis of a single K-feldspar sample. *Earth and Planetary Science Letters* **105**, 266–278 (1991).
123. Hodges, K. V., Ruhl, K. W., Wobus, C. W. & Pringle, M. S. $^{40}\text{Ar}/^{39}\text{Ar}$ Thermochronology of Detrital Minerals. *Reviews in Mineralogy and Geochemistry* **58**, 239–257 (2005).
124. Turner, G. ^{40}Ar - ^{39}Ar ages from the lunar maria. *Earth and Planetary Science Letters* **11**, 169–191 (1971).
125. Shuster, D. L. & Cassata, W. S. Paleotemperatures at the lunar surfaces from open system behavior of cosmogenic ^{38}Ar and radiogenic ^{40}Ar . *Geochimica et Cosmochimica Acta* **155**, 154–171 (2015).
126. Garrick-Bethell, I., Weiss, B. P., Shuster, D. L., Tikoo, S. M. & Tremblay, M. M. Further evidence for early lunar magnetism from troctolite 76535. *Journal of Geophysical Research: Planets* (2017).
127. Lovera, O. M., Harrison, T. M. & Boehnke, P. Comment on "Systematic variations of argon diffusion in feldspars and implications for thermochronometry" by Cassata and Renne. *Geochimica et Cosmochimica Acta* **151**, 168–171 (2015).
128. Reynolds, J. H. Comparative study of argon content and argon diffusion in mica and feldspar. *Geochimica et Cosmochimica Acta* **12**, 177–184 (1957).
129. Fechtig, H., Gentner, W. & Zähringer, J. Argonbestimmungen an Kaliummineralien—VII Diffusionsverluste von Argon in Mineralien und ihre Auswirkung auf die Kalium-Argon-Altersbestimmung. *Geochimica et Cosmochimica Acta* **19**, 70–79 (1960).

130. Evernden, J. F., Curtis, G. H., Kistler, R. W. & Obradovich, J. D. Argon diffusion in glauconite, microcline, sanidine, leucite and phlogopite. *American Journal of Science* **258**, 583–604 (1960).
131. Gerling, E. K., Levski, L. K. & Morozova, I. M. On the diffusion of radiogenic argon from minerals. *Geokhimiya* **Vol: No. 6** (1963).
132. Berger, G. W. & York, D. Geothermometry from $^{40}\text{Ar}/^{39}\text{Ar}$ dating experiments. *Geochimica et Cosmochimica Acta* **45**, 795–811 (1981).
133. Harrison, T. M. & McDougall, I. The thermal significance of potassium feldspar K-Ar ages inferred from $^{40}\text{Ar}/^{39}\text{Ar}$ age spectrum results. *Geochimica et Cosmochimica Acta* **46**, 1811–1820 (1982).
134. Lovera, O. M., Richter, F. M. & Harrison, T. M. Diffusion domains determined by ^{39}Ar released during step heating. *Journal of Geophysical Research* **96**, 2057–2069 (1991).
135. Harrison, T. M., Lovera, O. M. & Matthew, T. H. $^{40}\text{Ar}/^{39}\text{Ar}$ results for alkali feldspars containing diffusion domains with differing activation energy. *Geochimica et Cosmochimica Acta* **55**, 1435–1448 (1991).
136. Villa, I. M. From nanometer to megameter: Isotopes, atomic-scale processes, and continent-scale tectonic models. *Lithos* **87**, 155–173 (2006).
137. Parsons, I., Brown, W. L. & Smith, J. V. $^{40}\text{Ar}/^{39}\text{Ar}$ thermochronology using alkali feldspars: real thermal history or mathematical mirage of microtexture? en. *Contributions to Mineralogy and Petrology* **136**, 92–110 (1999).
138. Lovera, O. M., Grove, M. & Harrison, T. M. Systematic analysis of K-feldspar $^{40}\text{Ar}/^{39}\text{Ar}$ step heating results II: Relevance of laboratory argon diffusion properties to nature. *Geochimica et Cosmochimica Acta* **66**, 1237–1255 (2002).
139. McLaren, S., Dunlap, W. J. & Powell, R. Understanding K-feldspar $^{40}\text{Ar}/^{39}\text{Ar}$ data: reconciling models, methods and microtextures. *Journal of the Geological Society of London* **164**, 941–944 (2007).
140. Villa, I. M. & Hanchar, J. M. K-feldspar hygrochronology. *Geochimica et Cosmochimica Acta* **101**, 24–33 (2013).
141. Shuster, D. L. & Farley, K. A. $^4\text{He}/^3\text{He}$ Thermochronometry: Theory, Practice, and Potential Complications. *Reviews in Mineralogy and Geochemistry* **58**, 181–203 (2005).
142. Foland, K. A. & Xu, Y. Diffusion of ^{40}Ar and ^{39}Ar in irradiated orthoclase. *Geochimica et Cosmochimica Acta* **54**, 3147–3158 (1990).
143. Lovera, O. M., Heizler, M. T. & Harrison, T. M. Argon diffusion domains in K-feldspar II: Kinetic properties of MH-10. *Contributions to Mineralogy and Petrology* **113**, 381–393 (1993).
144. Tremblay, M. M., Shuster, D. L., Balco, G. & Cassata, W. S. Neon diffusion kinetics and implications for cosmogenic neon paleothermometry in feldspars. *Geochimica et Cosmochimica Acta* **205**, 14–30 (2017).

145. Gautheron, C. & Tassan-Got, L. A Monte Carlo approach to diffusion applied to noble gas/helium thermochronology. *Chemical Geology* **273**, 212–224 (2010).
146. Huber, C., Cassata, W. S. & Renne, P. R. A lattice Boltzmann model for noble gas diffusion in solids: The importance of domain shape and diffusive anisotropy and implications for thermochronometry. *Geochimica et Cosmochimica Acta* **75**, 2170–2186 (2011).
147. Ketcham, R. A. & Carlson, W. D. Acquisition, optimization and interpretation of X-ray computed tomographic imagery: applications to the geosciences. *Computers & Geosciences* **27**, 381–400 (2001).
148. Ketcham, R. A. Computational methods for quantitative analysis of three-dimensional features in geological specimens. *Geosphere* **1**, 32–41 (2005).
149. Schairer, J. F. The Alkali-Feldspar Join in the System $\text{NaAlSi}_3\text{O}_8$ - KAlSi_3O_8 - SiO_2 . *Journal of Geology* **58**, 512–517 (1950).
150. Parsons, I. Feldspars defined and described: a pair of posters published by the Mineralogical Society. Sources and supporting information. en. *Mineralogical Magazine* **74**, 529–551 (2010).
151. Brown, W. L., Openshaw, R. E., McMillan, P. F. & Henderson, M. B. A review of the expansion behavior of alkali feldspars: coupled variations in cell parameters and possible phase transitions. *American Mineralogist* **69**, 1058–1071 (1984).
152. Hovis, G. L., Brennan, S., Keohane, M. & Crelling, J. High-temperature x-ray investigation of sanidine-analbite crystalline solutions: thermal expansion, phase transitions, and volumes of mixing. *The Canadian Mineralogist* **37**, 701–709 (1999).
153. Bachmann, O., Dungan, M. A. & Lipman, P. W. The Fish Canyon Magma Body, San Juan Volcanic Field, Colorado: Rejuvenation and Eruption of an Upper-Crustal Batholith. *Journal of Petrology* **43**, 1469–1503 (2002).
154. Koning, A. J. *et al.* *TENDL-2015* https://tendl.web.psi.ch/tendl_2015/tendl2015.html. 2015.
155. Tribaudino, M. *et al.* Thermal expansion of plagioclase feldspars. en. *Contributions to Mineralogy and Petrology* **160**, 899–908 (2010).
156. Smith, J. V. & Ribbe, P. H. Atomic movements in plagioclase feldspars: Kinetic interpretation. en. *Contributions to Mineralogy and Petrology* **21**, 157–202 (1969).
157. Van Tendeloo, G., Ghose, S. & Amelinckx, S. A dynamical model for the P1–I1 phase transition in anorthite, $\text{CaAl}_2\text{Si}_2\text{O}_8$. en. *Physics and Chemistry of Minerals* **16**, 311–319 (1989).
158. McLaren, A. C. & Marshall, D. B. Transmission electron microscope study of the domain structures associated with the b-, c-, d-, e- and f-reflections in plagioclase feldspars. en. *Contributions to Mineralogy and Petrology* **44**, 237–249 (1974).

159. Rainey, C. S. & Wenk, H.-R. Intensity differences of subsidiary reflections in calcic plagioclase. *American Mineralogist* **63**, 124–131 (1978).
160. Megaw, H. D., Kempster, C. & Radoslovich, E. The structure of anorthite, $\text{CaAl}_2\text{Si}_2\text{O}_8$. II. Description and discussion. *Acta Crystallographica* **15**, 1017–1035 (1962).
161. Foit Jr., F. F. & Peacor, D. R. The Anorthite Crystal Structure at 410 and 830 °C. *American Mineralogist* **58**, 665–675 (1973).
162. Keihm, S. & Langseth Jr, M. *Surface brightness temperatures at the Apollo 17 heat flow site: Thermal conductivity of the upper 15 cm of regolith in Lunar and Planetary Science Conference Proceedings* **4** (1973), 2503.
163. Federici, P., Pappalardo, M. & Ribolini, A. Geomorphological map of the Maritime Alps Natural Park and surroundings (Argentera Massif, Italy). 1: 25,000 scale. *Selca, Florence* (2003).
164. Federici, P. R. *et al.* Exposure age dating and Equilibrium Line Altitude reconstruction of an Egesen moraine in the Maritime Alps, Italy. *Boreas* **37**, 245–253 (2008).
165. Federici, P. R. *et al.* Last Glacial Maximum and the Gschnitz stadial in the Maritime Alps according to ^{10}Be cosmogenic dating. *Boreas* **41**, 277–291 (2012).
166. Federici, P. R., Ribolini, A. & Spagnolo, M. Glacial history of the Maritime Alps from the Last Glacial Maximum to the Little Ice Age. *Geological Society, London, Special Publications* **433**, 137–159 (2017).
167. Kuhlemann, J. *et al.* Regional synthesis of Mediterranean atmospheric circulation during the Last Glacial Maximum. *Science* **321**, 1338–1340 (2008).
168. Cheddadi, R., Yu, G., Guiot, J., Harrison, S. & Prentice, I. C. The climate of Europe 6000 years ago. *Climate dynamics* **13**, 1–9 (1996).
169. Davis, B. A., Brewer, S., Stevenson, A. C. & Guiot, J. The temperature of Europe during the Holocene reconstructed from pollen data. *Quaternary Science Reviews* **22**, 1701–1716 (2003).
170. Wu, H., Guiot, J., Brewer, S. & Guo, Z. Climatic changes in Eurasia and Africa at the last glacial maximum and mid-Holocene: reconstruction from pollen data using inverse vegetation modelling. *Climate Dynamics* **29**, 211–229 (2007).
171. Cheddadi, R. & Bar-Hen, A. Spatial gradient of temperature and potential vegetation feedback across Europe during the late Quaternary. *Climate Dynamics* **32**, 371–379 (2009).
172. Larocque, I. & Finsinger, W. Late-glacial chironomid-based temperature reconstructions for Lago Piccolo di Avigliana in the southwestern Alps (Italy). *Palaeogeography, Palaeoclimatology, Palaeoecology* **257**, 207–223 (2008).
173. Brisset, E. *et al.* Lateglacial/Holocene environmental changes in the Mediterranean Alps inferred from lacustrine sediments. *Quaternary Science Reviews* **110**, 49–71 (2015).

174. Gandouin, E. & Franquet, E. Late Glacial and Holocene chironomid assemblages in Lac Long Inférieur (southern France, 2090 m): palaeoenvironmental and palaeoclimatic implications. *Journal of Paleolimnology* **28**, 317–328 (2002).
175. Kessler, M. A., Anderson, R. S. & Stock, G. M. Modeling topographic and climatic control of east-west asymmetry in Sierra Nevada glacier length during the Last Glacial Maximum. *Journal of Geophysical Research: Earth Surface* **111** (2006).
176. Jost, A. *et al.* High-resolution simulations of the last glacial maximum climate over Europe: a solution to discrepancies with continental palaeoclimatic reconstructions? *Climate Dynamics* **24**, 577–590 (2005).
177. Heiri, O. *et al.* Validation of climate model-inferred regional temperature change for late-glacial Europe. *Nature communications* **5**, 4914 (2014).
178. Durand, Y. *et al.* Reanalysis of 47 years of climate in the French Alps (1958–2005): climatology and trends for snow cover. *Journal of applied meteorology and climatology* **48**, 2487–2512 (2009).
179. Durand, Y. *et al.* Reanalysis of 44 yr of climate in the French Alps (1958–2002): methodology, model validation, climatology, and trends for air temperature and precipitation. *Journal of Applied Meteorology and Climatology* **48**, 429–449 (2009).
180. Casazza, G., Grassi, F., Zecca, G. & Minuto, L. Phylogeographic Insights into a Peripheral Refugium: The Importance of Cumulative Effect of Glaciation on the Genetic Structure of Two Endemic Plants. *PloS one* **11**, e0166983 (2016).
181. Gooley, R., Brett, R., Warner, J. & Smyth, J. A lunar rock of deep crustal origin: Sample 76535. *Geochimica et Cosmochimica Acta* **38**, 1329–1339 (1974).
182. Dymek, R., Albee, A. & Chodos, A. *Comparative petrology of lunar cumulate rocks of possible primary origin-Dunite 72415, troctolite 76535, norite 78235, and anorthosite 62237 in Lunar and Planetary Science Conference Proceedings* **6** (1975), 301–341.
183. McCallum, I. & Schwartz, J. Lunar Mg suite: Thermobarometry and petrogenesis of parental magmas. *Journal of Geophysical Research: Planets* **106**, 27969–27983 (2001).
184. Huneke, J. & Wasserburg, G. *Trapped ^{40}Ar in troctolite 76535 and evidence for enhanced ^{40}Ar - ^{39}Ar age plateaus in Lunar and Planetary Science Conference* **6** (1975).
185. Lugmair, G., Marti, K., Kurtz, J. & Scheinin, N. *History and genesis of lunar troctolite 76535 or: How old is old in Lunar and Planetary Science Conference Proceedings* **7** (1976), 2009–2033.
186. Premo, W. R. & Tatsumoto, M. *U-Th-Pb, Rb-Sr, and Sm-Nd isotopic systematics of lunar troctolitic cumulate 76535-Implications on the age and origin of this early lunar, deep-seated cumulate in Lunar and Planetary Science Conference Proceedings* **22** (1992), 381–397.
187. Husain, L. & Schaeffer, O. Lunar evolution: The first 600 million years. *Geophysical Research Letters* **2**, 29–32 (1975).

188. Bogard, D., Nyquist, L., Bansal, B., Wiesmann, H. & Shih, C. 76535: An old lunar rock. *Earth and Planetary Science Letters* **26**, 69–80 (1975).
189. Garrick-Bethell, I., Weiss, B. P., Shuster, D. L. & Buz, J. Early lunar magnetism. *Science* **323**, 356–359 (2009).
190. Braddy, D., Hutcheon, I. & Price, P. *Crystal chemistry of Pu and U and concordant fission track ages of lunar zircons and whitlockites in Lunar and Planetary Science Conference Proceedings* **6** (1975), 3587–3600.
191. Garrick-Bethell, I. & Weiss, B. P. Kamacite blocking temperatures and applications to lunar magnetism. *Earth and planetary science Letters* **294**, 1–7 (2010).
192. Leya, I., Neumann, S., Wieler, R. & Michel, R. The production of cosmogenic nuclides by galactic cosmic-ray particles for 2π exposure geometries. *Meteoritics & Planetary Science* **36**, 1547–1561 (2001).
193. Buckenham, M. & Rogers, J. Flotation of quartz and feldspar by dodecylamine. *Transactions of Institute of Mining and Metallurgy* **64**, 1–30 (1954).
194. Abramoff, M. D., Magalhães, P. J. & Ram, S. J. Image processing with ImageJ. *Biophotonics international* **11**, 36–42 (2004).
195. Heilbronner, R. & Barrett, S. *Image analysis in Earth sciences: microstructures and textures of earth materials* (Springer Science & Business Media, 2013).
196. Collins, W. D. *et al.* The community climate system model version 3 (CCSM3). *Journal of Climate* **19**, 2122–2143 (2006).
197. Liu, Z. *et al.* Transient simulation of last deglaciation with a new mechanism for Bølling-Allerød warming. *Science* **325**, 310–314 (2009).
198. He, F. *Simulating transient climate evolution of the last deglaciation with CCSM 3* PhD thesis (2011).
199. Gardner, A. S. *et al.* Near-surface temperature lapse rates over Arctic glaciers and their implications for temperature downscaling. *Journal of Climate* **22**, 4281–4298 (2009).
200. Loomis, S. E. *et al.* The tropical lapse rate steepened during the Last Glacial Maximum. *Science advances* **3**, e1600815 (2017).
201. Ilyashuk, E. A., Koinig, K. A., Heiri, O., Ilyashuk, B. P. & Psenner, R. Holocene temperature variations at a high-altitude site in the Eastern Alps: a chironomid record from Schwarzsee ob Sölden, Austria. *Quaternary Science Reviews* **30**, 176–191 (2011).
202. Bartlett, M. G., Chapman, D. S. & Harris, R. N. A decade of ground–air temperature tracking at Emigrant Pass Observatory, Utah. *Journal of Climate* **19**, 3722–3731 (2006).

203. Schwarz, N., Schlink, U., Franck, U. & Großmann, K. Relationship of land surface and air temperatures and its implications for quantifying urban heat island indicators—An application for the city of Leipzig (Germany). *Ecological Indicators* **18**, 693–704 (2012).
204. Grimberg, A. *et al.* Solar wind neon from Genesis: implications for the lunar noble gas record. *Science* **314**, 1133–1135 (2006).
205. Farley, K. *et al.* In situ radiometric and exposure age dating of the Martian surface. *science* **343**, 1247166 (2014).